Interferometry on small quantum systems at short wavelength

Dissertation
zur Erlangung des Doktorgrades an der Fakultät für Mathematik, Informatik und Naturwissenschaften
Fachbereich Physik
der Universität Hamburg

vorgelegt von

Sergey Usenko

Hamburg
2016

Gutachter der Dissertation:	PD Dr. Tim Laarmann
	Prof. Dr. Markus Drescher
Gutachter der Disputation:	PD Dr. Tim Laarmann
	Prof. Dr. Markus Drescher
	Prof. Dr. Wilfried Wurth
	Prof. Dr. Nils Huse
	Prof. Dr. Ludwig Mathey
Datum der Disputation:	23 September 2016
Vorsitzender des Prüfungsausschusses:	Prof. Dr. Ludwig Mathey
Vorsitzender des Promotionsausschusses:	Prof. Dr. Wolfgang Hansen
Leiter des Fachbereichs Physik:	Prof. Dr. Michael Potthoff
Dekan der MIN-Fakultät:	Prof. Dr. Heinrich Graener

Eidesstattliche Versicherung
Declaration on oath

Hiermit erkläre ich an Eides statt, dass ich die vorliegende Dissertationsschrift selbst verfasst und keine anderen als die angegebenen Quellen und Hilfmittel benutzt habe.
I hereby declare, on oath, that I have written the present dissertation by my own and have not used other than the acknowledged resources and aids.

Hamburg, den *city and date* *Unterschrift* *signature*

Abstract

The present work concentrates on prototypical studies of light-induced correlated many-body dynamics in complex systems. In its course a reflective split-and-delay unit (SDU) for phase-resolved one-color pump-probe experiments with gas phase samples using VUV–XUV laser pulses was built. The collinear propagation of pump and probe pulses is ensured by the special geometry of the SDU and allows to perform phase-resolved (coherent) autocorrelation measurements. The control of the pump-probe delay with attosecond precision is established by a specially developed diagnostic tool based on an in-vacuum white light interferometer that allows to monitor the relative displacement of the SDU reflectors with nanometer resolution. Phase-resolved (interferometric) pump-probe experiments with developed SDU require spatially-resolved imaging of the ionization volume. For this an electron–ion coincidence spectrometer was built. The spectrometer enables coincident detection of photoionization products using velocity map imaging (VMI) technique for electrons and VMI or spatial imaging for ions. In first experiments using the developed SDU and the spectrometer in the ion spatial-imaging mode linear field autocorrelation of free-electron laser pulses at the central wavelength of 38 nm was recorded.

A further focus of the work were energy- and time-resolved resonant two-photon ionization experiments using short tunable UV laser pulses on C_{60} fullerene. The experiments demonstrated that dipole-selective excitation on a timescale faster than the characteristic intramolecular energy dissipation limits the number of accessible excitation pathways and thus results in a narrow resonance. Time-dependent one-color pump-probe study showed that nonadiabatic (vibron) coupling is the dominant energy dissipation mechanism for high-lying electronic excited states in C_{60}.

Zusammenfassung

Die vorliegende Arbeit beschäftigt sich mit wegbereitenden Untersuchungen von lichtinduzierter Vielteilchendynamik in komplexen Systemen. Im Rahmen der Arbeit wurde dazu eine reflektive Strahlteilungs- und Verzögerungseinheit für Pump-Probe Experimente an Molekülen in der Gasphase entworfen und gebaut. Dies erlaubt die Messung von phasenaufgelösten (kohärenten) Autokorrelationen, wobei die Kontrolle der Pump-Probe-Verzögerung mit Attosekunden-Präzision durch ein speziell entwickeltes Weißlicht-Interferometer im Vakuum erfolgt, welches die Überwachung der relativen Verschiebung der Spiegel mit wenigen Nanometern Genauigkeit ermöglicht. Weiterhin erfordern phasenaufgelöste (interferometrische) Pump-Probe-Experimente die räumliche Abbildung des Ionisationsvolumens, wofür ein Elektron-Ion-Koinzidenzspektrometer aufgebaut wurde. Es ermöglicht die gleichzeitige, koinzidente Detektion der Ionen und Elektronen mittels der Velocity-Map-Imaging-Technik (VMI) oder wahlweise auch eine räumliche Abbildung für der Ionen. Hiermit wurde die lineare Feldautokorrelation von Pulsen des Freie-Elektronen-Lasers Hamburg (FLASH) bei einer Wellenlänge von 38 nm aufgenommen.

Ein weiterer Schwerpunkt der Arbeit bestand in der energie- und zeitaufgelösten Vermessung der resonanten Zweiphotonen-Ionisation von C_{60} mit einem durchstimmbaren Kurzpulslaser im ultravioletten Spektralbereich. Es konnte gezeigt werden, dass dipolselektive Anregung auf einer Zeitskale unterhalb der charakteristischen intramolekularen Energiedissipation die Anzahl der zugänglichen Anregungspfade limitiert und daher zu einer schmalen Resonanz führt. Das Studium der Zeitabhängigkeit weist dabei auf nichtadiabatische (vibronische) Kopplung als dominanten Mechanismus der Energiedissipation aus energetisch hochliegenden, elektronisch angeregten Zuständen in C_{60} hin.

Acronyms

AOI	Angle of Incidence
ATI	Above-Threshold Ionization
BBO	Beta-Barium Borate
CCD	Charge-Coupled Device
CL	Closed Loop
DFT	Density-Functional Theory
DOS	Density of States
FAC	Field Autocorrelation
FEL	Free-Electron Laser
FERMI	Free-Electron laser Radiation for Multidisciplinary Investigations
FLASH	Free-electron Laser in Hamburg
FRIAC	Fringe-Resolved Autocorrelation
FROG	Frequency-Resolved Optical Gating
FWHM	Full Width at Half-Maximum
HHG	High-Harmonic Generation
HOMO	Highest Occupied Molecular Orbital
IAC	Intensity Autocorrelation
IP	Ionization Potential
IR	Infrared
KS	Kohn-Sham
LDA	Local-Density Approximation
LED	Light-Emitting Diode
LUMO	Lowest Unoccupied Molecular Orbital
MCP	Microchannel Plate
MPI	Multiphoton Ionization
NMED	Nonadiabatic Multielectron Dynamics

OBE	Optical-Bloch Equations
OL	Open Loop
OPA	Optical Parametric Amplifier
OPD	Optical Path Difference
PAD	Photoelectron Angular Distribution
PSD	Position-Sensitive Detector
PTB	Physikalisch-Technische Bundesanstalt
REMPI	Resonance-Enhanced Multiphoton Ionization
RMS	Root Mean Square
ROI	Region of Interest
SAE	Single-Active Electron
SAMO	Superatom Molecular Orbital
SASE	Self-Amplified Spontaneous Emission
SDU	Split-and-Delay Unit
SFG	Sum-Frequency Generation
SHG	Second-Harmonic Generation
SPIDER	Spectral-Phase Interferometry for Direct Electric-field Reconstruction
STM	Scanning Tunneling Microscopy
TDDFT	Time-Dependent Density-Functional Theory
TDLDA	Time-Dependent Local-Density Approximation
THG	Third-Harmonic Generation
TOF	Time-of-Flight
UV	Ultraviolet
VMI	Velocity Map Imaging
VMIS	Velocity Map Imaging Spectrometer
VUV	Vacuum Ultraviolet
WLI	White Light Interferometry
XUV	Extreme Ultraviolet

Contents

1 Introduction

Nonlinear optics and short pulse spectroscopy of dynamical processes in matter rely on full control of amplitude and phase of the photonic reagents driving the system far from equilibrium. At the heart of this field is the coherent interaction of the sample with light. The coherent interaction between the light wave and the quantum mechanical wave function describing the system depends on the time-frequency spectrum of the laser pulse, i.e. the spectral phases and temporal shapes. This allows not only to study its response to light stimuli, but also to control it with light. With a purposely shaped spectral and temporal profile of laser pulses one can achieve selective bond breaking in molecules, enhance the specific outcome in chemical reactions initiated by these photonic reagents or populate certain ionization pathways. For a rather complete overview of work to date on laser control of photophysical and photochemical processes, the reader is referred to some excellent recent reviews [1–3]. There is a variety of established techniques available for both, pulse shaping [4] and pulse characterization [5,6] in the visible and ultraviolet spectral range. However, for shorter wavelength it becomes much more challenging. A one-color pump-probe scheme, where a double pulse sequence is generated from a single initial pulse, can be employed for pulse characterization and also can be regarded as one of the simplest examples of pulse shaping. Typically, a femtosecond laser pulse deposits (pumps) energy into the electronic and vibrational degrees of freedom without significantly ionizing the system under investigation. Subsequently, the energy redistribution is then monitored (probed) by a delayed pulse. It is worth noting that the well-defined phase of the light field is a prerequisite for both, studying the coherent processes and controlling them, as well as provides some benefits for pulse characterization. The phase-resolved one-color pump-probe spectroscopy (i.e. autocorrelation) is easily realized in the visible range as the transmissive optics employed for generating the double-pulse sequence is readily available. For shorter wavelengths in the VUV–XUV range one has to employ reflective optics and creating a pair of pulses with identical spatial phase becomes signif-

icantly more demanding [7].

The key challenge that is addressed in the present thesis is to push the current limits of phase sensitive spectroscopies towards shorter wavelength. It will provide novel opportunities to study and possibly control energy and charge migration in systems of increasing complexity with unprecedented spatial and temporal resolution. Molecular electronic devices such as molecular junctions, molecular transistors and organic solar cells rely on charge transport channels with negligible energy dissipation during the short propagation time. Polymer solar cells are commonly composed of a photoactive film of a conjugated polymer donor and a fullerene derivative acceptor, which makes use of the fullerenes' unique ability to form stable C_{60}^- anions [8–10]. Electron correlation plays an important role in the formation of four bound states of the fullerene anion [11–13]. The build-up and decay of correlations in complex quantum systems is a an important aspect of modern physics. Since their discovery by Kroto *et al* in 1985 [14], C_{60} fullerene has attracted a lot of attention for prototypical studies, in particular after the invention of an effective isolation method by Krätschmer et al [15] that made C_{60} available in macroscopic amounts. With its special structure, 174 nuclear degrees of freedom, 60 essentially equivalent delocalized π-, and 180 structure defining localized σ-electrons neutral C_{60} may be considered a model case of a large but still finite molecular system with many degrees of freedom for electronic and nuclear motion. Because of the large charge conjugation, its finite "energy gap", and quantum confinement of electronic states, C_{60} may be viewed as an interesting intermediate between a molecule and a condensed matter system. In fact, applying solid-state concepts to the valence "Bloch electrons" on the C_{60} sphere results in an "angular band structure" [16] from which other relevant quantities (such as plasma frequencies and group velocities) can be extracted. Photo-physical studies of fullerenes using fs laser fields cover the whole range from atomic through molecular to solid state physics [17]. The molecular response is truly a multi-scale phenomenon. It ranges from attosecond dynamics in electronic excitation and ionization to statistical physics describing thermalization processes. Thus, light-induced processes in fullerenes cover more than 15 orders of magnitude in time [18]. Investigation of C_{60} in gas phase allows to study the isolated molecules free from any interaction and hence concentrate on energy deposition and dissipation. Open scientific questions are: What is the role of multi-electron effects mediating the energy flow? On which time scale is the energy redistribution taking place? What is the role of nonadiabatic coupling between electron system and nuclear backbone? The present thesis gives detailed information. The exper-

imental results are compared with theoretical studies provided by collaboration partners from Martin-Luther-Universität Halle-Wittenberg[1].

The thesis is organized as follows. Chapter 2 provides some physical background with the focus on the interaction of isolated atoms and molecules with light, in particular on the photophysics of the C_{60} molecule. Furthermore, an overview of autocorrelation techniques as tools for femtosecond laser pulse characterization and dynamic studies in pump-probe experiments is given. Chapter 3 gives a description of the experimental setup designed and constructed during the course of the present thesis, including the vacuum chamber, the reflective split-and-delay unit for phase-resolved pump-probe experiments in the VUV–XUV wavelength range and charged particle detection setup. Chapter 4 discusses the main results, i.e. energetics and dynamics study of energy dissipation processes in isolated C_{60} molecules in the light of wavelength-tunable short UV pulses and phase control on the attosecond timescale in a Michelson-type all-reflective interferometric autocorrelator using monochromatic SASE pulses from a free-electron laser at a central XUV wavelength of 38 nm. Chapter 5 presents a summary of the results and future perspectives.

[1] J. Berakdar *et al*.

2 Theoretical background

2.1 Interaction of atoms and molecules with light

The interaction of a quantum system with electromagnetic radiation depends on many parameters of both the studied system and radiation. In the scope of the present thesis pulsed light sources (lasers) were used. For laser intensities below $10^{16}\,\mathrm{Wcm}^{-2}$ the interaction process is dominated by the electric field component. At higher intensities electrons become relativistic and the magnetic field component of the field has to be taken into account. This regime is beyond the scope of the present work and will not be discussed here. Once the photon energy is absorbed by the sample it is dissipated through a number of relaxation channels that depend on the particular system under study and the properties of the laser field. There is a variety of different pathways such as transition to an excited state (electronic, vibrational or vibronic), ionization, fragmentation, just to name few of them. The ionization process is one of the most attractive to study due to the formation of charged products and their relative ease for detection. The characterization of their properties, e.g charge state, mass, energy, velocity, together with detailed laser pulse metrology, allows to pinpoint internal structure and laser-induced dynamics of the studied quantum system. In general, a detailed description of an ionization process can be very complicated even for small systems and not accessible for calculations. This section, not pretending to be complete, will give a brief description of the several important aspects of photon–matter interaction problem with focus on the ionization process.

2.1.1 Single-active electron picture

The single-active electron (SAE) model was successfully used for decades to describe ionization of small quantum systems, i.e. atoms in optical laser fields. As follows form the name, in this picture only a single, typically the most weakly bound electron, responds

to the action of the external field during the interaction event. The rest of the system is accounted for as an effective potential comprised of the potential of the nuclei and the other electrons treated as static. The important quantities for describing laser-induced ionization in the SAE picture are the ionization potential (IP) of the system U_{IP} corresponding to the minimal energy required to ionize the atom, and the ponderomotive potential U_{p} of the electric field which is the cycle-averaged energy that a free electron acquires in this field. For an oscillating field with frequency ω_L and amplitude $\mathcal{E}$ the ponderomotive potential can be expressed as [19]:

$$U_{\mathrm{p}} = \frac{e^2\mathcal{E}^2}{4m_e\omega_L^2} \tag{2.1.1}$$

with e being the electron charge, m_e the electron mass and c the speed of light. If the energy absorbed by the active electron from the external field exceeds the ionization potential U_{IP}, the system is ionized. Upon ionization the electron can absorb one or several photons. The cross-sections for these processes depend on the photon energy, system's ionization potential and its electronic structure. For photon energies $\hbar\omega_L > U_{\mathrm{IP}}$ the ionization typically occurs upon absorption of a single photon. If $\hbar\omega_L < U_{\mathrm{IP}}$ ionization requires absorption of more than one photon. For the latter case one can distinguish two limiting regimes depending on the ratio of the frequency and amplitude of the incident field to the U_{IP}: the so-called multiphoton ionization (MPI) and field ionization.

2.1.1.1 Multiphoton ionization

If the amplitude of the electric field is relatively weak ($I < 10^{14}\,\mathrm{Wcm}^{-2}$) ionization can be envisioned as a sequential absorption of multiple photons by the active electron. The electric field strength is this regime is much lower than the system's inneratomic Coulomb field and the interaction can be described by the perturbation theory. If the sample has no resonances close to the photon energy or its multiples, the ionization proceeds via virtual electronic states after coherent absorption of a number of photons and is called *nonresonant* or *direct* ionization. The ionization rate $W^{(N)}$ (probability per unit interaction time) for an N-photon nonresonant MPI process can be expressed as [20]:

$$W^{(N)} = \sigma^{(N)} F^N \tag{2.1.2}$$

where $\sigma^{(N)}$ is the intensity-independent N-photon generalized ionization cross-section specific for the sample, and $F = I/\hbar\omega_L$ is the incident photon flux. Eq. (2.1.2) breaks down at a certain saturation intensity I_{sat} corresponding to a situation where the ionization probability reaches unity [21]. Once the saturation is reached, the further growth of the ionization yield with increase of the laser intensity comes mostly from the expansion of the ionization volume (volume effect). Thus, for $I > I_{\text{sat}}$ the ionization rate departs from its $\propto I^N$ dependence and is governed by spatial and temporal properties of the laser beam. Once promoted above the IP, the quasi-free electron can further gain energy from the electric field due to the close presence of the ionic core and, in principal, can continue absorbing photons being already in the ionization continuum. In this case the MPI process is called *above-threshold ionization* (ATI) (see Fig 2.1.1). A characteristic signature of an ATI process is a series of peaks in the kinetic energy distribution spectra of emitted photoelectrons separated by the photon energy $\hbar\omega_L$.

The probability of an MPI process increases if the studied system exhibits excited states resonant with the photon energy or its harmonics. An ionization process involving population of excited states is called *resonance-enhanced multiphoton ionization* (REMPI). In this situation the ionization rate does not follow the simple law of Eq. (2.1.2). In general, the ionization cross-section $\sigma^{(N)}$ for an N-photon REMPI process has a complex form (even for relatively simple atomic systems) that depends on the photon energy, photon flux, character of involved resonances, (i.e. their number, energy spacing and width), correlation effects and energy coupling inside the system. Comparing to the direct MPI, the intensity power law of $W^{(N)}$ in a REMPI case involving the same number of photons is typically reduced from I^N to I^{N-x} with x not necessarily being an integer [22,23].

2.1.1.2 Field ionization

If the strength of the external AC field becomes strong enough (e.g. $I > 10^{14}\,\text{Wcm}^{-2}$ for hydrogen) it can periodically deform the core potential which binds the outermost (active) electron (see Fig. 2.1.1b). Then, the net potential seen by the electron in each moment of time is a superposition of the instantaneous field and the atomic potential which forms a barrier of finite width. If the field oscillation is slow comparing to the electronic motion inside the atom or molecule, the electron can tunnel through the barrier and escape from the sample (tunneling ionization). If the field strength is sufficient to completely depress the barrier below U_{IP}, the electron escapes over the barrier. This description

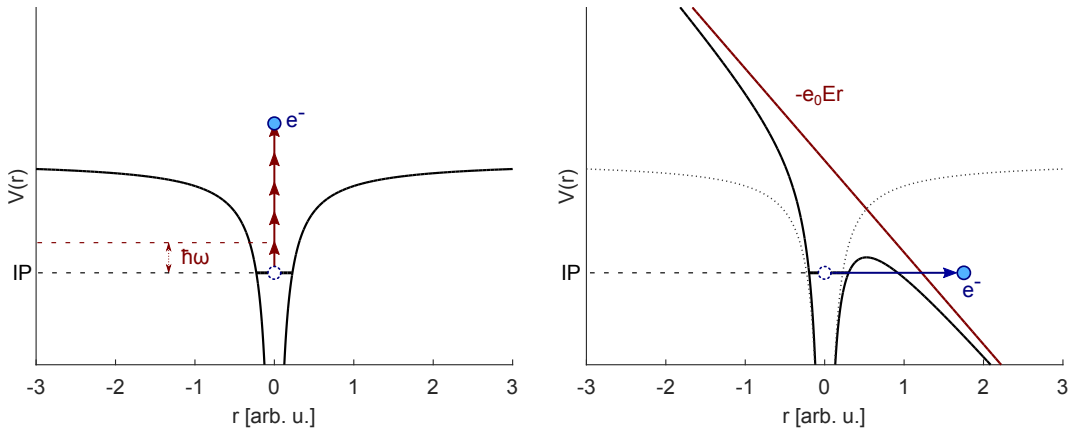

Figure 2.1.1: Two nonresonant ionization schemes: (a) multiphoton and (b) tunneling.

corresponds to the so-called *adiabatic* or *quasistatic* approximation as the barrier is essentially static for the fast moving electron. The adiabatic picture is justified for atoms and small molecules but breaks (together with the SAE concept) for larger systems with complex electronic structure (see Section 2.1.2 for details). In agreement with the above "semi-calssical" picture of the ionization process, the kinetic energy spectrum of photoelectrons has a continuous distribution for the tunneling or barrier-suppression ionization. To a good approximation the ionization process is prompt and the ejected electron carries away most of the absorbed energy. Therefore the mass spectrum of field ionized species usually shows only parent ions with a negligible amount of fragmentation.

To distinguish between the MPI and field ionization regimes one traditionally defines a dimensionless quantity called the Keldysh parameter [24]. It is proportional to the ratio of the electron tunneling time τ_{tun} through the barrier to the half-period of the oscillating electric field $T_L = 2\pi/\omega_L$ [24–26]:

$$\gamma = \sqrt{\frac{U_{\text{IP}}}{2U_{\text{p}}}} \propto \frac{\tau_{\text{tun}}}{\frac{1}{2}T_L} \tag{2.1.3}$$

For $\gamma \ll 1$ the ionization occurs in a time much shorter than the field inversion time and can be described by tunneling through or over the barrier. The case of $\gamma \gg 1$ indicates that either the external field is too weak to significantly deform the binding potential, or the oscillation frequency is too high and the the field changes its direction before the electron has time to escape. The ionization process is described then in the framework of MPI.

There is, however, no sharp demarcation line between the two regimes and when $\gamma \approx 1$ the two processes compete with each other. The photoelectron kinetic energy spectrum in this case contains ATI peaks superimposed on a continuous background. Here, the peaks can be explained in both, the multiphoton and the tunneling ionization pictures. In the latter case they appear as a consequence of interference of partial electron wavepackets emitted at different cycles of the laser pulse [27,28].

2.1.2 Nonadiabatic multielectron dynamics in complex systems

The two approximation described in the previous section—SAE and adiabatic—are successfully used for description of interaction of small quantum systems such as atoms with light. However, their validity for more complex systems is questionable. The main difference between atoms and molecules is size and the large amount of degrees of freedom of the latter. These differences lead to effects that make both of the above approximations fail.

The adiabatic approximation relies on the fact that the electronic motion inside the binding potential is much faster than the oscillation of the laser field. In this way the fast electron can instantly adjust to the slow change in the potential and remain in its eigenstate [25,26]. As the size of the system grows, the electronic orbitals become more delocalized. The electrons become "slower" and cannot adiabatically follow the field anymore [25]. This results in a nonadiabatic dynamic response. The SAE concept in turn assumes that every interaction event with the laser field involves only a single, the mostly weakly bound electron in the system. Any excitations inside the potential well and multielectron effects are neglected [26]. This approach is justified for those atomic species where multielectron excited states lie above the IP. More complex systems, e.g. polyatomic molecules, may have a large number of equivalent or nearly equivalent delocalized electrons interacting simultaneously with each other and the electric field. Such multielectron effects include electron–electron correlations and dynamic polarization.

One more aspect that contrasts molecules with atoms is the presence of nuclear degrees of freedom. Their coupling to the electronic system allows to exchange energy and opens new excitation (vibronic transitions) and ionization (thermal electron emission) mechanisms and new energy relaxation channels (i.e. fragmentation) appearing in molecules. Ionization discussed in this section is often one of the last steps in the excitation cascade. Usually, the photon energy is first absorbed by part of the electron

subsystem. Electron–electron coupling leads to energy exchange and equilibration (thermalization) within the subsystem. The timescale of this process depends on the system studied and properties of the excitation light pulse, e.g in C_{60} it occurs within ~ 70 fs. Collisional energy exchange between electrons may lead to the formation of new excited states (often multielectron), population of energy levels that cannot be reached in single-photon dipole transitions and statistical electron emission. On a longer timescale the energy is also transferred to nuclear degrees of freedom via electron–phonon coupling. In C_{60}, for example, it happens within 200–300 fs after the initial interaction with a femtosecond laser pulse [29,30]. This leads to vibrational excitation of the molecule often followed by statistical ionization and fragmentation.

Summing up, the nonadiabatic dynamics of many interacting electrons coupled to nuclear degrees of freedom makes the molecular response to fs laser fields much more complex, often rendering simple atomic approximations inapplicable.

2.2 C_{60}

The following sections give a brief description of the C_{60} molecule including its geometry, electronic structure and nuclear degrees of freedom (Section 2.2.1) and main aspects of its interaction with light (Section 2.2.2).

2.2.1 Nuclear and electronic structure

2.2.1.1 Shape

The 60 carbon atoms comprising the C_{60} molecule are arranged in vertices of a truncated icosahedron. A schematic view of the molecule is shown in Fig. 2.2.1. A regular truncated icosahedron is a highly symmetric structure with 90 edges of equal length, 60 equivalent vertices, 20 hexagonal and 12 pentagonal faces. In the C_{60} molecule each carbon atom is a vertex of one pentagonal and two hexagonal faces, which makes all the atoms essentially equivalent. Each atom is bound to three neighbors with one double bond (along the edge between two hexagons) 1.46 Å long and two single bonds (on pentagonal edges) 1.40 Å long [31]. Thus, strictly speaking, C_{60} is not a regular icosahedron (which has edges of equal length). However, the molecule is often treated as the regular one with an average edge length of 1.44 Å since the length difference between the two types of bonds is small. The outer diameter of C_{60} is 7.09 Å considering only the ion cage and 10.34 Å including the surrounding electron cloud [31]. The truncated icosahedron point group I_h (which

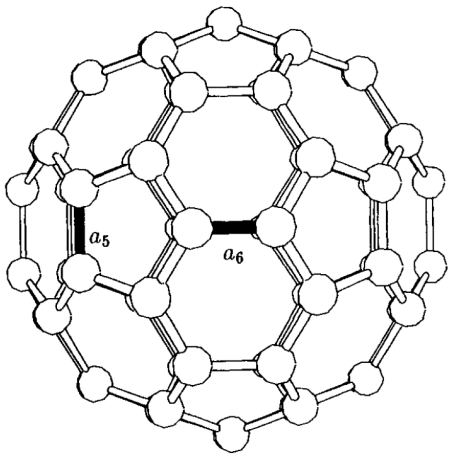

Figure 2.2.1: Schematic view of the C_{60} molecule. The single and double bonds are denoted as a_5 and a_6 accordingly. Adopted from [31].

symmetry is preserved even for the unequal edge lengths) allows 120 symmetry operations making C_{60} to possess the highest symmetry of all known molecules [31]. Many of its unique properties are the direct consequence of its high symmetry.

2.2.1.2 Nuclear degrees of freedom

An isolated C_{60} molecule has $60\times3 = 180$ nuclear degrees of freedom. Six of them (three translations and three rotations) are related to the movement of the molecule as a whole. The remaining 174 are internal degrees of freedom corresponding to different vibrational modes of the molecule. As a result of high degeneracy of an icosahedral system the 174 degrees of freedom lead only to 46 different frequency modes. They can be observed by inelastic neutron scattering, electron energy loss spectroscopy, as vibronic side bands in the photoluminescence spectra and in IR and Raman spectra [31].

Strong vibronic coupling due to nonadiabatic multi-electron dynamics (NMED) facilitates an effective energy transfer between the electron and nuclear systems in C_{60}. A_g and H_g vibrational modes play an important role in this aspect. As theoretically and experimentally demonstrated, this enables the control of vibrational motion of C_{60} by excitation with properly selected wavelength and temporal shape of the laser pulses in the optical and near-infrared spectral range [32,33].

2.2.1.3 Electronic structure

Each carbon atom has four valence electrons that form σ- and π-bonds holding the C_{60} molecule together. Three of the electrons form bonds via σ-orbitals confined mostly in the molecular cage. These orbitals are low-lying in energy and do not significantly contribute to electronic transport or optical properties of the molecule. The remaining 60 valence electrons (one per atom) hybridize into π-orbitals oriented normal to the cage structure. These delocalized electrons are energetically located near the Fermi level. They are the ones which dominate the optical response and participate in the charge transport in fullerene structures like nanotubes and quantum wells [31].

Several models were developed to calculate the electronic structure of fullerenes. They range from the one-electron Hückel method [34] to first principle calculations. Though sophisticated models give a good agreement with optical absorption, photoemission, and other experiments sensitive to the electronic structure, the simple Hückel description leads to the correct level ordering near the Fermi energy and thus provides

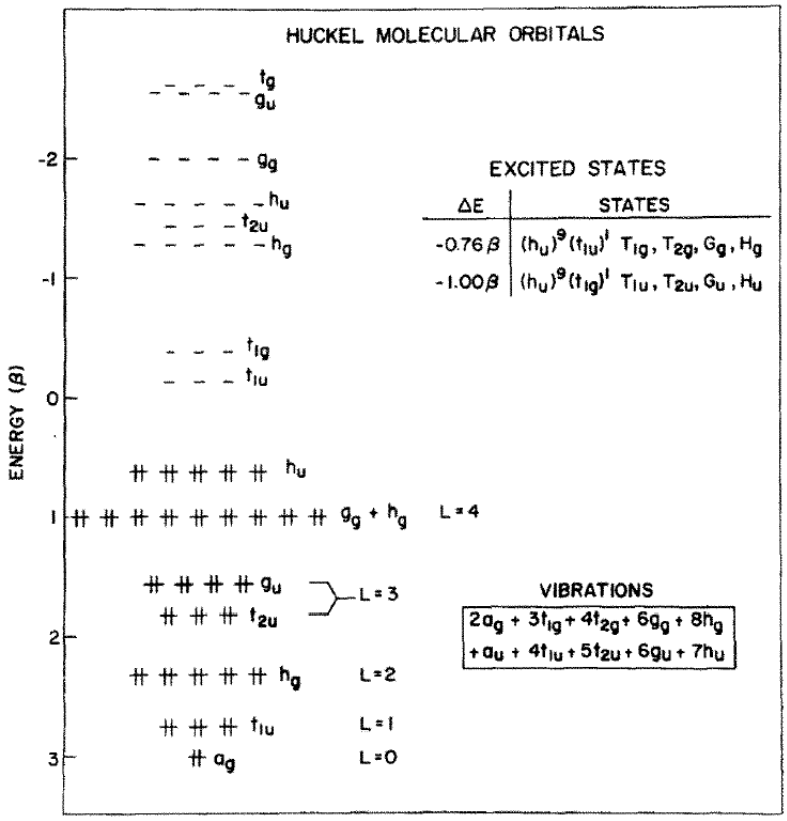

Figure 2.2.2: States of π-electrons in a free C_{60} molecule calculated with Hückel method. Occupied and unoccupied states are marked as "+" and "−" accordingly. Adopted from [34].

valuable insight into the electronic structure of fullerenes [31]. The ordering of the π-electron molecular orbitals with their notation based on the I_h group symmetry is shown in Fig. 2.2.2. The first 50 π-electrons fully occupy states with angular momenta $l = 0$–4. The remaining 10 electrons occupy states with $l = 5$ which can accommodate 22 electrons in total. These 10 electronic states correspond to the completely occupied h_u level which is the highest occupied molecular orbital (HOMO) in C_{60}. The lowest unoccupied molecular orbital (LUMO) corresponds to the t_{1u} level. In local density approximation (LDA) calculations estimate the HOMO–LUMO gap in free C_{60} molecules to be 1.79 eV [35].

2.2.2 Interaction of C_{60} with light

The response of C_{60} to light excitation demonstrates a broad range of characters, starting from effects easily explained by atomic models (e.g. ATI) and ending with multielectron

and statistical properties typical for condensed matter (e.g. thermionic emission) and metallic clusters (e.g. plasmon excitation). In this sense C_{60} bridges the gap between atoms and solids. Finally, the specific photo-induced dynamics depends solely on the properties of light: wavelength, intensity and pulse duration.

As described above, C_{60} is an example of a system with a large but finite number of degrees of freedom. Their strong coupling leads to effective energy dissipation mechanisms and allows the molecule to absorb a large amount of energy (up to several tens of eV) before disintegration. The relevant timescales of energy exchange range from fs to ns and the underlying processes are rather complicated. However, theoretical description of C_{60} is still feasible due to its high symmetry and relatively simple electronic structure. This makes C_{60} a perfect candidate for prototypical studies of ionization dynamics and energy dissipation in complex systems and a stringent test for different theoretical models. This section, without pretending to be complete, gives a brief overview of the most important aspects of C_{60} response to the excitation with light.

2.2.2.1 Multiphoton nonresonant ionization

In short, the interaction of C_{60} with nonresonant light can be described as a sequential multistep process: (i) the photon energy is absorbed by part of the electron subsystem, (ii) the energy is redistributed within the valence band via electron–electron interaction, (iii) the energy is transferred to ions via electron–phonon coupling leading to vibrational excitation. Each of the steps occurs on a different timescale. Ionization can take place at any of these steps depending on the properties of the excitation light, in particular the pulse duration. This allows to observe unique signatures of different energy exchange mechanisms in electron and ion spectra by varying the interaction time.

For nonresonant excitation shorter than the characteristic timescale for inelastic electron–electron scattering (<70 fs) the response of C_{60} is dominated by prompt ionization. At moderate intensities ($I < 6\times10^{13}$ Wcm^{-2}) the electron kinetic energy spectrum displays a series of peaks separated by the photon energy. This is a signature of the ATI process which can be readily explained in the framework of the SAE model. With increasing laser intensity, i.e. decreasing Keldysh parameter, the ATI peaks begin to disappear in the continuous background which becomes dominant as the laser intensity approaches conditions corresponding to $\gamma \approx 1$, i.e. when the SAE and adiabatic models predict that ionization proceeds via tunneling [36].

Once the pulse duration approaches the characteristic timescale of the electron–

electron interaction (~ 100 fs), the ATI peaks in the electron spectrum of C_{60} start to disappear even if intensity-wise the system is still in the MPI regime according to the Keldysh theory. This behavior can be explained using the Weisskopf statistical theory [37] as follows. On the timescale of ~ 100 fs the photon energy, first absorbed by small part of the electron subsystem, thermalizes within the valence band via inelastic electron–electron scattering which leads to the creation of a hot electron gas with temperatures up to several thousand K [29,37]. An electron can be then statistically evaporated from the hot valence band of the molecule (which is still vibrationally cold) in a process called *thermoelectronic emission*. Due to energy equilibration within the electron bath, this ionization mechanism produces a smooth thermal background which obscures the distinct ATI peaks observed at shorter pulse durations and similar intensities thus making the kinetic energy spectrum smooth.

The electron–phonon coupling in C_{60} was experimentally found to take place on the order of 200–300 fs after the initial photoabsorption [30,37]. Interaction with laser pulses longer than this value leads to strong vibrational excitation of the molecule. At corresponding pulse durations energy is absorbed by the electron system at a relatively low rate leaving sufficient time for electron–phonon energy exchange during the pulse and thus leading to efficient heating of the ionic cage. Ionization then takes place in a process called *thermionic emission*, i.e. evaporation of the electron from a vibrationally hot molecule. As with the discussed above thermoelectronic emission, this process is statistical by nature and produces electrons with a continuous kinetic energy distribution, but lower temperatures comparing to the former. The thermionic emission can take place on a ns–µs timescale, i.e. long after the excitation pulse is over [38–40]. This delayed ionization is commonly observed in systems with ionization potentials lying below the dissociation energies [37] and is indicated in the time-of-flight mass spectrum as a characteristic tail behind the main peak. The vibrational heating of the molecules also leads to a strong fragmentation which, in case of C_{60}, occurs via a sequential loss of neutral C_2 units by the parent ion and results in formation of fragments C_{60-2n}^{q+} with even number of atoms [17].

2.2.2.2 Resonances and multielectron effects

Resonances play an important role in excitation and energy transfer processes. In the optical wavelength range the absorption spectrum of C_{60} is dominated by transitions between the valence π-states (see Fig. 2.2.3). The HOMO $\rightarrow$ LUMO ($h_u \rightarrow t_u$) transition

is dipole forbidden since these states have the same parity. Thus, the first strong absorption peak corresponds to the dipole allowed HOMO → LUMO+1 ($h_u \rightarrow t_{1g}$) transition at ∼3.75 eV [41]. Experiments demonstrate that the t_{1g} state plays a key role in energy coupling between electronic and nuclear degreed of freedom of C_{60}. For example, fragmentation of C_{60} is greatly enhanced if the excitation energy (e.g. 3.1 eV) is close to the HOMO → LUMO+1 transition [17,30]. This points towards an efficient energy transfer from the electronic to the nuclear system mediated by excitation of t_{1g}. Furthermore, this state was also found to be crucial for the population of Rydberg series [42]. These states can be excited in a broad spectral range (400–800 nm) but the exact population mechanism still remains unknown. Pump-probe and temperature-dependent studies showed that the resonant HOMO → LUMO+1 transition together with the vibrational excitation of the molecule plays a key role in their population [43,44]. The proposed concept is that t_{1g} acts as a "doorway" [45] for a complex energy exchange processes between electronic and vibrational degrees of freedom through nonadiabatic coupling of many electrons to nuclear motion. It creates a broad band of electronically excited states that serves as a base for populating Rydberg series via multiphoton absorption.

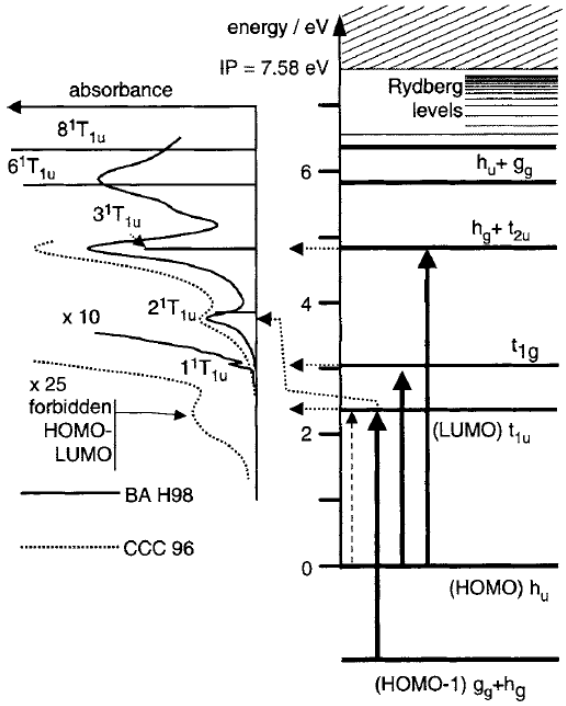

Figure 2.2.3: Optical absorption spectrum of C_{60} and the single-electron energy diagram. Figure from [17].

C_{60} is a manybody quantum system with many delocalized electrons and it is crucial to understand whether its response to light is dominated by single- or multielectron effects. Theoretical calculations predict that even at low intensities many electrons are excited during the interaction with a femtosecond laser pulse [46,47]. The experimental observation of ionization saturation intensities that are higher than those predicted by the conventional SAE model seem to support this picture. However, the data can be explained by both, invoking the multielectron effects [48] and using the SAE model, albeit with modifications accounting for the size of the molecule [49]. The question is under which conditions the single- or the multielectron response dominates the interaction. For example, it was found that for a sub-10 fs pulse excitation the single ionization of the neutral molecule is dominated by the SAE behavior, while the multiple ionization occurs via nonadiabatic multielectron dynamics with possible involvement of the plasmon resonance [50]. The plasmon resonance is probably the most notable multielectron effect in C_{60} and will be discussed in details in Section 2.2.2.4.

2.2.2.3 Superatom molecular orbitals

In 2008 Feng *et al* investigated C_{60} monolayers deposed on a metal substrate using scanning tunneling microscopy (STM) [51]. They discovered new unoccupied diffuse states in C_{60}, which hybridize like s- and p-orbitals of hydrogen with principal quantum number $n = 3$ and form nearly free-electron bands in one- and two-dimensional C_{60} assemblies. The spatial electron density distribution of these states resemble that of the atomic orbitals of hydrogen and alkali atoms (Fig. 2.2.4). Hence, the new states were named *super-atomic molecular orbitals* (SAMOs). SAMOs are bound to the core of the hollow C_{60} molecule rather than to the individual atoms like the known π-orbitals confined mostly to the atomic cage. The origin of the binding potential is the screening charge of the excited electron, a property expected for hollow-shell molecules. Recently SAMOs were revealed in free fullerenes as well by means of velocity map imaging (VMI) [52]. The kinetic energy spectra and photoelectron angular distributions obtained after ionization of isolated molecules with fs laser pulses in the visible range show good agreement with the properties of SAMOs calculated by means of time-dependent density-functional theory (TDDFT). The binding energy of the lowest member of the family, the s-SAMO, was found to be ~ 1.9 eV. It must be noted that SAMOs were identified not only in C_{60} but also in C_{70}, which corroborates that these states are not specific for C_{60} but are a general property of hollow molecules. From a molecular point of view SAMOs can be

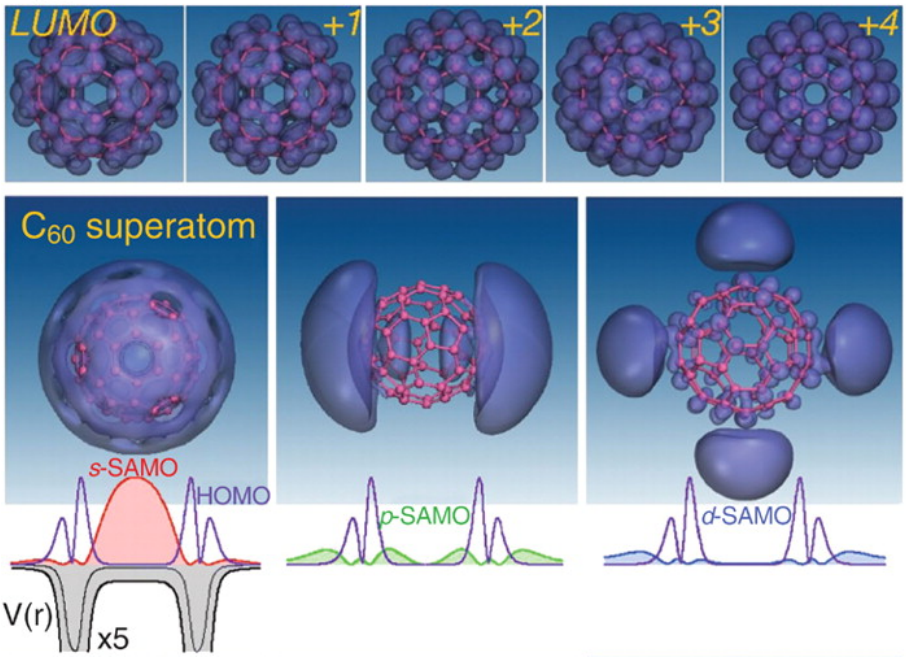

Figure 2.2.4: Spatial electron density distributions of π-orbitals (LUMO–LUMO+4) and s-, p-, d-SAMOs in a free C_{60} molecule. Adopted from [51].

regarded as low-lying mixed valence Rydberg states [53]. However, in contrast to the latter, a significant amount of the electron density of SAMOs is confined within the nuclear cage.

As with the Rydberg series, the population mechanism of SAMOs in fullerenes is not yet clear. Experimental observations show that SAMOs can be excited by fs laser pulses in a wide range (2–3.1 eV) of visible light [54]. The mismatch of the photon energy and SAMO–HOMO energy gaps presumes that these states are populated not via direct multiphoton transitions but through some internal conversion mechanism, possibly involving "doorway" states. The ionization of SAMOs is similar to that of Rydberg series and occurs due to the absorption of an additional photon. Despite the fact that fullerenes have a high density of states in the SAMO energy range, these diffuse orbitals dominate in the photoelectron spectra because their relative photoionization rates are much higher than those of energetically similar π-states for visible light.

SAMOs form delocalized bands in molecular assemblies upon bonding which implies their potential usefulness in molecular electronics [55] and also for new functionalities such as current carrying states and hence nanometer-sized magnetic field generators [56]. Though, in neutral molecules their energy lies above the Fermi level which can be

seen as a handicap for applications, it was shown theoretically that their energy can be decreased by doping the molecules with metal atoms [57]. We note in passing that recently SAMO states have been observed in planar, non-fullerene materials as well [58,59].

2.2.2.4 Giant plasmon resonance

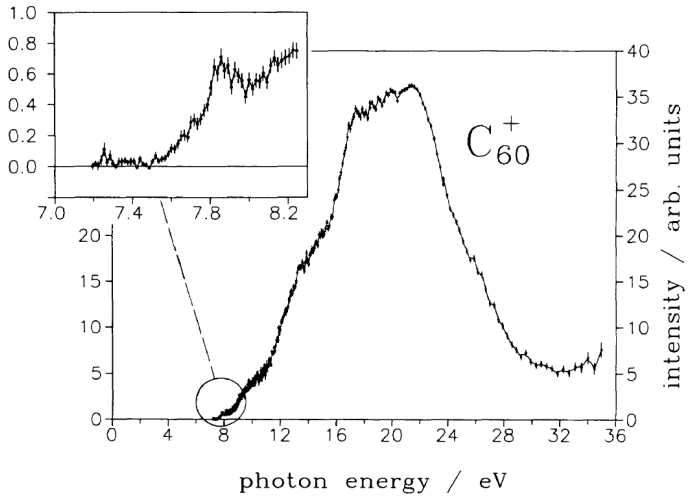

Figure 2.2.5: Experimental C_{60}^+ ion yield as a function of incident photon energy displaying an excitation of the giant plasmon resonance. Figure from [60].

Plasmons, i.e. a collective motion of electrons, are known from systems with a large amount of delocalized electrons such as metallic clusters [61]. Due to the delocalized valence electrons fullerenes, and C_{60} in particular, can be seen as small conducting spheres and are expected to display some metallic properties. The existence of the collective multielectron excitation similar to plasmons was first predicted for C_{60} by Bertsch *et al* using linear-response theory [62]. In contrast to metal clusters which have plasmon excitations in the optical range, the C_{60} plasmon resonance lies far above the IP and is directly coupled to the continuum. Thus, autoionization of the molecule is expected soon after the excitation. The first experimental observation of the resonance by means of excitation energy–resolved photoionization was reported by Hertel *et al* [60]. The plasmon manifests itself as a broad band in the ionization cross-section with a peak at ~ 20 eV and a full width at half maximum (FWHM) of 10 eV (Fig. 2.2.5). In a later experiment performed in the extended energy range Scully *et al* identified a second absorption band peaked at ~ 40 eV [63]. In a complementing theoretical study using time-dependent local density approximation (TDLDA) the authors interpreted the first peak at 20 eV as a surface plas-

mon and the second peak at 40 eV as a volume plasmon. In classical terms the surface plasmon can be understood as the oscillation of the constant electron density build up from both, π- and σ-states, with respect to the ionic cage. By contrast, the volume plasmon can be seen as a radial compression of electron density and involves mostly σ-electrons. The existence of two plasmon resonances is a characteristic property of finite-size metallic clusters [18] which underlines the special properties of C_{60}. The large width of the resonance assumes that the collective oscillation lives shorter than a femtosecond before the autoionization takes place. The corresponding electron dynamics has not been observed experimentally yet. Theory predicts that this collective excitation has a complex multipole nature which can be possibly revealed by angular-resolved electron energy-loss spectroscopy [64]. Recent theoretical (employing TDLDA) [65,66] and experimental (using VMI) [66] studies showed that the plasmon resonance in C_{60} has a strong effect on the angular distribution of photoelectrons emitted from the HOMO and HOMO-1 valence states. The calculations demonstrate that the field-induced dynamic polarization of the molecule (surface plasmon) affects the ionized electron through a screening potential which exhibits a strong energy-dependent variation in the range of 17–22 eV. This variation affects phases of the free-electron partial waves interfering in the continuum and is imprinted in photoelectron angular distributions (PADs) detected by the VMI spectrometer. The phases can be used to extract the so-called Wigner time delay [67] related to the attosecond dynamics of the ionization process (photoemission delay) [66]. The underlying physics suggests that this effect is not specific to C_{60}, but can be generic for any system that exhibits a plasmon resonance in the ionization continuum [65]. We note in passing that the plasmon resonance is also responsible for interesting properties C_{60} exhibits in the high-harmonic generation (HHG) process. It was shown experimentally that the frequency cut-off is extended comparing to the prediction of the SAE model, and the intensity of harmonics lying in the vicinity of the resonance is enhanced [68].

2.3 Autocorrelation methodologies

As was said in Chapter 1, short laser pulses are an important tool for the investigation and control of matter. Since the temporal structure of the pulse defines the timescale and outcome of the interaction process, its characterization is crucial and became a separate field of research. In general, characterizing a short event $E(t)$ constitutes in measuring its response to a known function $G(t)$, which we will call *gate*. Mathematically, the response can be expressed as a convolution of the event and the gate in time domain:

$$S(\tau) \propto \int_{-\infty}^{+\infty} E(t)G(t-\tau)\,\mathrm{d}t. \tag{2.3.1}$$

For the exact determination of the signal the gate must be infinitely short, i.e. $S(\tau) = E(\tau)$ only if $G(t)$ is the delta function. The laser pulse itself is often already the shortest event available to the experimentalist, thus, one approach is to use it as a gate. Substituting $E(t)$ instead of $G(t)$ in Eq. (2.3.1) gives what is called *linear autocorrelation*, the most straightforward version of a large family of techniques which has been used for laser pulse characterization for the last several decades. The next sections will give a brief overview of some of these techniques and are organized as follows. Sections 2.3.1 and 2.3.2 give concepts of linear and second-order autocorrelation. Section 2.3.3 gives a brief description of more advanced pulse characterization methods. In Section 2.3.4 special aspects of autocorrelation experiment realization with reflective optics are discussed. Section 2.3.5 describes the application of the autocorrelation approach to study excitation and relaxation dynamics of matter as a one-color pump-probe method.

2.3.1 Field autocorrelation

For the sake of simplicity the analysis in Sections 2.3.1 and 2.3.2 will deal only with the time dependence of the electric field $\mathbf{E}(x, y, z, t)$ neglecting its vector nature:

$$\mathbf{E}(x, y, z, t) \equiv E(t) = \mathcal{E}(t)\cos(\omega_0 t + \varphi(t) + \varphi_0), \tag{2.3.2}$$

where $\mathcal{E}(t)$ is the time-dependent amplitude (envelope), ω_0 is the carrier wave frequency and $\varphi(t)$ is the time-dependent phase. It is conventional to express the real physical

quantity E using the concept of a complex electric field:

$$E(t) = \frac{1}{2}\left(\tilde{E}(t) + \tilde{E}^*(t)\right), \tag{2.3.3}$$

where tilde and asterisk mark the complex quantity and the complex conjugate accordingly. The complex electric field can be expressed as [6]:

$$\tilde{E}(t) = \mathcal{E}(t)\mathrm{e}^{-\mathrm{i}(\omega_0 t+\varphi(t)+\varphi_0)} = \tilde{\mathcal{E}}(t)\mathrm{e}^{-\mathrm{i}\omega_0 t}, \tag{2.3.4}$$

with $\tilde{\mathcal{E}}(t)$ being the complex amplitude incorporating the time-dependent phase.

The simplest autocorrelation experiment with light beams is the so-called *amplitude* or *field autocorrelation* (FAC) that can be realized using a Michelson interferometer. The sketch of the experiment is shown in Fig. 2.3.1a. A short light pulse, which shall be

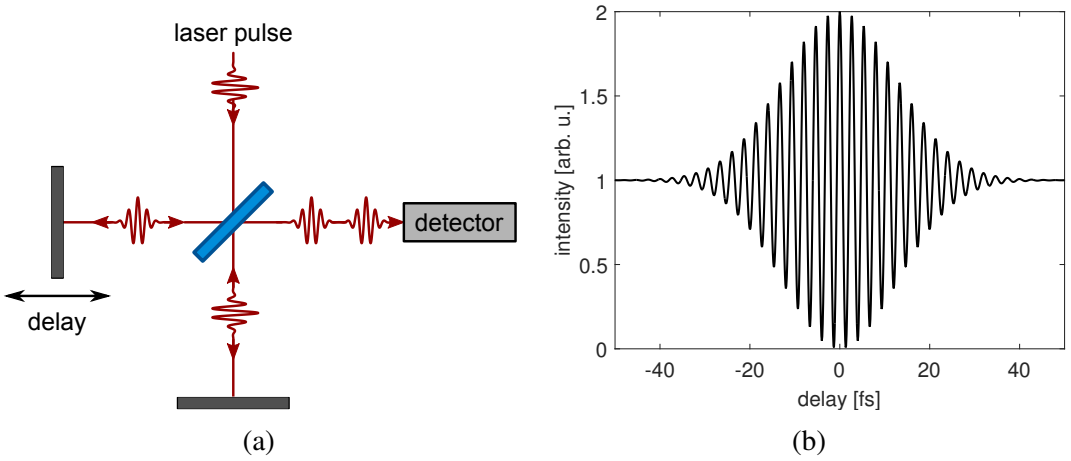

Figure 2.3.1: (a) Schematic layout of a Michelson interferometer for field autocorrelation; (b) autocorrelation signal of a 15 fs Fourier-limited 800 nm laser pulse recorded by the detector.

characterized, is split in two equal replicas that are directed to different arms of the interferometer with mirrors at the end of each arm. After reflection the replicas are collinearly recombined and sent to a linear detector. One of the mirrors can be moved along the beam propagation direction thus varying the optical path difference (OPD) between the pulses. Overlapped in space, the two pulse replicas will undergo interference depending on the relative phases of their electric fields. The detector response is always slow comparing to the pulse propagation and it cannot resolve the instantaneous signal. It will measure the

integrated signal instead:

$$S_{\mathrm{FAC}}(\tau) \propto \int_{-\infty}^{+\infty} \left[E(t) + E(t-\tau)\right]^2 \mathrm{d}t$$
$$= \int_{-\infty}^{+\infty} E^2(t)\,\mathrm{d}t + \int_{-\infty}^{+\infty} E^2(t-\tau)\,\mathrm{d}t + 2\int_{-\infty}^{+\infty} E(t)E(t-\tau)\,\mathrm{d}t, \tag{2.3.5}$$

where $E(t)$ is the electric field of a single pulse replica after passage through the interferometer and τ is the delay between the pulses. The first two terms in the above expression form a constant background and are independent contributions of each of the pulses separately. The last term is essentially Eq. (2.3.1) with $G(t) = E(t)$. It describes the interference of the pulses overlapped in time. Introducing a function $G_1(\tau)$:

$$G_1(\tau) \equiv \int_{-\infty}^{+\infty} \tilde{\mathcal{E}}(t)\tilde{\mathcal{E}}^*(t-\tau)\,\mathrm{d}t \tag{2.3.6}$$

and adopting a normalization:

$$\int_{-\infty}^{+\infty} \mathcal{E}^2(t)\,\mathrm{d}t = 1, \tag{2.3.7}$$

Eq. (2.3.5) can be rewritten as:

$$S_{\mathrm{FAC}}(\tau) \propto 1 + \mathrm{Re}\left\{G_1(\tau)\mathrm{e}^{\mathrm{i}\omega_0\tau}\right\} \tag{2.3.8}$$

with ω_0 being the carrier envelope frequency of the laser pulse. The oscillating term is often called the *interferogram* of the light source and its envelope $G_1(\tau)$—the *autocorrelation function*. According to Wiener-Khinchin theorem, the Fourier transform of $G_1(\tau)$ gives the source power spectrum, i.e. $\mathcal{F}\{G_1(\tau)\} = \left|\tilde{\mathcal{E}}(\omega)\right|^2$ [69]. Hence, the autocorrelator shown in Fig. 2.3.1 gives essentially the same information as any spectrometer and is often called Fourier-spectrometer. The knowledge of the power spectrum, however, is insufficient to recover the pulse shape. In general, the reconstruction of a temporal waveform from its spectrum is known as the so-called one-dimensional phase-retrieval problem, which is an ill-posed problem with an infinite number of solutions [5]. In application

to the FAC this means that there are infinitely many temporal shapes which correspond to a given spectrum. The unique determination of the pulse shape requires knowledge of its spectral phase as well. With only the spectrum in hand one has to make assumptions about the phase which strongly handicaps the application of FAC for pulse reconstruction. On the other hand, dependence of $S_{\mathrm{FAC}}(\tau)$ on the OPD between the interferometer arms enables to use FAC for profile characterization of rough surfaces with a nanometer resolution (see Section 3.4.2 for details).

2.3.2 Nonlinear autocorrelation

As was shown in the previous section, the linear autocorrelation can provide only the pulse spectrum. Nonlinear correlation techniques can give information about the pulse temporal structure. One of the ways is to introduce a nonlinear medium to the output of the interferometer used in the previous section (Fig. 2.3.2). The incident electric field $E(t)$ induces a time-dependent polarization $P(t)$ of the medium, which can be expressed as a power series of the applied field [70]:

$$\begin{aligned} P(t) &= \epsilon_0 \left[\chi^{(1)} E(t) + \chi^{(2)} E^2(t) + \chi^{(3)} E^3(t) + ... \right] \\ &\equiv P^{(1)}(t) + P^{(2)}(t) + P^{(3)}(t) + ..., \end{aligned} \tag{2.3.9}$$

where $\chi^{(n)}$ is the n-order susceptibility of the medium and ϵ_0 is the vacuum permittivity. For simplicity the above formula omits the vector nature of the field and assumes that the polarization is driven by the instantaneous electric field (the so-called *parametric process*). As a response the medium will emit a time-dependent electric field defined by the dominant terms of the decomposition (2.3.9) for the given material. For example, if the medium exhibits the second order nonlinearity $P^{(2)}(t) \propto E^2(t)$, it will generate light at twice the input frequency. This process is called second-harmonic generation (SHG). The incident field on the SHG crystal placed behind the interferometer can be written as $E_{\mathrm{inc}}(t,\tau) = E(t) + E(t-\tau)$, where $E(t)$ is the electric field of a single pulse replica. The output of the SHG process will be $\propto E^2_{\mathrm{inc}}(t,\tau)$. The light of the fundamental frequency remaining after passing through the crystal can be filtered out and the detector

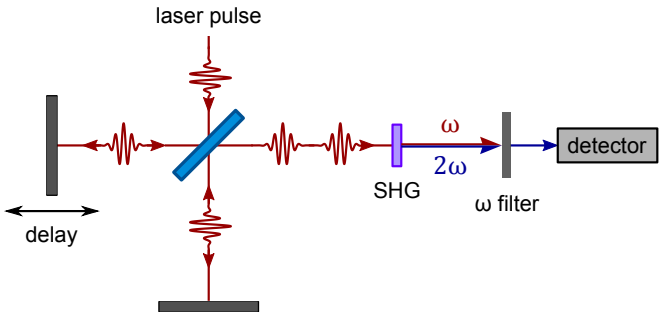

Figure 2.3.2: Schematic layout of a Michelson interferometer for a fringe-resolved second-order autocorrelation.

will record only the second-harmonic signal [6]:

$$\begin{aligned} S_{\mathrm{FRIAC}}(\tau) &\propto \int_{-\infty}^{+\infty} \left[(E(t) + E(t-\tau))^2 \right]^2 \mathrm{d}t \\ &= \int_{-\infty}^{+\infty} E^4(t)\,\mathrm{d}t + \int_{-\infty}^{+\infty} E^4(t-\tau)\,\mathrm{d}t \\ &\quad + 6 \int_{-\infty}^{+\infty} E^2(t) E^2(t-\tau)\,\mathrm{d}t \\ &\quad + 4 \int_{-\infty}^{+\infty} E(t) E(t-\tau) \left[E^2(t) + E^2(t-\tau) \right] \mathrm{d}t. \end{aligned} \tag{2.3.10}$$

The obtained signal is called *fringe-resolved intensity autocorrelation* (FRIAC). Adopting a normalization:

$$\int_{-\infty}^{+\infty} \mathcal{E}^4(t)\,\mathrm{d}t \equiv 1, \tag{2.3.11}$$

Eq. (2.3.10) can be recast as:

$$S_{\mathrm{FRIAC}}(\tau) \propto 1 + 2G_2(\tau) + 2\mathrm{Re}\left\{ F_1(\tau) \mathrm{e}^{\mathrm{i}\omega_0\tau} \right\} + \mathrm{Re}\left\{ F_2(\tau) \mathrm{e}^{\mathrm{i}2\omega_0\tau} \right\}, \tag{2.3.12}$$

where:

$$G_2(\tau) \equiv \int_{-\infty}^{+\infty} \mathcal{E}^2(t)\mathcal{E}^2(t-\tau)\,\mathrm{d}t, \tag{2.3.13a}$$

$$F_1(\tau) \equiv \int_{-\infty}^{+\infty} \tilde{\mathcal{E}}(t)\tilde{\mathcal{E}}^*(t-\tau)\left[\mathcal{E}^2(t)+\mathcal{E}^2(t-\tau)\right]\mathrm{d}t, \tag{2.3.13b}$$

$$F_2(\tau) \equiv \int_{-\infty}^{+\infty} \tilde{\mathcal{E}}^2(t)\tilde{\mathcal{E}}^{*2}(t-\tau)\,\mathrm{d}t, \tag{2.3.13c}$$

and ω_0 is the carrier frequency of the pulse. As with the FAC in Eq. (2.3.8), the FRIAC signal consists of a constant background defined by the incoherent action of each pulse and additional terms arising from their overlap in the medium. The decomposition (2.3.12) shows that $S_{\mathrm{FRIAC}}(\tau)$ contains three "principal" frequencies: 0, $1\omega_0$ and $2\omega_0$. Their envelopes, $G_2(\tau)$, $F_1(\tau)$ and $F_2(\tau)$, can be extracted from the measurement by taking the Fourier transform of $S_{\mathrm{FRIAC}}(\tau)$, selecting the datasets around each principal frequency and performing the inverse Fourier transform of each dataset. This is not a problem if all the three components are well separated in frequency domain, which is typically the case. The exceptions are very short, few cycle, pulses with broad bandwidths which may cause the envelopes to overlap and thus hinder their identification.

The function $G_2(\tau)$ is the phase-averaged *intensity autocorrelation* (IAC) and carries information about the intensity envelope of the pulse $I(t) = \mathcal{E}^2(t)$. Assumption-free reconstruction of $I(t)$ from $G_2(\tau)$ is impossible because deconvolving a function from its autocorrelation is similar to the above mentioned one-dimensional phase-retrieval problem. What this function gives exactly is the RMS length of the pulse, which does not carry information about any fine structure of the intensity envelope [5]. The intensity autocorrelation alone can be obtained in a separate experiment if the two beams with wavevectors $\mathbf{k}_1$ and $\mathbf{k}_2$ are focused on the nonlinear medium in a noncollinear geometry as shown in Fig. 2.3.4. In this geometry the medium will emit the second-harmonic light in three directions: $\mathbf{k}_1$, $\mathbf{k}_2$ and $\mathbf{k}_1 + \mathbf{k}_2$. The last signal occurs only if the pulses overlap in time and thus contains no background. This light results from the momentum conservation and is the one of interest. However, the interference fringes disappear due to spatial phase averaging (see Section 2.3.4 for details) and a detector placed in the direction $\mathbf{k}_1 + \mathbf{k}_2$ records $S_{\mathrm{IAC}}(\tau) \propto G_2(\tau)$. The benefit of this scheme is that it provides $G_2(\tau)$ directly and can

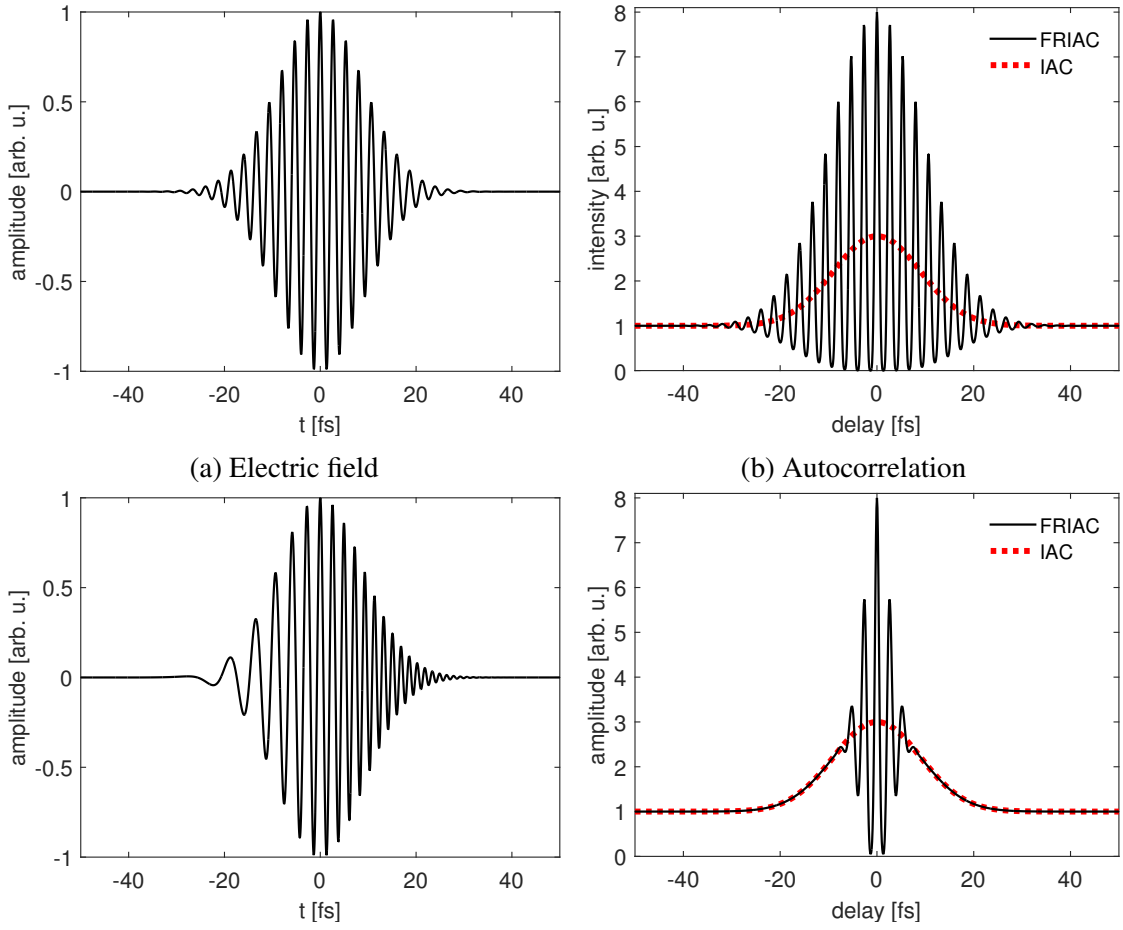

(a) Electric field (b) Autocorrelation

(c) Electric field (d) Autocorrelation

Figure 2.3.3: Two Gaussian pulses with $\lambda = 800\,\text{nm}$ and $\tau_{\text{FWHM}} = 20\,\text{fs}$ and their autocorrelation functions. (a), (b): Fourier limited pulse and its FRIAC trace. (c), (d): linearly chirped pulse and its FRIAC trace. The red curves show phase-averaged functions (i.e. IAC) which are the same for both pulses.

be used for single-shot measurements. Due to the relative wavefront tilt of the two beams and the absence of the background the temporal delay between the pulses is mapped on the transverse spatial distribution of the second-harmonic signal, i.e. $S(\tau) = S(x)$. Thus, recording the SHG signal with transverse spatial resolution enables to get the single-shot IAC data which can be desirable if the laser source has shot-to-shot fluctuations of energy or the pulse shape.

The last two terms in the Eq. (2.3.12) describe the interference of the pulse replicas. $F_1(\tau)$ oscillating at ω_0 is the interferogram of the fundamental frequency multiplied by a time-dependent amplitude factor. This term is produced by intensity modulation

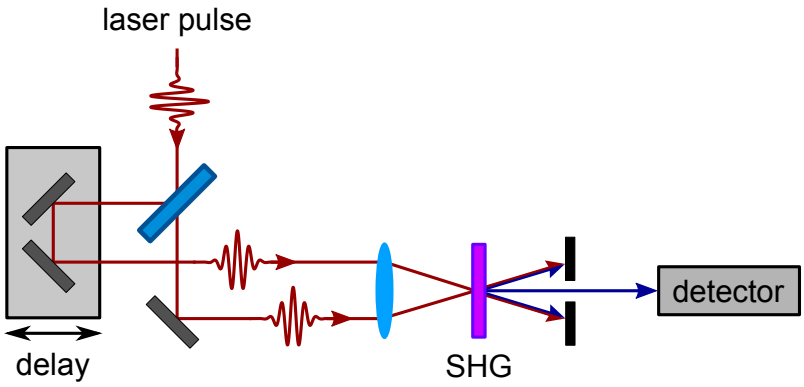

Figure 2.3.4: Noncollinear intensity autocorrelation setup.

in the nonlinear medium resulting from the interference of the initial pulses. The last term in Eq. (2.3.12) is the interferogram of the second-harmonic field, i.e. $F_2(\tau)$ is the second-harmonic autocorrelation function. Its Fourier transform directly provides the second-harmonic spectrum $\mathcal{F}\{F_2(\tau)\} = \left|\tilde{\mathcal{E}}^2(\omega)\right|^2$. For Fourier-limited pulses $G_2(\tau) = F_2(\tau)$ holds. An example of a temporal chirp affecting the FRIAC signal is illustrated in Fig. 2.3.3.

It was shown by Naganuma *et al* that the knowledge of the three functions $G_1(\tau)$, $G_2(\tau)$ and $F_2(\tau)$ is sufficient to reconstruct the original pulse without any assumptions [71]. The only unknown is the time direction because the autocorrelation function is symmetric by definition. This means that the chirp of the pulse can be quantified but its direction (sign) remains unknown. The maximum of the FRIAC amplitude $S_{\mathrm{FRIAC}}(0) = 8$, showing that the peak to background contrast of the fringe resolved autocorrelation is 8:1, which serves as a good check for the accuracy of the measurement.

2.3.3 Other pulse characterization techniques

Though in theory the original pulse can be reconstructed from a FRIAC measurement, this technique has never become popular in the laser science for pulse characterization. The reason is that the FRIAC measurement is much more sensitive to the spectrum than to the temporal pulse shape. Thus, difference between FRIAC traces of pulses with different shapes but equal spectra can be subtle which makes the pulse reconstruction challenging in practice [72]. There are more powerful and reliable techniques used in the femtosecond laser community. The two main families are: spectrally-resolved correlation techniques known as *frequency-resolved optical gating* (FROG) [5,73], and the so-called *shear inter-*

ferometry techniques, e.g. SPIDER [74].

FROG setups may have many different geometries but all of them essentially give a measurement of a *spectrogram* $S(\tau,\omega)$—the spectrally-resolved cross-correlation of the studied pulse with some gate function. This involves the measurement of the spectrum for each correlation delay τ, which turns the one-dimensional phase-retrieval problem encountered in frequency integrating techniques into a two-dimensional phase-retrieval problem. It has a unique solution and thus enables assumption free reconstruction of the pulse intensity $I(t)$ and phase $\varphi(t)$. Two examples of FROG using the pulse itself as the gate, the so-called SHG FROG [5] and interferometric FROG (IFROG) [75], are the natural extensions of IAC and FRIAC into the frequency domain. It was shown that with the choice of a suitable nonlinear process FROG can be applied for pulse characterization in VUV/XUV spectral range [76,77].

Shear interferometry, another method widely used for reconstruction of ultrashort pulses, involves only frequency domain measurements and does not require a time-dependent scan. It measures the spectrum of the interference signal of the studied pulse $E(t,\omega)$ with its replica $E(t+\tau,\omega+\Omega)$ shifted in time and frequency by constant values τ and Ω. Therefore, this method is suitable for single-shot measurements. It was successfully used in the XUV spectral range to measure the temporal profile of femtosecond pulses from a seeded FEL [78].

2.3.4 Spatial effects

For the sake of simplicity the analysis in the previous sections considered the pulse propagation as a one-dimensional problem depending only on t, i.e. the spatial dependence and polarization were neglected. Such treatment misses some important aspects that will be discussed in the present section. The interference fringes observed in Fig. 2.3.1b and 2.3.3 depend on: (i) temporal and spatial coherence of the original pulse and (ii) how the two pulse replicas are superimposed in time and space. The maximum coherence of the original pulse does not guarantee that the fringes will be observed in the experiment. Interference of two pulses depends on the phase difference $\Delta\varphi$, which is, in general, a function of space and time, i.e. $\Delta\varphi = \Delta\varphi(x,y,z,t)$. Since any measurement constitutes in signal integration (i.e. averaging) over a certain area or volume and a certain time window, the exact form of $\Delta\varphi(x,y,z,t)$ becomes important. Thus, if the phase averaging (in spatial or time domain) occurs during the measurement procedure, the oscillating

terms $F_1(\tau)$ and $F_2(\tau)$ in Eq. (2.3.12) may loose contrast or vanish completely. In a perfectly collinear second-order autocorrelator $\Delta\varphi(x, y, z)$ is constant and the interference depends only on the delay τ. This allows to obtain an interferometric signal with relative ease. However, even in this case temporal phase averaging may occur if the setup is unstable and τ fluctuates on a timescale much smaller than the detector integration time. A collinear second-order autocorrelator will record in this case $S(\tau) \propto 1 + 2G(\tau)$—the so-called intensity autocorrelation with a background. It has the peak to background contrast of 3:1 instead of 8:1 in the fringe-resolved case. If $\Delta\varphi(x, y, z)$ varies, phase averaging may also occur in spatial domain, e.g. when the beams are overlapped at some angle like in the noncollinear IAC (Fig. 2.3.4). When two beams intersect at an angle θ, they form an interference pattern in the intersection area. An example of such pattern, which is often called *light-induced grating* [79], is shown in Fig. 2.3.5. The grating is characterized by

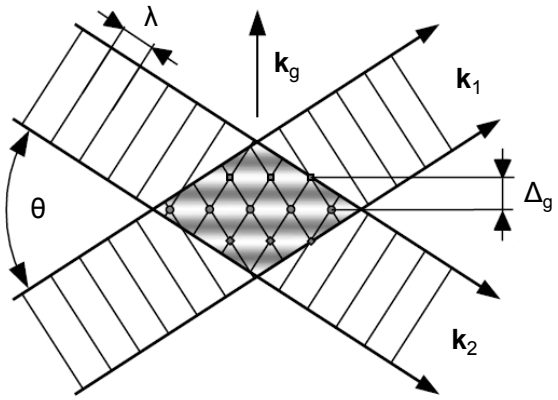

Figure 2.3.5: Interference pattern grating formed by two beams linearly-polarized perpendicular to the image plane. Adopted from [79].

the grating vector $\mathbf{k}_g = \mathbf{k}_1 - \mathbf{k}_2$, where $\mathbf{k}_1$ and $\mathbf{k}_2$ are the wavevectors of the intersecting beams. If $|\mathbf{k}_1| = |\mathbf{k}_2|$ the grating period Δ_g along $\mathbf{k}_g$ depends on the wavelength and the intersection angle as:

$$\Delta_g = \frac{\lambda}{\sin\theta}. \tag{2.3.14}$$

In the autocorrelation experiment one of the beams can be delayed by τ, which will affect the interference pattern. Though the grating period Δ_g remains fixed, positions of minima and maxima will "scroll" inside the beam intensity envelope along $\mathbf{k}_g$ depending on the temporal delay τ between the two beams. For optical wavelengths and angles of 5–10 °

(which are typical for noncollinear IAC setups) Δ_g is in the order of several microns. In the same time, a typical focus size of the laser beam is several tens of microns. The detector recording the second harmonic signal that propagates in the direction $\mathbf{k}_{2\omega} = \mathbf{k}_1 + \mathbf{k}_2$ will integrate over the complete beam profile containing many grating periods. Thus, the phase sensitive terms $F_1(\tau)$ and $F_2(\tau)$ will average to zero.

The collinear overlap of the beams in a FRIAC setup for the optical range is provided by a transmissive beam splitter which is not available for VUV/XUV frequencies. This compels to use reflective optics for short wavelengths. A common approach is to use a split-and-delay unit (SDU) based on a mirror divided in two parts. One half can be displaced along its normal and delay a half of the incident beam (see Fig. 2.3.6a). In the

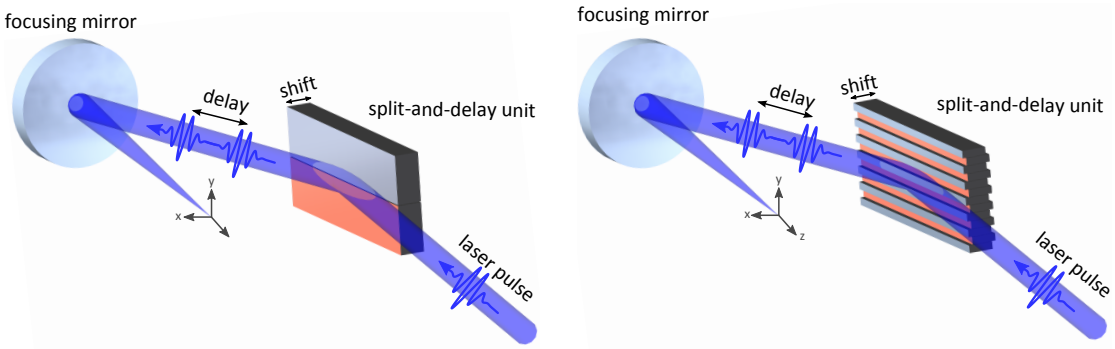

(a) (b)

Figure 2.3.6: Outline of two reflective split-and-delay unit designs: (a) conventional double split mirror and (b) strip array mirror.

context of the autocorrelation experiment it is essentially an example of a noncollinear geometry discussed above. Let us consider the propagation of each half of the beam separately. The left column in Fig. 2.3.7 shows intensity profiles of the half-beams right after reflection from the SDU and the right column their respective intensities and phases after focusing. The relative wavefront tilt will lead to a "grating-like" interference pattern once the beams are superimposed in the focal area. The skew angle between the beams is relatively small and under tight focusing conditions only one interference period fits into the beam profile. The transverse beam intensity in the focal plane for different temporal delays between the beams is shown in Fig. 2.3.8a. Mashiko *et al* showed that upon integration of the second order signal over the complete beam profile (ROI area in Fig. 2.3.8)

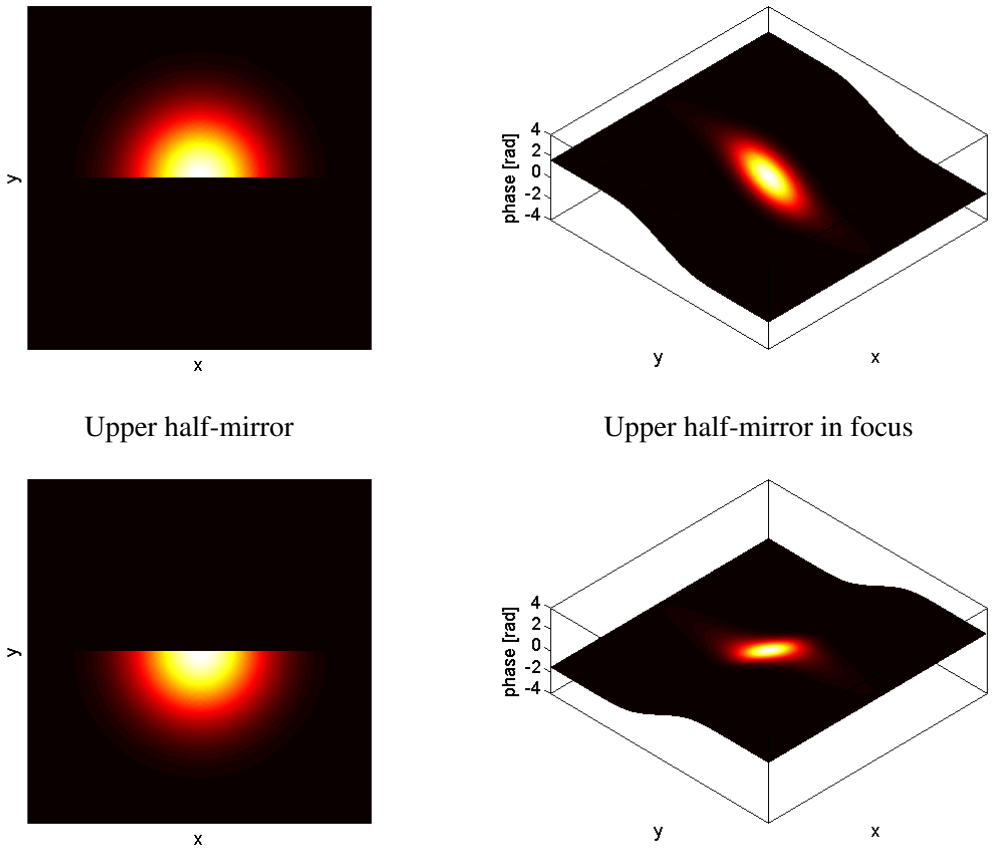

Figure 2.3.7: Intensity profiles of the beam $I(x, y)$ after the reflection from two halves of the double-mirror SDU (left) and in focal plane (right). Color designates intensity and the surface tilt in the focus images is the phase.

$F_2(\tau)$ vanishes completely and the amplitude of $F_1(\tau)$ is substantially reduced [80]:

$$S_{\mathrm{FRIAC}}(\tau) \propto 1 + 2G_2(\tau) + 0.812\,\mathrm{Re}\left\{F_1(\tau)\mathrm{e}^{\mathrm{i}\omega_0\tau}\right\} \tag{2.3.15}$$

The signal integrated over the ROI area in Fig. 2.3.8a as a function of delay is shown in Fig. 2.3.8b. Though the interference fringes are still present, they come from the remaining $\mathrm{Re}\{F_1(\tau)\mathrm{e}^{\mathrm{i}\omega_0\tau}\}$ term. Thus, spatial phase averaging leads to loss of information required for the unambiguous pulse reconstruction. This also has implications for coherent control applications which require a fixed phase difference between the pulses in the signal integration area (Section. 2.3.5).

A solution to the phase tilt problem is to split the wavefront equally symmetric across

the beam profile using plane strip-array mirrors (see Fig. 2.3.6b). In practice this can be realized with double comb reflectors [7] or slotted ones [81]. Each reflector acts like a grating generating several diffracted beams that form a sequence of spots in the focal plane (Fig. 2.3.8c). The spatial phases of the beams $\varphi(x, y)$ originating from the two gratings are identical for a given diffraction order which makes their overlap equivalent to a collinear geometry with a transmissive beam splitter. Hence, if the experimental setup allows to resolve the orders in the focal plane it is possible to obtain the FRIAC measurement restricting the signal detection area to a single diffraction order. The separation of the diffraction orders in the focal plane depends on the light wavelength, the grating period and the focal length of the focusing element. In first approximation it can be estimated using a grating equation. The diffraction of a monochromatic beam with a wavelength λ from a single strip-mirror with a period d is described as [82]:

$$m\lambda = d\left(\sin\alpha + \sin\beta_m\right), \tag{2.3.16}$$

where m is the diffraction order, α and β_m are the angles of incidence and diffraction counted from the surface normal. For the SDU arrangement shown in Fig. 2.3.6b the strips are oriented parallel to the incidence plane, i.e. $\alpha = 0$. The displacement of the m^{th} diffraction order with respect to the 0^{th} order along the dispersion plane in the focus of a focusing mirror with a focal length f is:

$$\Delta_m = f\tan\beta_m. \tag{2.3.17}$$

For VUV/XUV wavelength and gratings with periods on the order of μm the diffraction angles are small, i.e. $\tan\beta \approx \sin\beta$. Combining Eqs. (2.3.16) and (2.3.17) then gives:

$$\Delta_m = \frac{m\lambda f}{d}. \tag{2.3.18}$$

The above formula gives a convenient "rule of thumb" for estimating the strip-array SDU performance for a given experimental setup. The focal intensity distribution, of course, depends not only on the grating period and propagation distance but also on the beam parameters (size, wavefront error), focusing aberrations (e.g. astigmatism) and surface quality of optical elements. The last point becomes especially crucial as the wavelength decreases. Thus, an accurate prediction of the autocorrelator performance requires a fully numerical treatment of the beam propagation (an example is shown in Section 3.4.1.2).

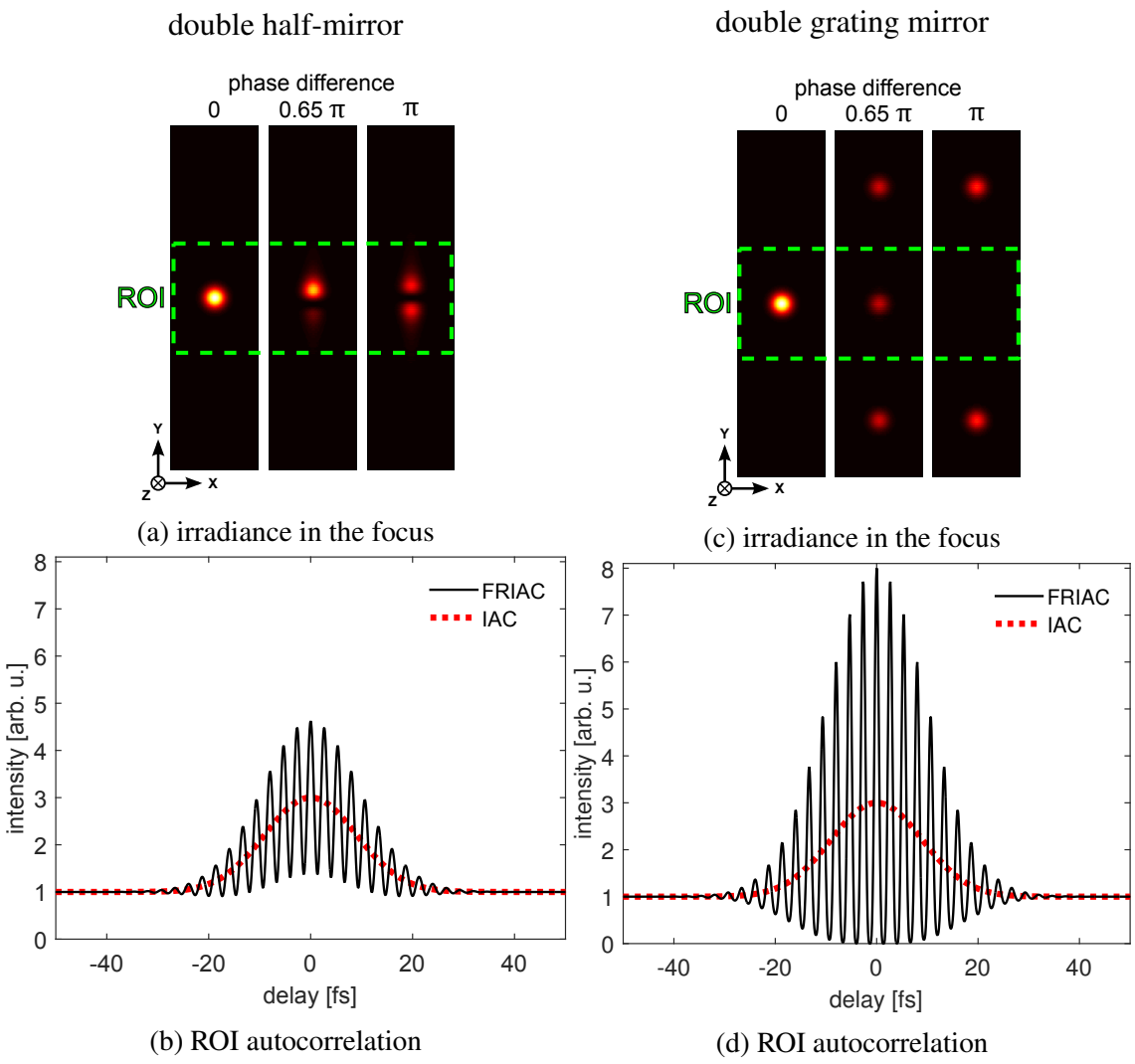

Figure 2.3.8: Top: comparison of the transverse intensity profile in the focal plane as a function of different phase delays between two beams for two SDU configurations: conventional double split-mirror (left) and strip-array mirror (right). Bottom: the corresponding fringe-resolved autocorrelation signals obtained by integrating the signal over the ROI area for each delay (solid lines) and phase averaged signals—IAC (dashed lines).

2.3.5 Two-photon photoionization for second-order autocorrelation

Pulse characterization techniques based on correlation methods (autocorrelation, cross-correlation, FROG) require a nonlinear response to the original pulse which is then analyzed. SFG, SHG or THG used in the optical domain are the so-called *parametric processes*, i.e. their response to the incident electric field is instantaneous [70], which makes them perfectly suitable for pulse diagnostics. However, the wavelength range where these processes can be generated is limited. For a nonlinear autocorrelation at short wavelengths, e.g. in the VUV/XUV spectral range, one has to choose a different nonlinear process (often nonparametric) for this role. Two examples are nonlinear ionization and two-photon fluorescence. The fact that these processes are nonparametric means that their yield in the correlation experiment depends not only on the properties of the laser pulse, but also on light–matter interaction dynamics, which is often rather complicated. In this sense the autocorrelation scan becomes a pump-probe experiment in which the first pulse changes the state of matter and the second one probes its evolution. The recorded yield is then a convolution of the laser pulse temporal shape with the dynamic response of the sample. Some processes, such as nonresonant direct MPI, are characterized to a large extend by the instantaneous response to the incident light (see Eq. (2.1.2)). Their yield has the same delay dependence as for an optical parametric process of equal order. Hence, they can be employed for pulse characterization in wavelength regions where conventional parametric processes are not available [77]. Other processes, e.g. REMPI, may show very rich and complicated dynamics which will be encoded in the measured pump-probe signal. Provided that the temporal structure of the laser pulse is known, some characteristic properties of the light–matter interaction, such as the lifetime of intermediate states, can be extracted from the pump-probe data. This makes autocorrelation methods attractive to gain information on light–matter interaction processes.

The pump-probe technique is based on promoting the sample into a transient unstable state with one (or several) photons and then probing the evolution of this state with another photon (or photons), possibly of a different color, delayed in time. The excited state is a nonstationary superposition state that evolves in time. The sample's memory of the first excitation step has two components: energy and phase, i.e. the population of the transient state(s) and its coherence. The latter one is an important aspect of the light–matter interaction which forms the basis for coherent control experiments. Both, populations and coherences tend to decay with time due to inelastic and elastic scattering

and energy transfer processes. There are several ways to model the temporal evolution of a system upon excitation. Typically, the system's phase memory is rather short. If it is much shorter than the excitation laser pulse, then the interaction with the electric field can be considered incoherent. In this case the time evolution can be described by rate equations in a form:

$$\frac{\mathrm{d}}{\mathrm{d}t} N_n = A(t) - \Gamma_n N_n, \tag{2.3.19}$$

where N_n is the population of the state $|n\rangle$, $A(t)$ is the pump rate and Γ_n is the population decay rate. The time-dependent pump rate contains the electric field envelope and accounts for photon-induced transitions from the lower lying states. Γ_n is the rate of the population loss as a result of various processes, e.g. inelastic collisions and spontaneous emission.

If the phase memory of the system is longer or comparable to the excitation pulse, the rate equation model for populations cannot give an accurate prediction of the system response. The interaction with light will depend on the relative phases of the excited electronic wavepackets evolving in time and the laser field in each particular moment, i.e. it becomes coherent. There is more than one way to model coherent processes. The examples are solving the Schrödinger equation directly or using the density matrix formalism. The latter, in a form of Optical-Bloch equations, is an attractive approach for its lower computational costs. The detailed description of this method is given in Appendix B. In the following it will be briefly summarized. A quantum system with n states can be described by an $n \times n$ density matrix $\hat{\rho}$. The elements of the density matrix evolve in time according to the Liouville-von-Neumann equation [83]:

$$\frac{\mathrm{d}}{\mathrm{d}t} \rho_{mn} = -\frac{\mathrm{i}}{\hbar} \left[\hat{H}, \hat{\rho}\right]_{mn} - \Gamma_{mn}\rho_{mn}. \tag{2.3.20}$$

The diagonal elements ρ_{nn} represent the populations of the corresponding states. The off-diagonal elements ρ_{mn} are called *coherences* and are related to coherent superpositions of states. In contrast to the rate equations, the populations ρ_{nn} are coupled to the electric field not directly but via the coherences ρ_{mn}. Therefore, the probability of the atom to undergo a transition depends on the phase difference between the incident field and the oscillating average dipole moment $\langle\hat{\mathbf{d}}\rangle$ reflected in ρ_{mn} [84].

As an example it is instructive to examine two-photon ionization of an electronic

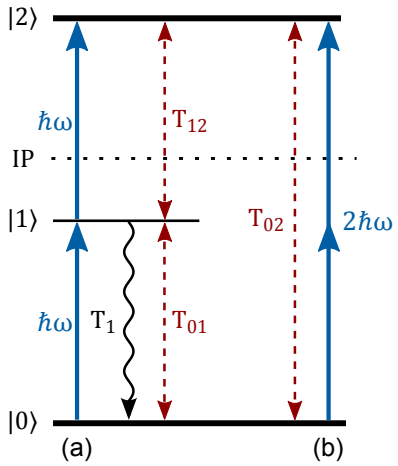

Figure 2.3.9: Resonant two-photon ionization scheme of a three-level system with linear (a) and nonlinear (b) ionization pathways, with marked coherence and population decay times T_{mn} and T_1 accordingly.

three-level system by a sequence of two short coherent laser pulses with photon energy $\hbar\omega_L$. The system contains the occupied ground state $|0\rangle$, unoccupied transient state $|1\rangle$ and the unoccupied final state $|2\rangle$ located in the ionization continuum. The neighboring states are separated by the energy gap equal to $\hbar\omega_L$ (Fig. 2.3.9). The ionization of this system may occur via two pathways: in a direct transition $|0\rangle \xrightarrow{2\hbar\omega} |2\rangle$ or in a sequential transition $|0\rangle \xrightarrow{\hbar\omega} |1\rangle \xrightarrow{\hbar\omega} |2\rangle$ creating a transient population on level $|1\rangle$. The two photons required for ionization may be absorbed either from the same pulse (pump *or* probe) or from different pulses (pump *and* probe). The light field will couple all three energy levels and besides creating the transient population, it will induce polarizations (coherences) between the states. The coherences will oscillate at frequencies corresponding to the energy gaps between the levels. In the discussed resonant case these will be ω_L for one-photon coupling ($|0\rangle$ and $|1\rangle$, $|1\rangle$ and $|2\rangle$) and $2\omega_L$ for two-photon coupling ($|0\rangle$ and $|2\rangle$). The population and coherences will decay with characteristic times T_1, T_{01}, T_{12} and T_{02}. If the excitation pulses are coherent, the population of the final state $|2\rangle$ (ionization yield) will oscillate as a function of the delay due to a combination of optical and quantum interferences. If the coherence times are long enough, the quantum interference will be manifested as oscillations in the ionization yield in the delay region free from the optical interference caused by the pulse overlap. The illustration is given in Fig. 2.3.10. The decaying population in state $|1\rangle$ manifests itself as broadening of the pump-probe trace (exponential wings) comparing to the FRIAC of the laser pulse.

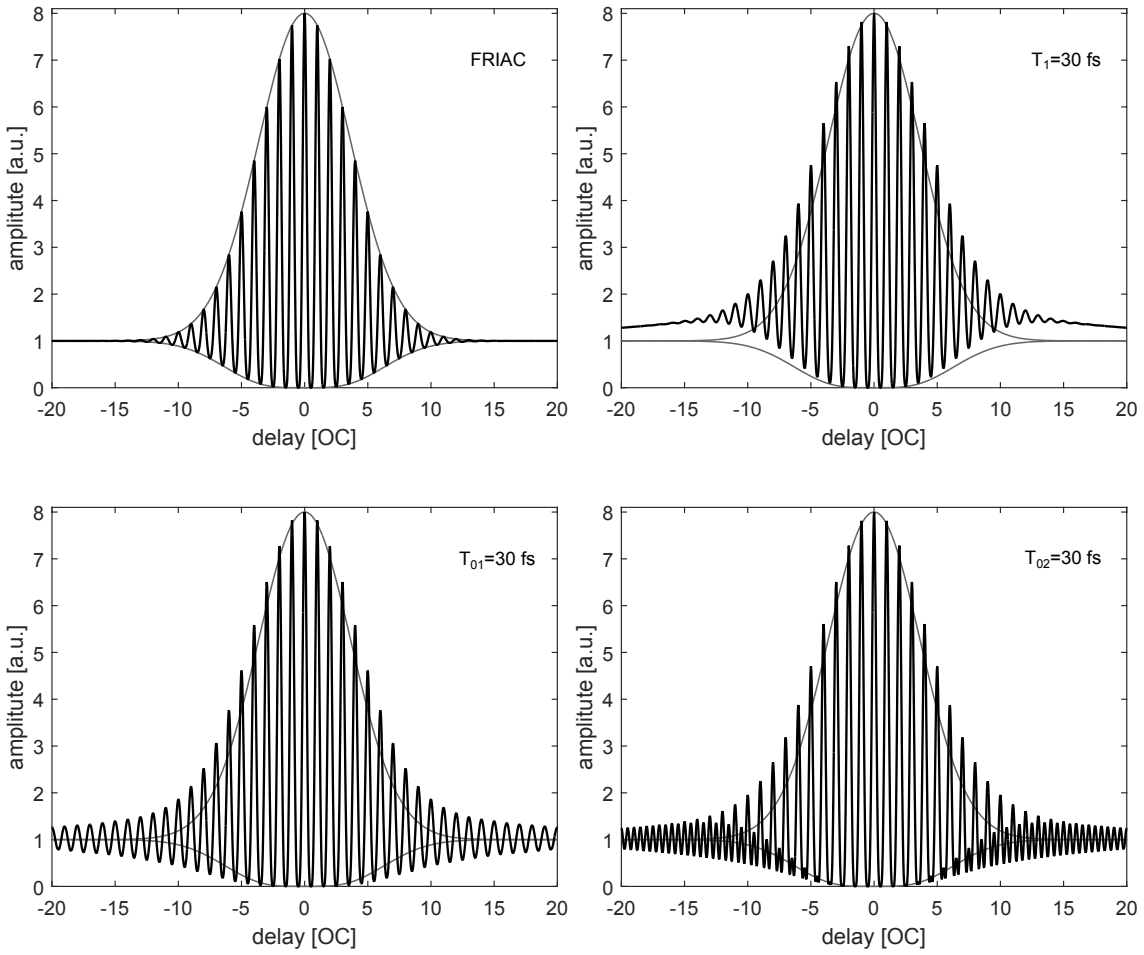

Figure 2.3.10: FRIAC of 800 nm, 15 fs FWHM Gaussian pulse and solutions of OBE for the three-level system ionized by this pulse for different values of the relaxation constants T_1, T_{01} and T_{02}. The thin gray lines mark the upper and lower envelopes of the FRIAC function. The pump-probe delay is shown in optical cycles λ/c.

Information on the population and phase decay rates can be obtained from the pump-probe delay scan if the temporal structure of the pulse is known. This can be done by fitting the solution of OBE to the measured data, or using a simpler method suggested by Nessler *et al* [85]. In short, the measured pump-probe delay scan is decomposed into the three frequency envelopes centered at zero, ω_L and $2\omega_L$ in the Fourier domain, and then the envelopes are fitted with functions that are convolutions of the corresponding envelopes of the laser pulse FRIAC with symmetric exponentials $\mathrm{e}^{-|\tau|/T_{mn}}$ describing the phase and the population decays. The characteristic lifetimes T_{mn} are found as free fit parameters. It must be noted that the mutual coherence of the two laser pulses in the

ionization volume is a prerequisite for distinguishing the phase and population relaxation dynamics. The phase integrated measurement, e.g. in noncollinear geometry, will display the overall broadening of the signal comparing to the laser pulse IAC, but will not allow to separate the different contributions.

3 Experimental setup

3.1 Vacuum chamber

Experiments involving the ionization of gas-phase molecules by VUV/XUV laser pulses and subsequent detection of interaction products require a high vacuum environment with residual gas pressures below 10^{-6} mbar. Design and commissioning of a vacuum setup was part of the present work.

The experimental apparatus comprises two main parts: a commercial CF160 cube and a CF250 cylindrical chamber of custom design. The cube serves as an ionization chamber, while the cylinder houses in-vacuum optics (detailed description is given in Section 3.4) containing a split-and-delay unit (SDU) and focusing optics. The front side of the cube is used as the entrance for the laser beam. The back side is connected to the optics chamber leaving four other sides free for mounting a molecular beam source (Section 3.2), a setup for detecting ionization products (Section 3.5) and a vacuum pump. The laser beam passes through the cube into the optics chamber where it is split into a pump-probe sequence of two pulses and then back-focused into the center of the cube where the intersection of femtosecond VUV/XUV pulses with the molecular beam takes place. The optics chamber is a 400 mm long CF250 tube equipped with five side flanges used for connection with the cube, attachment of electronic feedthroughs for in-vacuum manipulators and as viewports for diagnostics of the SDU by means of white light interferometry (Section 3.4.2). The outline of the chamber is presented in Fig. 3.1.1. The chamber is mounted on a movable support. The support provides 100 mm of translation in horizontal and vertical directions, and enables rotation of the CF250 cylinder around its axis in a range of $\pm 10\,^{\circ}$. The vacuum infrastructure consists of a scroll pump (Edwards nXDS10i) and a turbomolecular pump (Pfeiffer HiPace 700M). The SDU developed for the interferometric experiments is extremely sensitive to vibrations, hence the turbomolecular pump was chosen to have a fully active magnetic bearing which excludes any contact of ro-

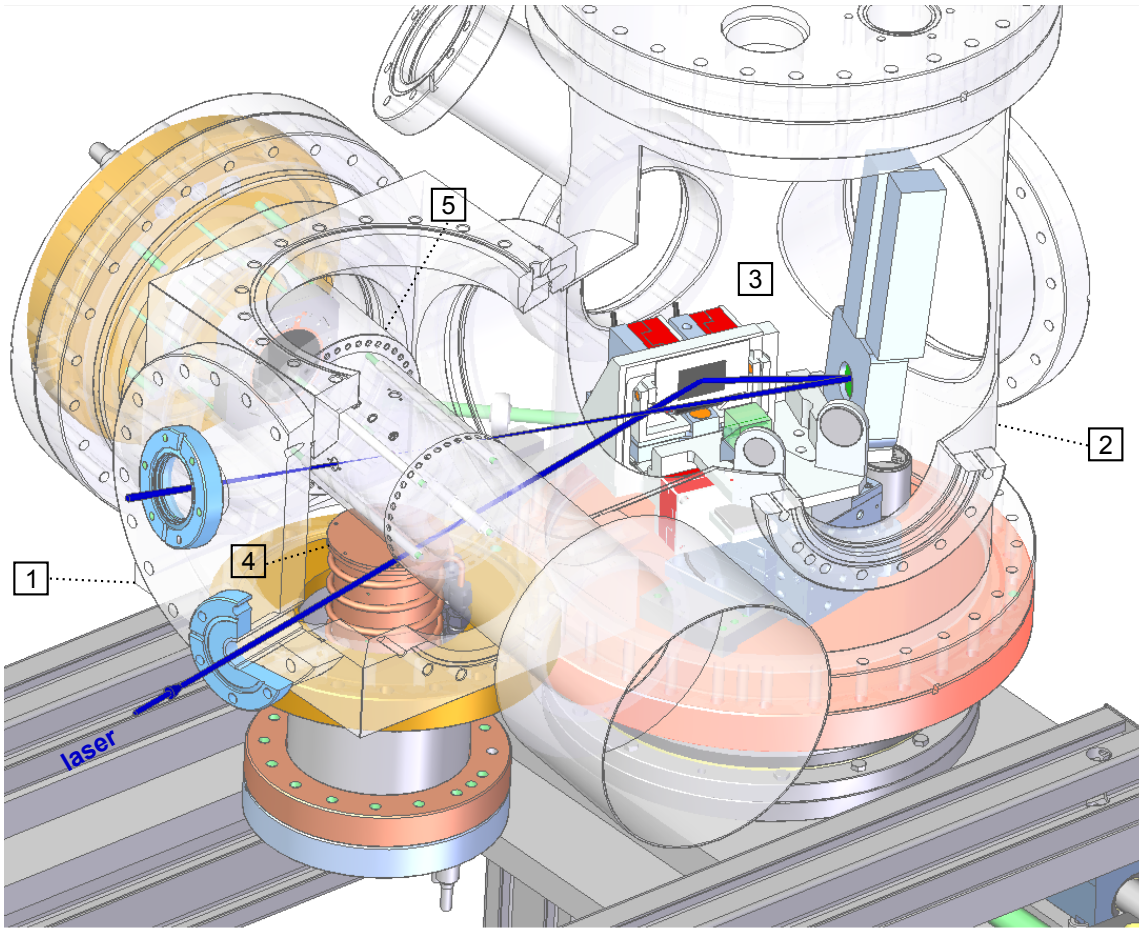

Figure 3.1.1: Outline of the vacuum chamber and components of the experimental setup. In the drawing are shown: 1—CF160 cube, 2—CF250 cylinder chamber, 3—in-vacuum optics with manipulators, 4—molecular beam source, 5—charged particle detection setup. The dark blue line indicates the beam path of the short-wavelength pulses. A detailed description of each component is given in the corresponding section of the thesis.

tors with static parts of the pump during operation. The assembled setup, including the chamber, support, pumps and inner components weights $\approx 200\,\mathrm{kg}$.

3.2 Molecular beam source

Ionization experiments with atoms or molecules in the gas phase often require intense and well collimated molecular beams. The simplest molecular beam source consists of a reservoir filled with gas or vapor which has an aperture (an orifice or a slit) for the release of the molecules. Optionally, a collimating system can be installed behind the reservoir, which, together with the reservoir's aperture, defines the geometry of the produced beam. The main parameter defining the flow of the gas (vapor) escaping from the source is the so-called Knudsen number Kn equal to the ratio of the mean free path of the molecules λ to the aperture size d, i.e. $Kn = \lambda/d$. This number defines whether the gas behavior is described by statistical or continuous mechanics. Therefore, there are two regimes of gas expansion—effusive (molecular) flow and hydrodynamic (continuous) flow—realized at two distinct limiting scenarios. In case $Kn \gg 1$ ($d \ll \lambda$) the number of collisions between particles as they leave the source approaches zero, their interaction can be neglected and the particle flow rate depends only on the pressure difference between the volumes separated by the source's aperture, vapor density and the geometry of the collimating system. This is the so-called effusion or molecular flow regime described by statistical mechanics. In the limit $Kn \ll 1$ ($d \gg \lambda$) the internal friction in the gas starts to play role and the expansion is in the hydrodynamic flow regime which is described by continuous mechanics [86]. Typically, molecular beams produced in this regime by methods like supersonic jet expansion are more intense and well collimated comparing to those obtained from effusive beam sources. However, for the present experiment the beam intensity and divergence provided by an effusive source are sufficient and hence the continuous flow regime will not be discussed.

At room temperature fullerenes have a form of solid powder due to their low vapor pressure of $\sim 9 \times 10^{-20}$ mbar [87]. To transfer them into the gas phase with a sufficient density higher temperatures are required. Photoionization experiments with C_{60} typically require temperatures in the range of 420–500 °C, which correspond to vapor pressures of 10^{-4}–10^{-3} mbar [87]. To achieve these temperatures a resistively heated oven was developed in the Laarmann group. The oven includes a sample capsule, temperature sensor, ceramic housing for the capsule, heating element and an outer casing used for mounting. The components of the device are shown in Fig. 3.2.1. The sample capsule is a blind-ended $35 \times 14\,\mathrm{mm}^2$ stainless steel cylinder with 0.5 mm thick walls. Once the sample is filled inside, the capsule is closed by a lid with an orifice that can have

different diameters (1–3 mm) and which serves as the first aperture of the source. The capsule is wrapped by a 0.5 mm thick temperature sensor wire and placed inside a 50 × 15 mm alumina housing. The outer surface of the housing has a helical thread which

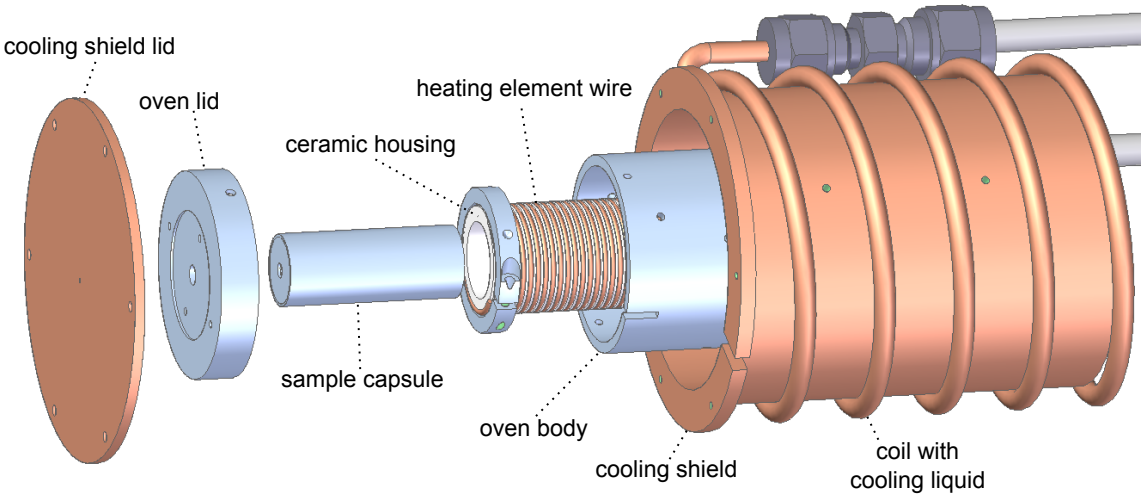

Figure 3.2.1: The resistively heated oven used for evaporation of fullerenes. Fixing screws used to assemble all the components together and the temperature sensor are omitted.

serves as a guideway for the heating wire wound around. The ceramic cylinder with the capsule, heating element and temperature sensor are placed inside a stainless steel oven body that has attachments for mounting. Also the lid of the body can have different apertures with diameters 1, 2 or 3 mm, that together with the orifice of the sample capsule form a collimator. The distance between the capsule orifice and the outer body aperture is variable in a range 5–18 mm and is used to control the effusive beam shape and intensity. In order to reduce heating of ambient parts of the chamber, the oven is placed inside a copper housing that acts as a cooling shield cooled by water or liquid nitrogen. The lid of the shield has a 1 mm orifice and is the last aperture of the molecular beam source The distance between the oven and the shield orifice can be varied from 1 to 5 mm providing the total collimator–source distance variation 6–23 mm.

From kinetic theory of gases the mean free path of molecules inside a volume can be expressed as [88]:

$$\lambda = \frac{1}{n\sigma\sqrt{2}}, \tag{3.2.1}$$

where σ is the particle collision cross-section and n is the density of particles inside the volume. Assuming ideal gas conditions with pressure P and temperature T, n can be

expressed as:

$$n = \frac{P}{kT}, \tag{3.2.2}$$

with Boltzmann constant k. At a typical evaporation temperature of $T = 775\,\mathrm{K}$ the vapor pressure of C_{60} is $\approx 2.7 \times 10^{-3}$ mbar [87] and the particle density in the source given by Eq. (3.2.2) is $n_0 \approx 2.5 \times 10^{19}\,\mathrm{m}^{-3}$. Taking the collisional cross-section to be $\sigma = 336 \times 10^{-20}\,\mathrm{m}^2$ [31], the mean free path of the molecules obtained with Eq. (3.2.1) is $\lambda \approx 8\,\mathrm{mm}$. There is no sharp demarcation line between the conditions of the two gas expansion regimes described above, however, in many practical cases the strict condition for the effusive regime $d \ll \lambda$ can be relaxed, and the particle behavior can be described by the effusion laws even if $d \sim \lambda$ [88]. For the present experimental setup with the source aperture $d = 1\,\mathrm{mm}$ which was used in all experiments, the mean free path $\lambda > d$ which justifies the molecular beam description in the effusion regime.

The particle density at a distance r from the molecular source can be estimated according to [88]:

$$n(r) = \frac{1}{3}\frac{A_s n_0}{\pi^{3/2} r^2}, \tag{3.2.3}$$

where A_s is the area of the source aperture, r is the distance from the source to the region of interest and n_0 is the density of molecules in front of the source aperture that can be calculated from Eq. (3.2.2). In the present experimental geometry the distance from the source to the laser–molecule interaction volume is 60 mm. Thus, at 775K evaporation temperature a particle density of $n \approx 3.4 \times 10^{14}\,\mathrm{m}^{-3}$ is derived.

The vapor pressure of fullerenes depends exponentially on the temperature [87,89,90], therefore a fluctuation of only 3 K at 775 K results in molecular density fluctuations in the interaction volume of more than 10%. It follows that stable temperature conditions are important. A power supply Veeco 1508 used for heating up the oven provides a stable temperature with uncertainty $< 1\,\mathrm{K}$. Using Eqs. (3.2.2) and (3.2.3) with pressure data from [87] one can calculate that this results in density fluctuations of less than 3%.

Another aspect to be considered in molecular beam experiments is the velocity distribution of particles. In photoionization studies molecular and laser beams usually intersect perpendicularly. Thus, the molecular velocity with respect to the transverse intensity $I(x, y)$ profile of the laser beam and the timescale of a light–molecule interaction event

must be considered. In pulsed laser experiments the timescale of the interaction process is defined by the pulse length for single-pulse experiments and the pump-probe delay in case a sequence of pulses is used. In effusive beams the velocity distribution of molecules with mass m and temperature T can be described by the Maxwell–Boltzmann distribution [88]:

$$f(v) = 4\pi \sqrt{\left(\frac{m}{2\pi k T}\right)^3} v^2 \mathrm{e}^{-\frac{mv^2}{2kT}}, \tag{3.2.4}$$

with an average velocity:

$$\langle v \rangle = \sqrt{\frac{8kT}{\pi m}}. \tag{3.2.5}$$

For a vapor of C_{60} molecules at 775 K the average velocity is 151 m/s. The maximum pump-probe delay used in the present work is $\sim$1000 fs. Over this time, the average C_{60} molecule in the beam travels $\sim$0.15 nm which is slightly more than 20% of its diameter. Taking into account that the diameter of the focused beam has the order of µm, the intensity $I(x, y)$ experienced by a molecule stays essentially constant throughout the interaction time and the molecules can be considered in rest.

3.3 Femtosecond UV laser system

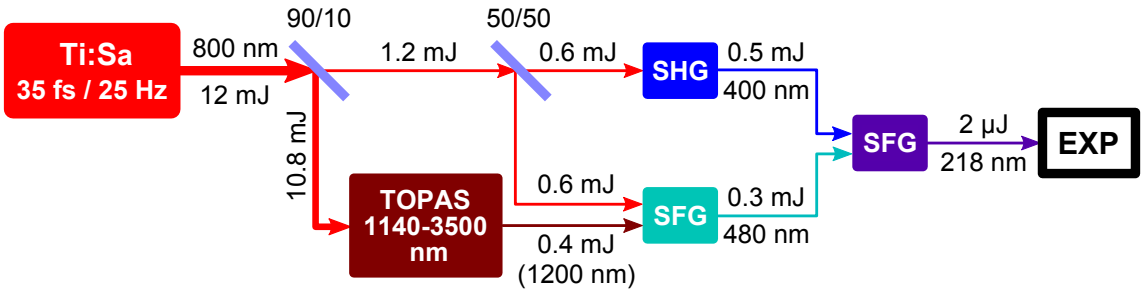

Figure 3.3.1: Schematic layout of 218 nm generation scheme.

In order to study electronic transitions into highly excited manybody states close to the ionization potential, fs pulses at ultraviolet (UV) frequencies are required [91]. The laser setup for generating fs pulses in the range of 216–222 nm comprises a Ti:Sa laser system, an optical parametric amplifier (OPA) and several frequency mixing stages. The outline of the system is sketched in Fig. 3.3.1. The Ti:Sa laser (Amplitude Technologies) is the backbone of the overall generation scheme and provides 35 fs (FWHM) pulses with a pulse energy of 12 mJ behind the compressor at a repetition rate of 25 Hz and the 800 nm central wavelength. This output is split into several arms. First, the beam is split in a 90:10 ratio. The more intense fraction is sent to a commercial OPA (Light Conversion, TOPAS-C + HE-TOPAS). The OPA is continuously tunable in the infrared spectral range (1140–3500 nm) and is pumped by the Ti:Sa laser. For the subsequent frequency conversion in the UV the output of the OPA is tuned to 1200 nm. The 11 mJ of the 800 nm pump pulse are converted to ≈ 0.4 mJ at this wavelength. The low-intensity fraction of the Ti:Sa laser (10 %) is equally split into two branches. One half is recombined with the 1200 nm output of the TOPAS in a β-barium borate (BBO, 0.2 mm thick) crystal to generate 480 nm light by sum frequency generation (SFG). The second half is frequency doubled in another BBO, and then together with the 480 nm beam directed to the third SFG stage (BBO, 40 µm thick) to finally generate the 5.7 eV (218 nm) photons. The UV pulse energy was measured using a calibrated XUV photodiode and a pyroelectric detector to be ≈ 2 µJ. The complete nonlinear optical setup was simulated using the software package LAB2 [92] including dispersion induced by UV pulse propagation in air and through the 2 mm thick entrance window of the vacuum chamber. According to the calculation the 218 nm pulse duration in the interaction region is of the order of 100 fs FWHM with a spectral bandwidth of 2.8 nm. A coarse cross-correlation measurement

performed between the 400 nm and 480 nm pulses of 150 fs FWHM supports the derived UV laser pulse parameters.

3.4 In-vacuum optics and diagnostics setup

The easiest way to realize a one-color pump-probe experiment is to produce a double pulse sequence by splitting a given initial pulse in two replicas, delay one of them in time, and then overlap both in space. With reflective optics it is usually performed with a so-called split-and-delay unit (SDU). The following sections describe the SDU developed in the framework of the present thesis (Section 3.4.1), the setup for diagnostics of the longitudinal SDU displacement on the nm scale using white light interferometry (Section 3.4.2) and the focusing optics used in experiments with UV and XUV laser beams (Section 3.4.3).

3.4.1 Reflective VUV/XUV split-and-delay unit

As was shown in Section 2.3.4, fringe-resolved interferometric autocorrelation using reflective optics requires an SDU of a special geometry. Design, characterization and commissioning of the SDU was one of the central parts of the present thesis.

3.4.1.1 Design

Two SDU units of different geometry were developed and tested during the presented work. The first SDU uses an approach similar to the one applied in [7], i.e. it consists of two identical comb-mirrors interposed such that their teeth form an alternating pattern of reflective strips. Each comb-mirror was processed from a $50 \times 30 \times 1\,\mathrm{mm}^3$ high quality silicon substrate by a diamond circular saw. The combs have 20 mm long and 100 µm wide teeth with 150 µm gaps between them. When interposed the two combs form a 25 µm spaced grid of reflective strips. The sawing technology using a circular blade limits the maximum possible thickness of the processed material to 1 mm substrate thickness, which is the limit for a 150 µm thick saw blade. This design proved to be insufficient to maintain the initial flatness after the sawing,because the sawing process induces mechanical stress on the relatively long and narrow strips that have only a single attachment point to the bulk of the substrate. As a result the individual teeth of each comb acquire a twist which proved to be devastating for the experiment requiring the perfect overlap of the beams reflected from the two integral parts of the SDU. To satisfy the high requirements for surface quality of the order of $\lambda/8$ at 38 nm the second SDU of a different design was tested. It consists of two reflectors of complementary but distinctly different design. The

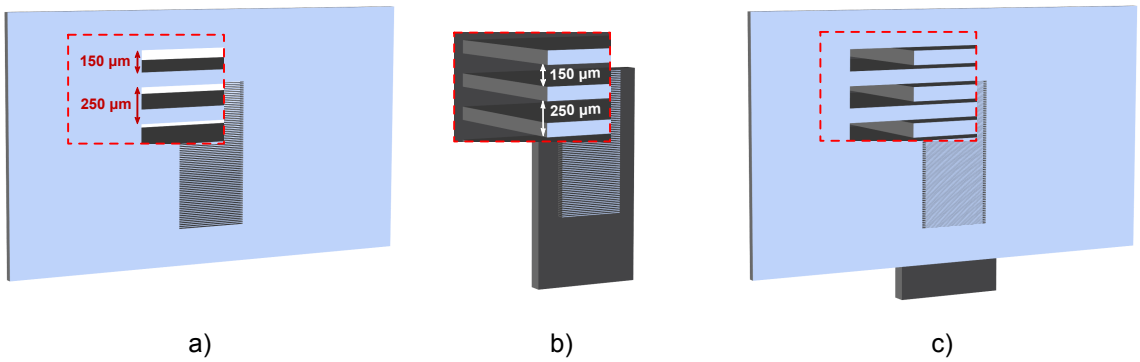

Figure 3.4.1: Sketch illustrating the two components of the SDU. (a) Is the slotted and (b) is the ridged grating. (c) Shows their interleaved arrangement after assembling. Reflective faces are shown in pale blue.

basis of the reflectors are high quality polished silicon wafers (Pilz Optics). The final manufacturing of a desired shape was performed by experimental collaborators. The design of the two mirrors is illustrated in Fig. 3.4.1. The first mirror (Fig. 3.4.1a) is a $60 \times 35 \times 1\,\mathrm{mm}^3$ rectangular wafer with the central $10 \times 20\,\mathrm{mm}^2$ area processed with a diamond circular saw to produce a slotted grid. The grid has a period of 250 µm, with 150 µm wide, 10 mm long slits and 100 µm wide stripes of material between them. In contrast to the comb design, the grid mirror has shorter stripes supported by the bulk of the substrate from both ends. This enables to keep the stripes narrow, which is essential to resolve the diffraction pattern at short wavelengths, and at the same time make them more resilient to stress and maintain the required surface quality. The counterpart of the slotted mirror is shown in Fig. 3.4.1b. Its reflective face is processed as a pattern of 100 µm wide and 150 µm spaced ridges covering the area of $8 \times 20\,\mathrm{mm}^2$ and protruding from the substrate for 1.25 mm. The dimensions of the ridges are designed to fit into the slits of the grid mirror. When interposed the two mirrors form a sequence of 100 µm wide and 25 µm spaced stripes (fill factor 0.8) with neighboring elements belonging to different mirrors. The pump-probe delay is generated by displacing one of the mirrors along the surface normal.

The surface quality of the two mirrors was checked with a home-built white light interferometer (WLI) (details are given in Section. 3.4.2). A fragment of the heightmap of the assembled SDU covering a $3.6 \times 1.8\,\mathrm{mm}^2$ area is shown in Fig. 3.4.2. The "ridged" mirror (even stripes in numerical order from top in the figure) proved to maintain the high quality of the original substrate even after the sawing procedure. Its heightmap has smooth fluctuations with a standard deviation of 4 nm. The mirrors are glued to a mount

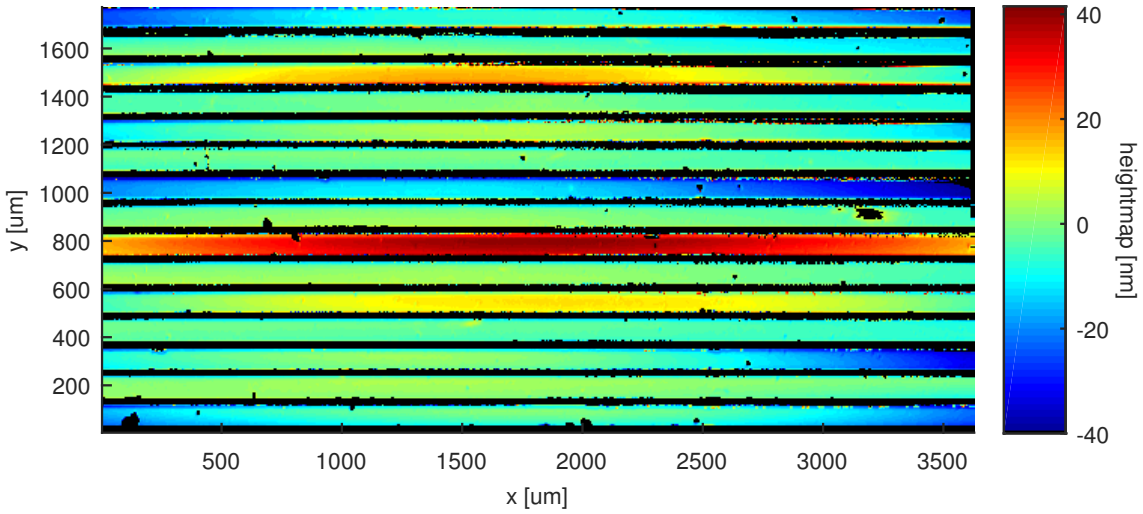

Figure 3.4.2: Heightmap of the SDU fragment. Both gratings are present, odd stripes counted from top belong to the slotted grating, even stripes—to the ridged grating. Dark spots seen on the surface of the mirrors are dust particles gathered on the optics.

and this low frequency variance is most probably a result of a strain induced by the glue and not a characteristic of the substrate. The "slotted" mirror (odd stripes from top in the figure) is less robust and its height variance can reach more than 100 nm depending on the area of the mirror. Thus, special care must be taken to hit a "flat spot" with the laser beam during the experiment.

3.4.1.2 Optical performance

The effect of the SDU surface profile on the optical performance was simulated applying wave optics (Appendix A) and is summarized in the following. Let the transverse complex electric field of the incident beam be $\tilde{u}_i(x, y)$. Upon reflection from a rough surface the incident wavefront will experience a phase distortion depending on the surface heightmap $h(x', y')$ and the angle of incidence θ_i (Fig. 3.4.3). For a monochromatic beam with a wavenumber $k = 2\pi/\lambda$ the phase distortion is given by [93,94]:

$$\varphi(x', y') = 2k\, h(x', y')\, \sin\theta_i. \tag{3.4.1}$$

The coordinates in the surface plane x', y' and in the plane of the incident wavefront x, y are related by simple transformations:

$$\begin{aligned} x &= x' \sin\theta_i, \\ y &= y'. \end{aligned} \tag{3.4.2}$$

If the incident wavefront $\tilde{u}_i(x, y)$ is known, then the reflected wavefront can be expressed

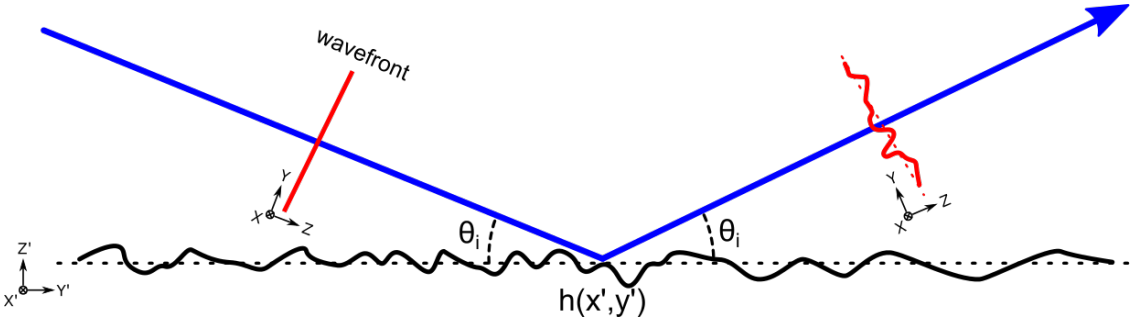

Figure 3.4.3: Wavefront distortion after a reflection from a rough surface with a profile $h(x', y')$.

by:

$$\tilde{u}_r(x, y) = \tilde{u}_i(x, y)\mathrm{e}^{\mathrm{i}\varphi(x,y)}, \tag{3.4.3}$$

and then propagated in free space as explained in Appendix A.

The effect of the SDU surface heightmap on the beam quality was simulated propagating the beam through the major optical elements of the system (the SDU and the focusing mirror) to the focal plane where the interaction with the molecular beam occurs. In the simulation a Gaussian beam with a waist $w = 0.5\,\mathrm{mm}$ and a wavelength $\lambda = 38\,\mathrm{nm}$ is incident on the SDU at an angle $\theta_i = 22\,^\circ$. After reflection the beam is propagated to the spherical focusing mirror with a focal length $f = 300\,\mathrm{mm}$ at normal incidence. Finally, the beam is reflected to the focal plane placed 300 mm from the focusing mirror. The simulation result is shown in Fig. 3.4.4. As can be seen from comparison of the realistic heightmap with the ideally flat surface, the surface figure of the SDU will allow to see interference contrast in the focus for 38 nm wavelength and 22 ° angle of incidence, though it will be reduced.

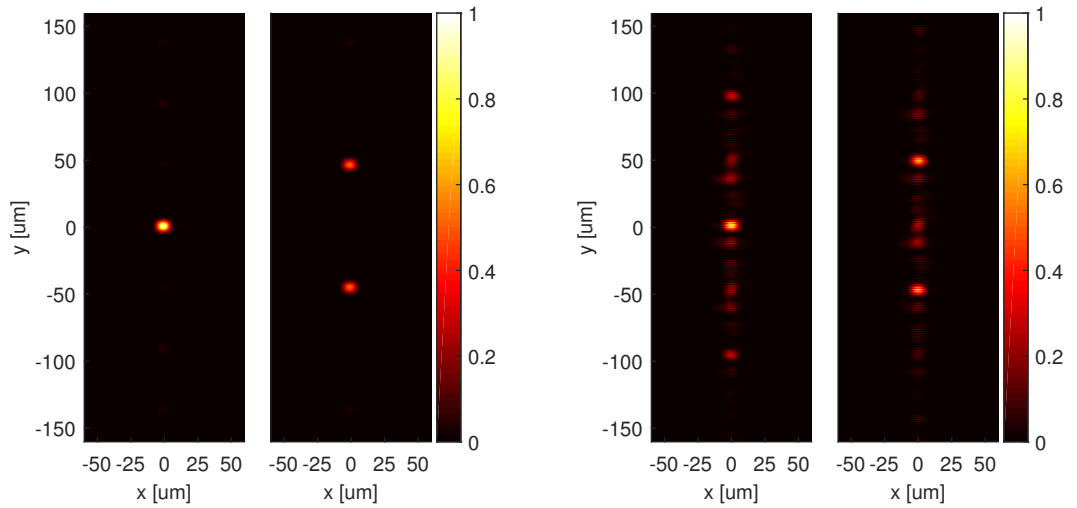

(a) zero delay (b) π delay (c) zero delay (d) π delay

Figure 3.4.4: Simulation of intensity distribution of a Gaussian beam ($w = 0.5\,\text{mm}$, $\lambda = 40$ nm) in the focal plane ($f = 300\,\text{mm}$) after reflection from the SDU with a geometry described in Section 3.4.1.1. (a) and (b) is an ideally flat SDU, (c) and (d) is the SDU with the heightmap shown in Fig. 3.4.2.

3.4.1.3 High-precision in-vacuum positioning system

The slotted mirror (Fig. 3.4.1a) is rigidly fixed to a special mount while its counterpart (Fig. 3.4.1b) is given several degrees of freedom driven by piezo actuators necessary for the alignment and controlling the pump-probe delay. A time delay τ between the two pulse replicas is generated by a relative displacement of the mirrors Δz along their normal and can be written as:

$$\tau = \frac{2\Delta z \sin\alpha}{c}, \tag{3.4.4}$$

where c is the speed of light and α is the grazing angle of incidence (AOI) of the laser beam. Fringe-resolved autocorrelation at short wavelength requires a control of pump-probe delays on a sub-fs scale which can only be provided by a high-precision piezo actuator. Due to resolution limitations of controlling electronics, the precision of piezo stages is inversely proportional to their maximum travel range which makes it hard to satisfy the demands for both high precision and long delay generation simultaneously. In order to achieve sub-fs resolution precision was the top priority requirement still allowing moderate delays of several hundred fs. Since an autocorrelation function is symmetric around $\tau = 0$ by definition, all the information is contained in a single half of the trace

(positive or negative delays). This allows to mount the translation stage controlling Δz "asymmetrically", i.e. in a way that $\tau = 0$ corresponds not to the middle position of the stage, but closer to one of its travel limits. This way of mounting gives an advantage of generating longer pump-probe delays compared to the middle position without loss of information. The actuator used in the present setup is a linear piezo stage (PI 622.1, Physik Instrumente) with a travel range of 250 µm in the closed loop (CL) and 300 µm in the open loop (OL) modes accordingly. For angle of incidence (AOI) $\alpha = 22\,^\circ$ from surface these values translate in delay intervals of 624 fs in CL mode and 748 fs in OL mode. The nominal resolution of the stage is 0.7 nm in CL mode which in theory enables to control delays with a precision down to ~ 0.002 fs.

Parallelism of the two SDU reflectors is required to overlap the pulses in space and is ensured by controlling pitch and yaw angles of the movable mirror. Each of the rotations is motorized by a piezo stage with a 80 µm travel range (PX100 SG VAC, Piezosystem Jena). These rotations are used for a precise alignment of the mirrors after the mounting and for fine corrections during the experiment. Each rotation axis has a different lever providing the adjustment range of ± 2.76 mrad for the pitch and ± 0.50 mrad for the yaw angle.

3.4.2 White light interferometry

The control of temporal delays between subsequent pump and probe pulses with sub-femtosecond precision requires control of the SDU mechanics on a nanometer scale and an adequate feedback providing information about the SDU reflective profile in each moment of time. White light interferometry (WLI) was chosen to fulfill this task. WLI is widely used for profile characterization of both static and dynamics surfaces [95] with sub-nanometer precision. As any interferometry technique, WLI utilizes the superposition property of electromagnetic waves, i.e. their ability to interfere when superimposed. There are various designs of WLI systems and the choice in each particular case depends on specific requirements of the application. The main components of any white light interferometer are: a broadband light source, a beam splitter, two reflecting surfaces and a detector. In its operation principle a white light interferometer is essentially a field autocorrelator (FAC) described in Section 2.3.1. A collimated beam from the light source is split and guided into two interferometer arms towards reflective surfaces. After reflection the two beams are collinearly recombined and directed to a position sensitive detector

(usually a camera). The key difference between an FAC and a WLI is given by the different tasks of these systems and lies in the light source and reflective surfaces used in each case. While an FAC employs optically flat mirrors to characterize the spectrum of the light source, a WLI utilizes a broad band (white) light source, usually with a known spectrum, to characterize a sample surface placed in one of the interferometer arms.

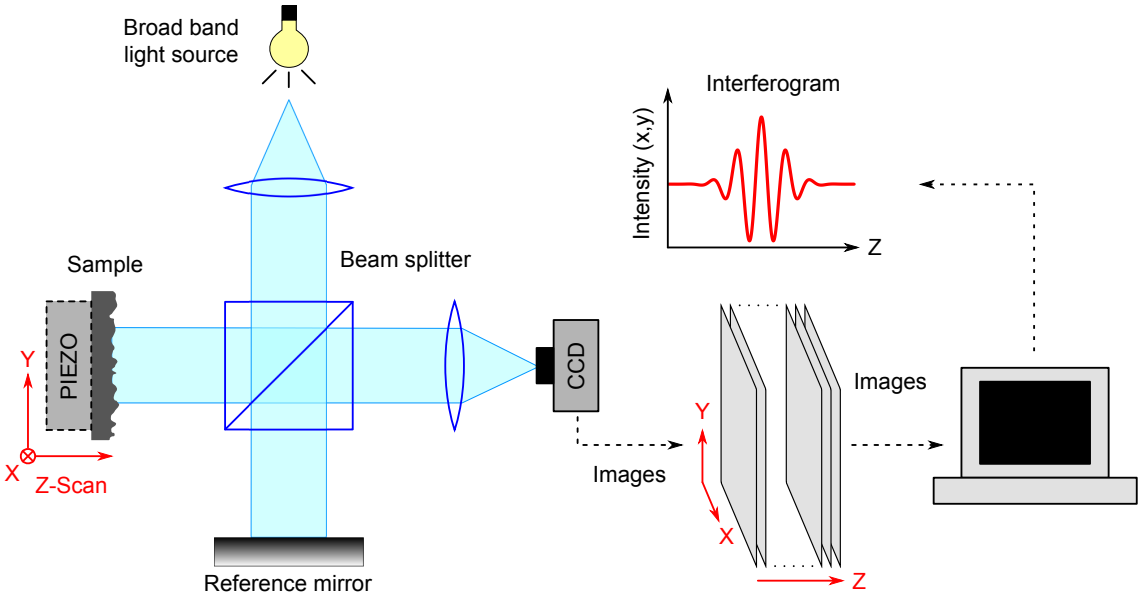

Figure 3.4.5: Schematic layout of a Michelson white light interferometer.

A schematic outline of a Michelson-type WLI setup is shown in Fig. 3.4.5. The signal $S_{\mathrm{WLI}}(x, y, \Delta)$ recorder by the camera at a position with transverse coordinates x and y depends on the optical path difference (OPD) denoted as $\Delta = \Delta(x, y)$ between the two interferometer arms. As with the FAC, the signal is a sum of the interferometric term and the background [96]:

$$S_{\mathrm{WLI}}(x, y, \Delta) = I_1(x, y) + I_2(x, y) + 2\sqrt{I_1(x, y) I_2(x, y)}\, \gamma(\Delta) \tag{3.4.5}$$

where $I_1(x, y)$ and $I_2(x, y)$ are reflected intensities of the two beams and $\gamma(\Delta)$ is the interferogram. In general, γ is a function depending on the spectrum of the light source and the dispersion in the optical elements of the interferometer. In the so-called balanced interferometer the dispersion in both arms is equal and γ is a symmetric function. In many practical cases γ can be approximated by the autocorrelation function of the light source (which is the Fourier transform of source's power spectrum) oscillating with the source's mean frequency. A typical Δ-dependence of $S_{\mathrm{WLI}}(x, y, \Delta)$ for fixed x and y is

shown in Fig. 3.4.6b and similar in appearance to $S_{\mathrm{FAC}}(\tau)$ from Eq. (2.3.5). The intensity

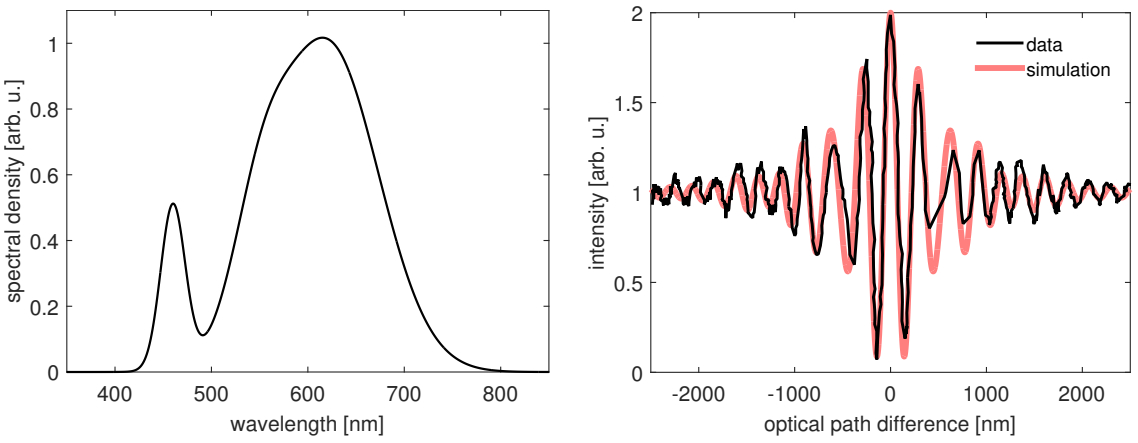

(a) (b)

Figure 3.4.6: Spectrum (a) and experimental autocorrelation trace (b) of the white light diode used in our home-built WLI setup. The interferogram simulation was performed using the spectrum (a) taken from [97].

distribution has its maximum at $\Delta = 0$ which corresponds to equal optical path length along both interferometer arms and hence full constructive interference of the beams. If one of the reflective surfaces has a known profile (called reference), and another one has an unknown heightmap $h(x, y)$, then $S_{\mathrm{WLI}}(x, y, \Delta)$ can be expressed as a function of $h(x, y)$. Characterization of $h(x, y)$ is a common application of a WLI. The reference is typically chosen to be optically flat and the OPD between the beams can then be written as:

$$\Delta(x, y; z) = 2(z - h(x, y)), \tag{3.4.6}$$

where z is a fixed coordinate of the sample surface along the beam propagation controlled by the experimentalist. In case the reflectances of both, the reference and the sample, are comparable and do not vary significantly across the surface, the incoherent sum $I_1(x, y) + I_2(x, y)$ that defines the background intensity can be replaced by a constant value I_0 and Eq. (3.4.5) becomes:

$$S_{\mathrm{WLI}}(x, y, z) = I_0 + I_0 \Gamma(z - h(x, y)) \cos\left(4\pi \frac{z - h(x, y)}{\lambda_0}\right), \tag{3.4.7}$$

with $\gamma(\Delta)$ expressed as a product of the envelope (autocorrelation function) $\Gamma(\Delta)$ and

a cosine term oscillating with the frequency corresponding to the mean wavelength of the light source λ_0. Performing a z-scan and capturing images at different z-values one obtains $S_{\mathrm{WLI}}(z)$ for each camera pixel. Subsequent analysis, i.e. finding a z-value for the signal maximum for every pixel, enables the reconstruction of the complete sample's heightmap $h(x, y)$. Since a signal recorded by a pixel is intensity integrated over the sample area imaged by the pixel, the resolution of the obtained heightmap is defined by the resolution of the imaging system, i.e. camera and optics. The heightmap $h(x, y)$ can be reconstructed correctly only if the sample's surface is smooth on the scale of lateral resolution of the imaging setup.

3.4.2.1 Design

In the present work the WLI setup was used to monitor the displacement and angular deviations of the SDU in real time during experiments with frequencies up to 10 Hz. Outline of the setup is shown in Fig. 3.4.7. The Michelson interferometer is arranged vertically with all the components except the camera and the light source located in vacuum. A 1 W white LED (Ledxon ALUSTAR) is used for illumination. The spectrum of the diode and its autocorrelation signal are shown in Fig. 3.4.6. The LED with collimating optics is mounted on top of the optics chamber and the white light beam passes inside the chamber through a window flange. A 20 mm broadband cube (Edmund Optics) is used for splitting and recombining the beams. The cube is fixed on a kinematic mount (Newport 9873-M-K) which provides angle adjustment together with a 2 mm translation along the horizontal arm of the interferometer which has the SDU at the end. An uncoated polished silicon $25 \times 25 \times 6\,\mathrm{mm}^3$ wafer (Pilz Optics) is used as a reference surface and is placed in the vertical arm. For scanning along z-direction the reference mirror is motorized with a translation piezo stage (PX100 SG VAC, Piezosystem Jena). Due to the chamber geometry two additional mirrors are required to steer the recombined beam towards the camera mounted on the air side.

The majority of commercial WLI setups are essentially microscopes with narrow fields of view and high magnification factors to provide sufficient lateral resolution for investigation of rough surfaces. The task of our in-vacuum WLI is to characterize the relative movement of the two parts of the SDU in order to assure their parallelism and obtain a feedback about the displacement. This requires imaging of a large sample area at every camera shot and hence demands a relatively large field of view. On the other hand, the silicon wafers proved to be essentially flat on a microscale (Fig. 3.4.2), and given that

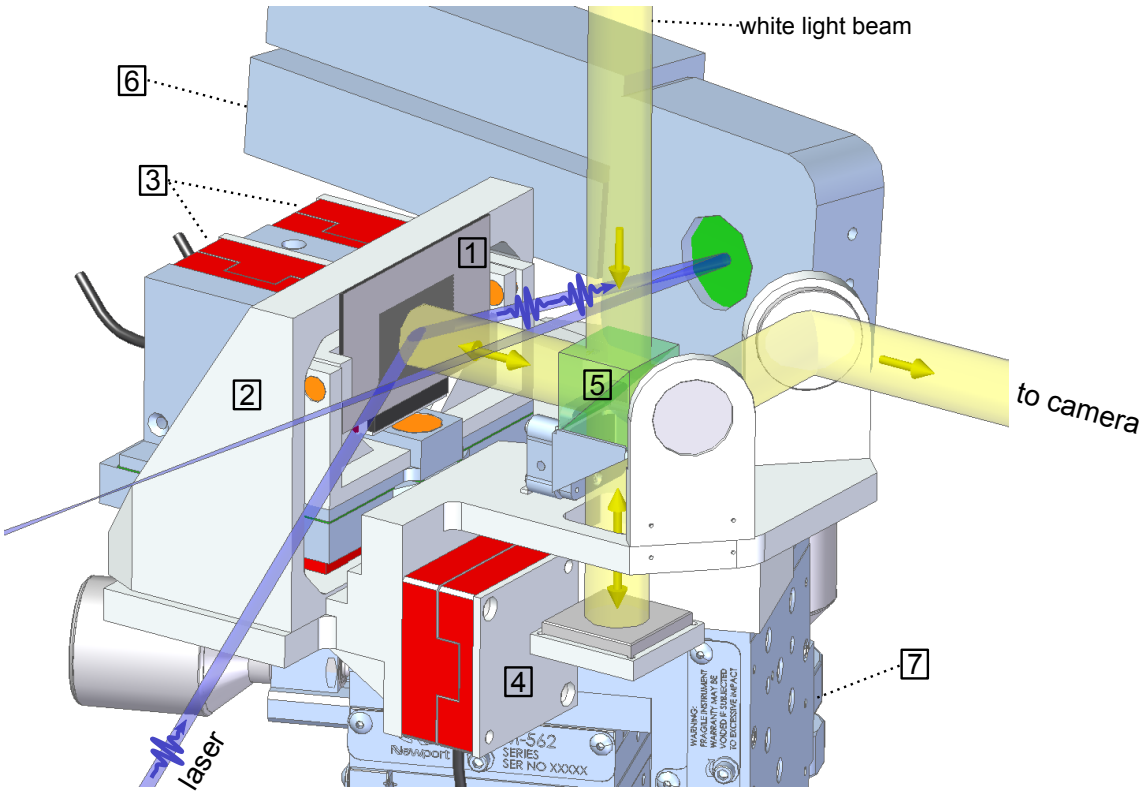

Figure 3.4.7: Technical drawing showing the main components of the in-vacuum optics with supports and motorized manipulators: 1—SDU reflectors, 2—mount frame of the SDU, 3—piezo stages used the for angle alignment of the SDU reflectors, 4—reference mirror of the WLI setup mounted on the scanning stage, 5—WLI beam splitter, 6—motorized mirror mount with the focusing mirror for the laser beam, 7—XYZ manipulator for translational alignment of the complete system with respect to the laser beam.

the stripes of the SDU have a width of 100 µm, high lateral resolution is not necessary. For that reason no magnifying optics besides a common camera objective was used. A combination of a Thorlabs DCC3240C camera and an objective with a 180 mm focal length provided a field of view sufficient to image a $15 \times 15\,\mathrm{mm}^2$ area with a transverse resolution of $\sim 10\,\mu\mathrm{m}$ which proved to be acceptable for the task.

3.4.2.2 Single-shot delay diagnostics

Vibrations coming from typical sources that are present in the lab environment, like scroll pumps or ventilation system[1], have strong impact on the performance of the sensitive

[1]The turbo pump (Pfeiffer HiPace 700M) attached to the chamber itself had a negligible effect on the performance due to the magnetic bearing which strongly reduces the vibrations.

split-and-delay unit. However, the important quantity is not the vibration of the setup as a whole but the relative jitter of the two SDU components that define the pump-probe delay. It was found that the feedback loop of the z-scan piezo is not fast enough to correct for the external vibrations and this causes the corresponding reflector to oscillate around the set position thus leading to delay fluctuations.

The frequency spectrum of the vibrations shown in Fig. 3.4.8 was obtained by recording a movie of jittering interference fringes with the WLI camera and then taking the Fourier transform of the time-dependent position of a single fringe. The analysis shows that main contributions come from frequencies < 100 Hz. Typical jitter amplitudes vary from several tens to more than 100 nm. A displacement of 100 nm at 22 ° grazing AOI corresponds to a delay $\tau = 0.25$ fs which is a rather large value for VUV/XUV wavelengths. For example, for 38 nm radiation that has an oscillation period of 0.127 fs, the jitter constitutes already two optical cycles. Therefore, the fringe-resolved autocorrelation becomes impossible if the signal is accumulated. To obtain the fringe resolved trace the exact knowledge of the SDU displacement on the shot-to-shot basis is required. In gen-

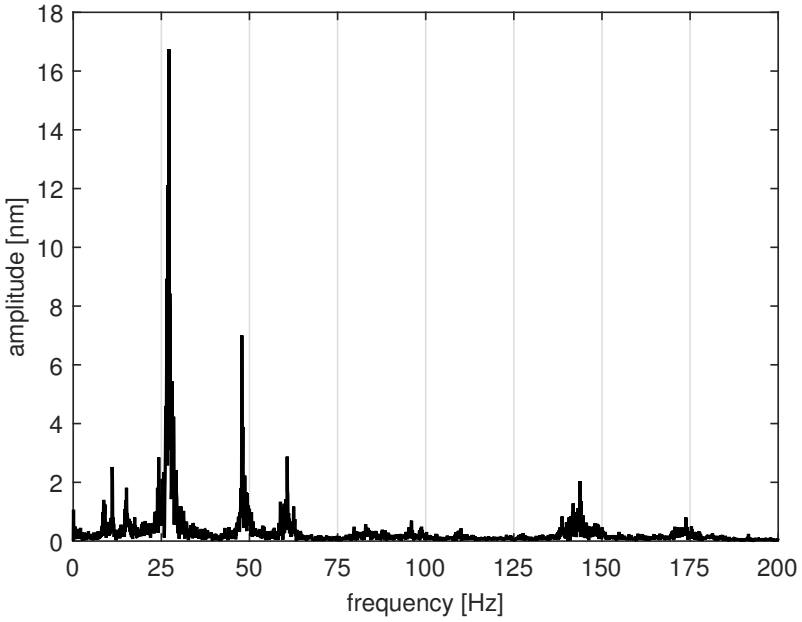

Figure 3.4.8: Frequency spectrum of the relative displacement jitter of the two SDU gratings.

eral, the exact determination of the heightmap requires to perform a z-scan with a WLI which is not a problem if both of the surfaces of the setup are static. If the OPD between the surfaces varies with time faster than a typical scan period (as in the case described above), then scanning is not applicable and a single-frame technique is required. The

single-shot determination of the SDU profile is described as follows. The position of the maximum interference fringe that reflects the OPD $\Delta(x, y; z)$, is a function of both, the local variation of the heightmap $h(x, y)$ and the shift of the heightmap along z-direction as a whole (recall Eq. (3.4.6)). As a result of the jitter, z, assumed to have a well defined value before, becomes a time-dependent quantity $z = z(t)$ oscillating around some reference value z_0 at several tens of Hz with sub-100 nm amplitude. The oscillation period is, however, much larger than the propagation time of a single pulse (or a pump-probe sequence) and $z(t)$ can be considered constant within the timeframe of a single light–sample interaction event. Hence, recording a short-exposure WLI image synchronized to the laser pulse arrival gives a snapshot of the interference pattern corresponding to a certain z and pump-probe delay τ. A typical single-shot WLI image with an interference pattern on the SDU surface is shown in Fig. 3.4.9. The jitter of $z(t)$ does not change the character of $h(x, y)$ but only shifts it along the white light beam and if $h(x, y)$ is known, the relative value $z(t)$ for every laser shot can be derived evaluating the shot-to-shot displacement of the fringe pattern across the SDU surface.

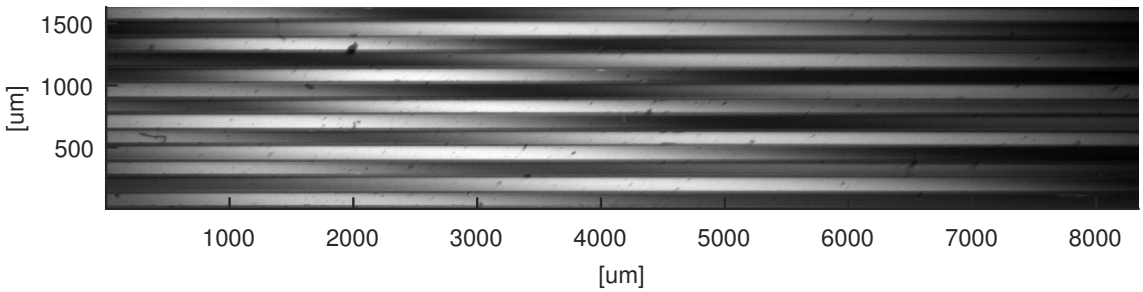

Figure 3.4.9: Typical single-shot image from the WLI camera showing the SDU surface with horizontal gratings illuminated by the white light diode. The alternating bright and dark areas correspond to interference fringes of the white light. The diagonal tilt of the fringes arises from the small angle between the overlapped beams reflected from the reference mirror and the SDU. The positions of bright areas on the first grating (odd stripes counted from top) correspond to dark areas on the second gratings (even stripes). This indicates that the longitudinal displacement between the gratings $\Delta_z = \lambda_{\mathrm{WLI}}/4$, which equals to the optical path difference $\Delta_{\mathrm{OPD}} = \lambda_{\mathrm{WLI}}/2 \approx 290\,\mathrm{nm}$.

3.4.3 Focusing optics

The setup used in the thesis is designed to employ one inch round mirrors (spherical or toroidal) for focusing the laser beams after reflection from the SDU. The geometry of the chamber enables to vary the focusing mirror–interaction volume distance in a range 316–370 mm to account for different beam divergences. At the nominal distance of 317 mm,

which corresponds to the optimal focusing of a perfectly collimated incoming beam, the laser beam has a normal AOI of 14.25 ° on the focusing optics. Experiments performed during the work on the thesis used 218 and 38 nm laser radiation and required two different mirrors.

A spherical multilayer mirror (Layertec) with $f = 300$ mm was used for focusing the 218 nm radiation. The mirror has a reflectance of 80–90% in the range of 200–245 nm. Though the AOI of 14.25 ° on a spherical mirror results in an astigmatic focus, the obtained intensity was sufficient for the experiments.

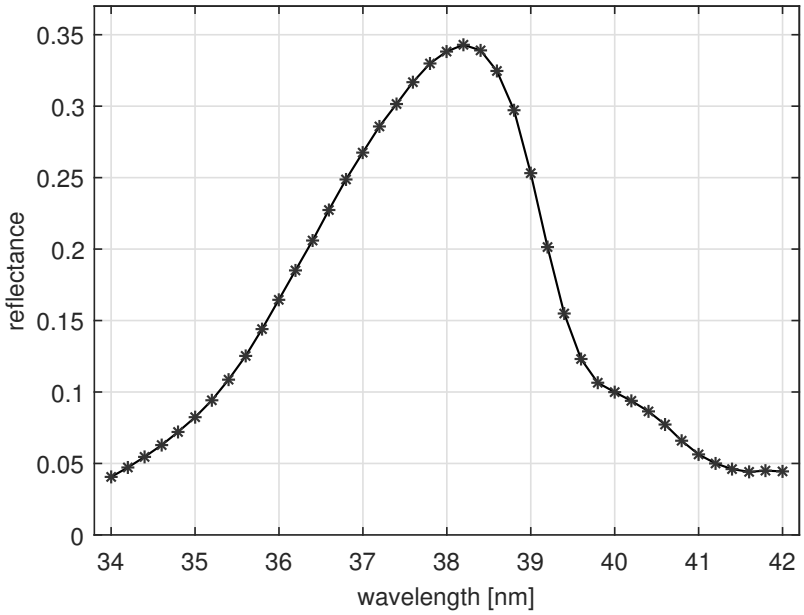

Figure 3.4.10: Reflectance curve of the toroidal mirror for 38 nm radiation at 14.25 °normal angle of incidence measured by PTB, Berlin.

The diffraction pattern generated by the SDU has the order separation proportional to the light wavelength. This means that a tighter focusing in the XUV range is required in order to resolve the spatial interference fringes. For this reason a toroidal mirror (OptixFab) was designed for 38 nm radiation. The toroid has radii of curvature $R_1 = -654.5$ and $R_2 = -614.8$ mm and a nominal focal length $f = 317$ mm at normal AOI $= 14.25\,°$. The reflectance curve of the multilayer coating is shown in Fig. 3.4.10. It has the peak reflectance of 34% at the central wavelength of 38 nm and a FWHM ≈ 3.2 nm.

The focusing optics is mounted in a motorized gimbal mount (Standa 8MGM25T-1) which gives adjustment of the beam pointing in two axes in a range $\pm 2.5\,°$. The motors

are controlled with OWIS PS90 stepper motor controller.

3.5 Charged particle spectrometer

Electron and ion spectroscopy in the gas phase are widely used to study structure and light-induced dynamics of free molecules and clusters. These techniques typically involve two steps: photoionization of a sample and subsequent analysis of the ionization products by a detector. Detection techniques available today can provide information about mass, charge, energy, momentum and spatial distribution of charged products upon ionization, which in turn can give insight into electronic structure and dynamics of the sample. Experiments rely on temporal or spatial information obtained upon particle detection, i.e. they utilize time-of-flight (TOF) or imaging data or a combination of both.

The apparatus developed during the present work is designed as a versatile setup for coincidence detection of electrons and ions utilizing the velocity map imaging (VMI) technique for electron detection and spatial or velocity map imaging for ion detection. This section is structured as follows. Sections 3.5.1 and 3.5.3 give a brief outline of the main aspects of velocity and spatial imaging in gas phase photoionization experiments. Section 3.5.3 discusses the electrostatic optics design and in Section 3.5.4 a brief description of the position-sensitive detector used throughout the experiments is presented.

3.5.1 Velocity map imaging of electrons

A photoionization event produces a cloud of electrons[1] that expands freely in space according to their nascent velocities. At a fixed moment of time t after the ionization, particles born in the same point in space with equal speed v but different velocity vectors will cover a surface of a sphere with the radius $r = vt$. In velocity space this sphere is called *Newton* sphere [98]. The Newton's sphere radius and surface density (number of particles ejected in each direction) reflects the velocity distribution, which, together with the particles' masses, carries information about energy and momentum release of the photoionization event. Imaging techniques are based on projecting Newton spheres with electric fields on a 2D position-sensitive detector (PSD). A sketch displaying a Newton sphere with its projection is shown in Fig. 3.5.1. In the idealized scenario obtaining a snapshot of the sphere at a time t will require freezing the particles at that moment and then imaging them with an instantaneous electric field. However, using classical equations of motion, it can be shown that if the energy acquired by the particles in the projecting field is much

[1] The basic principles are identical for electrons and ions. Thus, in the following we refer to charged particle in general.

higher than their initial kinetic energy, then imaging the sphere by a constantly active DC field (which is easily realized experimentally and is the basis of the majority of imaging methods) is almost equivalent to the imaging in the idealized example described above [99]. Though projecting a 3D distribution on a 2D plane leads to inevitable loss of infor-

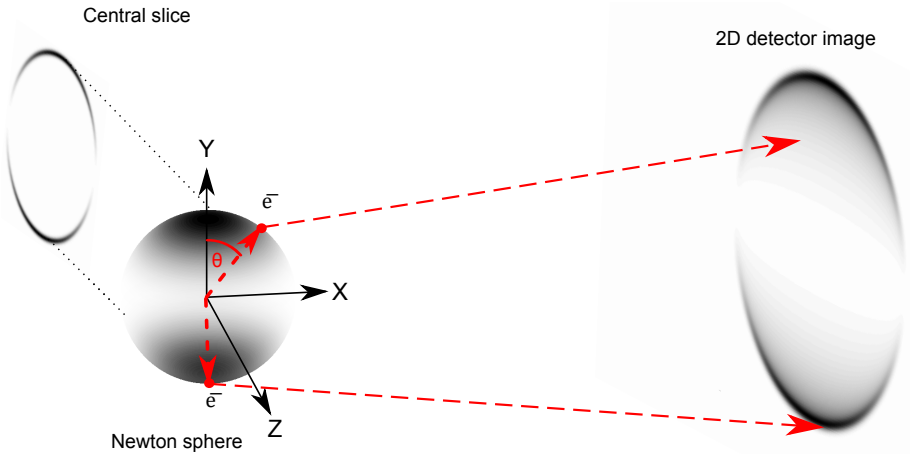

Figure 3.5.1: Illustration of a Newton sphere formed by electrons after the ionization event. The dark shade reflects the density of ejected electrons. The shown velocity distribution has a dependence $\propto \cos^2\theta$ often encountered in photoionization by light linearly polarized along the Y-axis.

mation due to folding of the dimension along the projection axis, the original picture can be reconstructed from its image under certain conditions. If the nascent velocity distribution has an axis of symmetry parallel to the detector plane the full 3D picture can be retrieved from the 2D image using the Abel transformation [100]. The axial symmetry is often encountered in experiments involving ionization of gas-phase samples with linearly polarized light. The most popular numerical reconstruction algorithms include the so-called "onion peeling" [101] and basis set expansion methods [102,103].

After the first experiment performed in 1987 by Chandler and coworkers [104] a number of steps were made to improve the imaging methods. One of the issues encountered in the early experiments using homogeneous extraction fields was the initial spatial spread of the ionization products. The ionization volume has a spatial distribution with each point carrying its own Newton sphere. The superposition of all of them on the detector causes a significant image blurring unless the source' spatial extension is compensated for. A solution was found by Eppink and Parker in 1997. They showed that with the application of an inhomogeneous projection field acting like an electrostatic lens, electrons with equal velocities can be focused on the same spot on the detector regardless of their initial spatial position [105]. The technique thus was named "Velocity Map Imaging"

(VMI). The spatial focusing achieved in a VMI spectrometer (VMIS) significantly improves the energy resolution down to a typical number of $\Delta E/E = 2{-}5\,\%$.

3.5.2 Spatial imaging of ions

Spatially resolved imaging of the ionization volume is required in some experiments, e.g. studies of spatial properties of focused laser beams or intensity-dependent ionization processes [106]. The ionization volume is defined as the intersection volume of the laser beam and the sample. A typical laser focus has a micrometer scale which is of the same order as the spatial resolution of a typical position-sensitive detector. Therefore, to resolve its possible fine structure due to, e.g. aberrations or diffraction, the image must be magnified which can be achieved with an ion microscope. In the present work the spatial imaging of the ionization region is relevant in the context of the fringe-resolved interferometric autocorrelation measurement which requires spatial resolution for the detected ion signal (see Section 2.3.4 for details). Note, that a laser beam with a wavelength 38 nm diffracted from the grating split-and-delay unit (Section 3.4.1) with a 250 µm period and then focused with a 300 mm focal length mirror will generate a diffraction pattern with orders separated by just 46 µm. The interferometric measurement we aim at requires the selection of the signal from an individual order, hence the image of the diffraction pattern must be magnified.

The task of a spatial imaging device is opposite to that of a VMI spectrometer discussed in the previous section: the VMIS resolves velocities of different particles focusing their spatial distribution, while the ion microscope resolves the spatial positions regardless of the initial velocities. In gas-phase ionization experiments the sample ions always possess nonzero velocities prior to their extraction by the electric field. These velocities can be a property of the neutral gas itself (thermal or molecular beam velocities), or be a result of the recoil acquired during the ionization process. In any case, these velocities define the ions' initial trajectories and the important aspect of spatial imaging is to minimize the effect of this velocity spread, i.e. to focus all ions born in the same spatial origin but with different velocities to the same spot on the detector. It requires different fields and electrostatic optics geometry than those used for VMI spectroscopy. If the velocity focusing condition is attained, the magnification of the image depends on the source–detector distance and the curvature of the ion trajectories. In principal, a VMI spectrometer of standard design [105] can be operated with voltage settings in spatial

imaging mode though the magnification factors in this case are modest compared to a dedicated microscope. This is due to the relatively straight ion fly paths. For example, the 300 mm long Eppink-Parker VMIS operated in the spatial imaging mode can achieve a magnification of 8–9. By contrast, a dedicated ion microscope can achieve magnification factors up to 100 [106] using a set of Einzel lenses to deflect the ion trajectories and get a high magnification on a reasonable flight distance. The experimental test of the spatial imaging capabilities of the setup are discussed in Section 4.2.

3.5.3 Design of electrostatic optics

The design of the electron–ion coincidence spectrometer is similar to the one used in [107]. It consists of two on-axis VMI spectrometers placed on opposite sides of the ionization region. One is used for the detection of electrons and the other one for ions. Each of the spectrometers comprises a detector, a drift tube and a set of electrodes (electrostatic optics) used for extraction and focusing of charged particles. The geometry of the setup is sketched in Fig. 3.5.2. The optics of each spectrometer has two elements: an extractor and a lens. In the double-sided design the electron extractor serves as the repeller for the ions and vice versa. The lens, not present in the original Eppink-Parker design [105], is placed here between the extractor and the drift tube in order to compensate for field distortions caused by the aperture in the repeller (see the details below).

Depending on the mode of operation, the optimal fields for extraction of electrons and ions require a different set of voltages applied to the electrostatic optics. Therefore, the coincident detection of electrons and ions for each laser shot with maximum resolution requires a fast high-voltage switch (e.g. Behlke). Before the laser pulse arrives and ionization takes place the voltages are kept at values optimal for electron detection. Light electrons reach the detector within the first 100 ns after the ionization. This period of time is too short for the much heavier ions to respond to the extraction field and they can be considered as almost motionless. After 100 ns the voltages are switched to optimal values for ion detection and maintained for a time sufficient for all ions to reach the detector (typically, several tens of μs). Finally, the voltages are switched back to the electron mode before the next laser pulse arrives.

A typical one-sided VMI spectrometer has a repeller in a form of a blind disc or with a small orifice for on-axis sample injection which has a negligible effect on the electric field. In a double-sided configuration the two electrodes close to the ionization region

must have relatively large apertures to provide a free path for charged particles towards each of the detectors. This introduces field distortions in the extraction region which reduce the image quality. Lenses can be used to compensate for these distortions. In this case the lens on the ion side is operated at negative potential during the detection of electrons, and the lens on the electron side is switched to positive voltage during the detection of ions [107].

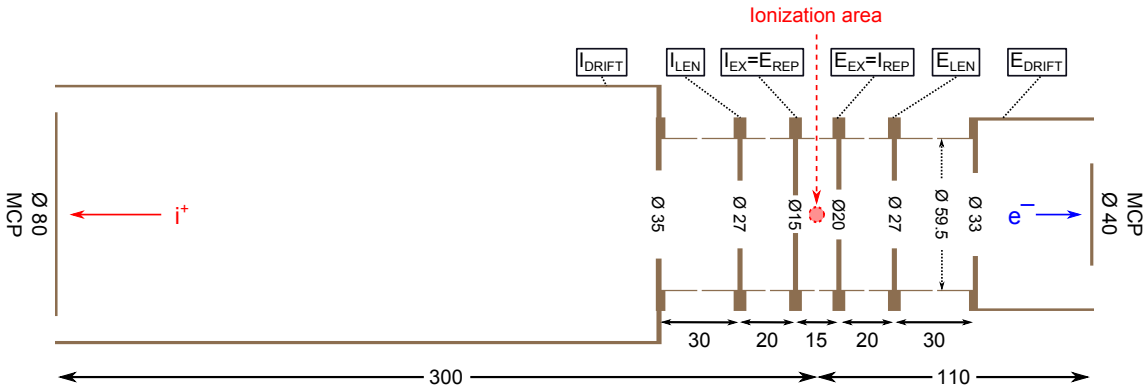

Figure 3.5.2: Outline of the double-VMI. Units are millimeters.

In the present setup the electrodes of the spectrometer are made as aluminium discs with central apertures and diameters as given in Fig. 3.5.2. Cylindrical shielding with an inner diameter 58 mm is a part of each electrode and spans most of the space between their main bodies. It serves to protect the particles' fly path from electric field distortions induced by mounting rods. A mu-metal drift tube covers the area between the last electrode and the detector of each spectrometer.

The spectrometer design bases on detailed simulations of its performance using the SIMION 8.0 [108] software package. Performance of a spectrometer to a large extent is defined by its geometry, which, in turn, is usually dictated by the geometry of other parts of the experimental setup (e.g. the vacuum chamber). Once the geometry is fixed, the optimal electric potentials can be found from simulations. Traditionally, the velocity imaging condition for a VMI spectrometer is specified as a voltage ratio between the repeller and the extractor electrodes. If the system contains additional electrodes, their voltage ratio also has to be defined. As was mentioned before, for electron detection the lens on the ion side is used to improve the focusing and is operated at higher negative voltage than the repeller. The lens on the electron side is set to the same potential as the drift tube, i.e ground in the present case. The voltage ratios optimal for VMI were determined using a build-in SIMION optimization routine which is described in the fol-

lowing. Electrons with different velocities are launched from a finite spatial volume. The source volume has a shape of a cube with 1 mm side and electrons originate from its center, corners and centers of its faces and edges. The voltages are adjusted with a simplex algorithm [108] to get the smallest spread of the radial coordinate in the detector plane for every velocity component, i.e. minimize the blurring due to finite spatial size of the source. By analogy with optics, the electrostatic lens system suffers from different aberrations. The most notable of them are "chromatic"—dependence of the focal length on the particle's speed, and "spherical"—dependence of the focal length on the angle α between the velocity vector and the flight axis. To account for aberrations the optimization run was carried out for several groups of electrons, each group with a different energy and α. The voltages were then optimized to obtain the smallest radial spread averaged over all groups with different angles and energies. The optimal focusing ratios found from simulations were $V_{\text{rep}} : V_{\text{ex}} : V_{\text{len(i)}} = 1 : 0.76 : 1.52$.

As was discussed in Section 3.5.1 the VMI technique is based on projecting a 3D Newton sphere on a 2D detector, in other words "mapping" the particle's velocity component parallel to the detector plane (i.e. $\mathbf{v}_{yz}$ in the coordinate system shown in Fig. 3.5.1). Thus, for a given particle's speed the outermost radius of the projection will be spanned by particles with the initial velocity vector orthogonal to the flight axis. Provided that the focusing voltage ratio is determined and maintained fixed, the maximal detectable kinetic energy can be expressed as a function of the potential of one of the electrodes (e.g. repeller). Since the focusing is optimized for different emission angles the variation of energy resolution with α is weak, and hence the resolution will be quoted only for electrons with a velocity vector transverse to the flight axis. A relation of the electron's initial kinetic energy E in eV and its radial position R in mm on the detector can be approximated by the following expression [109]:

$$E = qV_{\text{rep}}\frac{R^2}{C^2}, \tag{3.5.1}$$

where q is the charge in e, V_{rep} is the repeller potential[1] in V and C is a coefficient depending on the spectrometer geometry which can be found from simulations. The obtained value of C for the present setup is 221.3 mm. Once this coefficient is known, the energy resolution $\Delta E/E$ for a given electron kinetic energy can be calculated. For this

[1] Here it is assumed to be negative, for a positive potential the formula has to be modified to maintain the correct signs for variables.

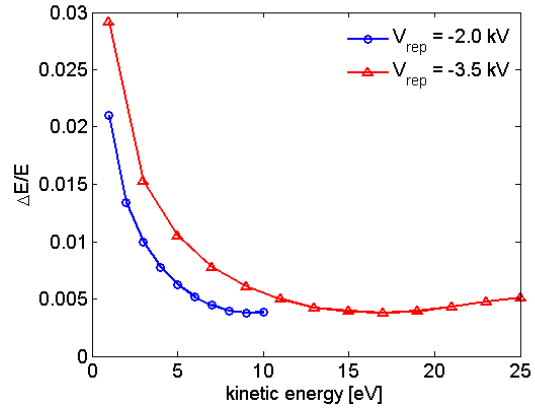

Figure 3.5.3: The energy resolution of the VMI for two repeller potentials.

several electron groups (10000 electrons per group), each with a different kinetic energy and randomly sampled within a 4×1 mm^2 cylindrical source volume were launched. The electrons' velocity vector was oriented parallel to the detector plane and perpendicular to the source's long axis. $\Delta E/E$ for a given energy can be estimated by calculating the FWHM of the radial position spread ΔR and then converting it to energy using Eq. (3.5.1). The resolution curves obtained for different repeller voltages are shown in Fig. 3.5.3.

It is worth noting that the figure mentioned above illustrates only the theoretical resolution given by the electrostatic optics considering that the manufacturing and construction of the setup is perfect and the resolution of the detector itself is infinite.

3.5.4 Position-sensitive detector

The present detection system consists of a phosphor-based position-sensitive detector (PSD) and a camera, which is a typical choice for imaging applications. The PSD contains a microchannel plate (MCP) chevron stack [110] followed by a thin metal anode and a phosphor coated fiberoptic screen. The phosphor generates fluorescence upon impact of the electron cloud from the MCP. The impact positions are recorded by detecting the light flashes with the camera. A $\varnothing$ 75 mm detector (Photonis Limited) was used for ion imaging in the present work. It utilizes a standard P47 (Y_2SiO_5:Ce) phosphor that emits a short-lived ($\sim$50 ns) blue fluorescence peaked at 400 nm. Typical bias voltages used for detector operation are: $V_{\text{front}}^{\text{MCP}} = 0$ V, $V_{\text{back}}^{\text{MCP}} = +1900$ V, $V_{\text{screen}} = +5000$ V. Hamamatsu ORCA-R2 CCD camera is used to image the fluorescence light. Time-of-flight (TOF) information is received from the anode of one of the MCP (back or front) contacts of the

detector. Thus obtained TOF data cannot be correlated with spatial information, since the camera integrates events over time while the anode integrates events over the detector area. However, a certain selectivity can be achieved by introducing a duty cycle (detection window) for data acquisition. If the experiment requires imaging of particles with a known TOF, the detector can be "gated" in time domain. The MCP gain strongly depends on the bias voltage and is essentially suppressed if the potential difference between the front and the back sides of the MCP stack falls below a certain threshold ($\sim$1200 V for the described PSD). We introduce a temporal gate with a fast high-voltage pulser (Behlke GHTS30). The pulser produces flat-top voltage pulses and supplies the MCP with the required bias voltage during a time window tuned to the arrival time of the desired particles. The window can be as short as 100 ns. The gating technique gives a possibility to image ions with a specific mass-to-charge ratio.

4 Results and discussion

4.1 Photoionization of C_{60} with UV light

In the present study tunable short UV laser pulses are used to ionize C_{60} in a two-photon ionization process. Multiphoton ionization studies of C_{60} with short laser pulses reported before (see e.g. [50] and references therein) were typically performed in the photon energy range 1.5–3.1 eV. These energies are way below the IP of neutral C_{60} which is 7.6 eV. In this case at least three photons are required to ionize the molecule. Such multiphoton excitation involves complex energy relaxation processes between different degrees of freedom of the molecule. Here we employ relatively high photon energies between 5 and 6 eV in order to simplify the light–molecule interaction picture to a two-photon process: absorption of the first photon excites the molecule and subsequent absorption of the second photon of the same energy leads to ionization. These photon energies fall within a broad photoabsorption band between 200 and 250 nm previously reported by Smith for gas phase neutral C_{60} [111]. In our experiments we utilize 50-fs laser pulses which are shorter than the characteristic timescales of energy relaxation due to nuclear motion in C_{60}. Therefore, the electronic excitation is, to a large extend, decoupled from relaxation processes due to coupling to nuclear degrees of freedom. In this case wavelength-resolved single pulse experiments will give direct information on the linewidth of the resonance, i.e. the lifetime of the transient optically excited state. Using a one-color pump-probe scheme the two photoabsorption processes (excitation and photoemission) can be separated in time. This allows to excite dynamics that initially involve a relatively narrow band of electronic states and then probe the system's relaxation with a delayed photon of the same energy. Such approach provides direct information about the transient state dynamics.

The next sections of the present thesis are related to this subject and are organized as follows. The excitation spectrum of free C_{60} molecules calculated by means of time-

dependent density-functional theory is presented in Section 4.1.1. Experimental data on the wavelength-dependent ionization of C_{60} in the range 216–222 nm are reported in Section 4.1.2. Section 4.1.3 describes time-resolved one-color pump-probe results on the transient state dynamics excited by UV laser pulses. Section 4.1.4 presents the theoretical methods used for calculations supporting the experimental data. Section 4.1.5 gives the discussion and conclusion.

4.1.1 Calculation of the excitation spectrum

The excitation spectrum of C_{60} in the UV–vis range was calculated [112] with the linear-response TDDFT approach known as the Casida method [113] by our collaborators in the Martin Luther University of Halle-Wittenberg (M. Shüler and J. Berakdar). As the first step, occupied and unoccupied Kohn-Sham (KS) orbitals of neutral C_{60} were computed with the OCTOPUS package [114]. The excitation spectrum is approximated by singly-excited (one excited electron–hole pair per state) manybody states $|\Phi_\alpha\rangle$ with energies E_α represented in the KS basis as:

$$|\Phi_\alpha\rangle = \sum_{i\in\text{occ}} \sum_{j\in\text{unocc}} A_{ij}^{\alpha} \hat{c}_j^{\dagger} \hat{c}_i |\Phi_0\rangle, \tag{4.1.1}$$

where $|\Phi_0\rangle$ is a determinant built by the occupied (ground-state) KS orbitals and $\hat{c}_j^{\dagger}$ ($\hat{c}_i$) is the creation (annihilation) operator with respect to the KS basis. The amplitudes A_{ij}^{α} are obtained from solutions of the Casida equations [113]. The computed excitation spectrum of C_{60} is shown in Fig. 4.1.1a. One can distinguish two types of states here: states accessible by dipole excitation from the ground state (GS)—"bright" states (BS)—and states with vanishing dipole transition moment—"dark" states (DS). Computed energies of the first three bright states (denoted as C, E and G in the figure) are in good agreement (albeit their energies are slightly underestimated, which is typical for TDDFT) with experimental absorption spectra reported by Smith for gas-phase C_{60} molecules [111]. Projection of the photoexcitation G onto the KS basis is depicted in Fig. 4.1.1b. The electron density distributions and corresponding angular momentum characters of the relevant KS orbitals are illustrated in Fig. 4.1.2. Despite the fact that C_{60} has high density of states in the vicinity of G, the number of transitions accessible for single-photon excitation from the ground state is very limited. As can be seen from Fig 4.1.1, the transitions mainly contributing are: (i) from HOMO-1 to LUMO+2 and (ii) from HOMO to two states with predominant

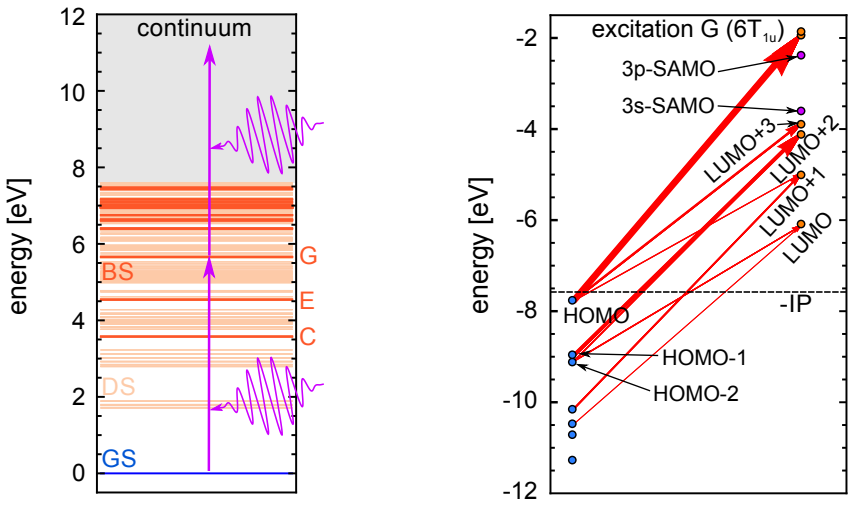

Figure 4.1.1: (a) Excitation spectrum of a free C_{60} molecule starting from the ground state (GS). In the dipole approximation optically accessible states are denoted as "bright" states (BS) and are marked by dark orange color. States with vanishing dipole transition moments are denoted as "dark" states (DS) and marked by pale orange. Purple arrows denote two 5.7 eV (218 nm) photons required for ionization. The first three "bright" excitations are labeled as C, E and G according to the notation suggested in [111]. (b) Projection of G onto the KS basis. The relative weight of each transition is denoted by the thickness of the red arrow. Figure from [112].

angular momenta $L = 8$ and $L = 6$ lying above the $3p$-SAMO. We note that the two lowest lying SAMOs, $3s$ and $3p$, cannot be populated by direct single-photon transitions from the ground state according to the calculations.

4.1.2 Excitation energy–resolved photoionization study

The energy-resolved photoionization study was performed in the single-pulse regime, i.e. C_{60} molecules are excited by the absorption of one photon and then ionized by the absorption of an additional photon from the same pulse. The details of the experimental setup are given in Chapter 3. In short, the 100 fs 2 µJ UV pulses were directed into the chamber where they interacted with the C_{60} molecular beam. The split-and-delay unit was replaced by a plane aluminium mirror that has reflectivity $\sim 80\,\%$ in the 200–245 nm range. The effusive molecular beam was produced by evaporating gold grade C_{60} powder at a temperature $T_{\text{evap}} = 775\,\text{K}$. The ions were detected with a standard VMI spectrometer [105] built previously in our group [115]. The spectrometer was operated in the time-of-flight (TOF) mode, i.e. only temporal information was recorded. The laser

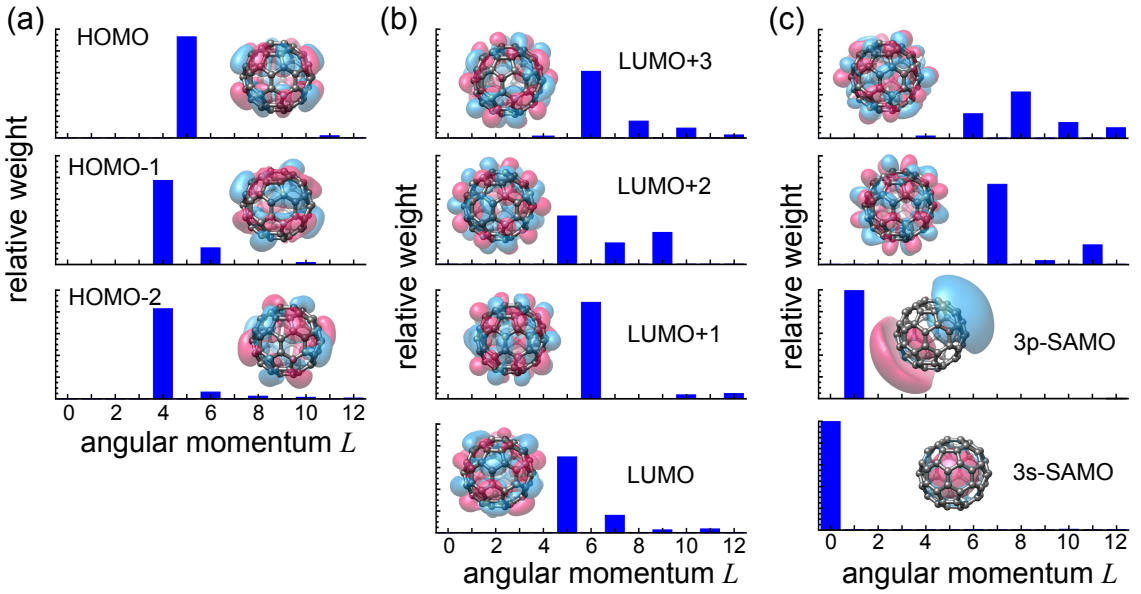

Figure 4.1.2: Occupied and virtual KS states close the negative ionization potential (IP) ordered (from bottom to top) according to Fig. 4.1.1b. The respective orbital character is illustrated by the relative weight of each angular momentum component L. Only one representative of degenerate states is shown. (a) Occupied states; (b) virtual states below the SAMOs; (c) orbitals including the SAMOs and higher states. Figure from [112].

pulses were focused by a spherical multilayer mirror with a focal length $f = 300\,\text{mm}$ and a reflectivity $> 80\,\%$ in the respective wavelength range. The beam waist in the interaction area was on the order of $150\,\mu\text{m}$. The peak laser intensity in the interaction area reached $\approx 3.5 \times 10^{10}\ \text{Wcm}^{-2}$ as was estimated from the measured pulse energy, pulse duration and the laser beam profile.

A typical TOF ion mass spectrum recorded after ionization of C_{60} molecules with short laser pulses in the wavelength range 216–220 nm is shown in Fig. 4.1.3. Typical voltages for the repeller and extractor electrodes of the VMI were set to $V_{\text{rep}} = +5900\,\text{V}$ and $V_{\text{ext}} = +4000\,\text{V}$, while the drift tube was kept grounded. The flight time of C_{60}^{+} ions for these voltage settings is $\approx 11\,\mu\text{s}$. The mass peak at $7\,\mu\text{s}$ belongs to residual gas ions. Due to the rather low laser intensity no multiply charged fullerenes were observed in the TOF mass spectrum.

Different UV wavelengths were obtained by tuning the IR output of the TOPAS (see Section 3.3). The central wavelength of the beam entering the chamber was calculated from the measured spectra of the two components of the last SFG stage—400 nm and tunable 470–495 nm. A typical spectral jitter for the both wavelengths was $\pm 0.3\,\text{nm}$. The

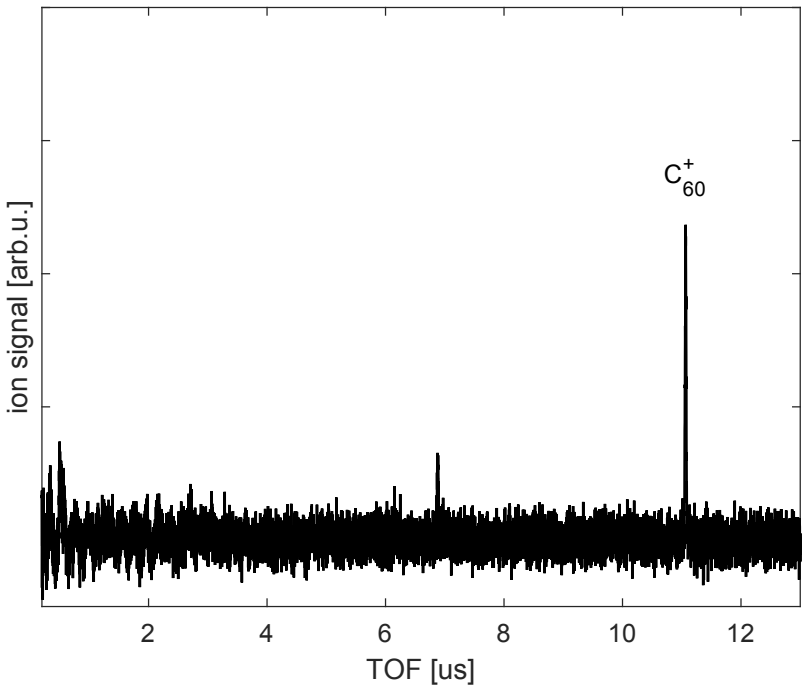

Figure 4.1.3: Typical ionic time-of-flight spectrum of C_{60} recorded after the interaction with a single 218 nm 100 fs laser pulse.

relative pulse energy was monitored with a silicon photodiode (Optodiode AXUV100G). Approximately 250 single-shot mass spectra were taken per wavelength point. To obtain the ionization yield the C_{60}^+ mass peak was integrated for each shot and normalized on the number of shots and the average pulse energy given by the diode for each wavelength.

The C_{60}^+ yield as a function of laser wavelength is shown in Fig. 4.1.4. A clear resonance peak is visible. The low-wavelength cutoff at 216 nm corresponds to the TOPAS wavelength tuned to 1140 nm which is on the limit of its performance range. The corresponding pulse energy is weak and exhibits substantial shot-to-shot energy fluctuations, which result in low pulse energy with significant fluctuations for every subsequent SFG stage as well. Large error bars on the detected ion signal for short wavelengths are the consequence of that. Beyond 219 nm the C_{60}^+ signal steadily decreases until its complete disappearance at 222 nm. Hence, this wavelength can be considered as the low-energy edge of the resonance. The FWHM of the observed peak is ~ 3.65 nm (94 meV). The lifetime of the transient excited state is estimated from the resonance linewidth. For this, the experimental data is fit by a convolution of the laser pulse spectrum of 2.8 nm FWHM and a Lorentzian function describing the homogeneous broadening. A characteristic time of 10^{+5}_{-3} fs is derived, which gives a lower bound of the excited state lifetime.

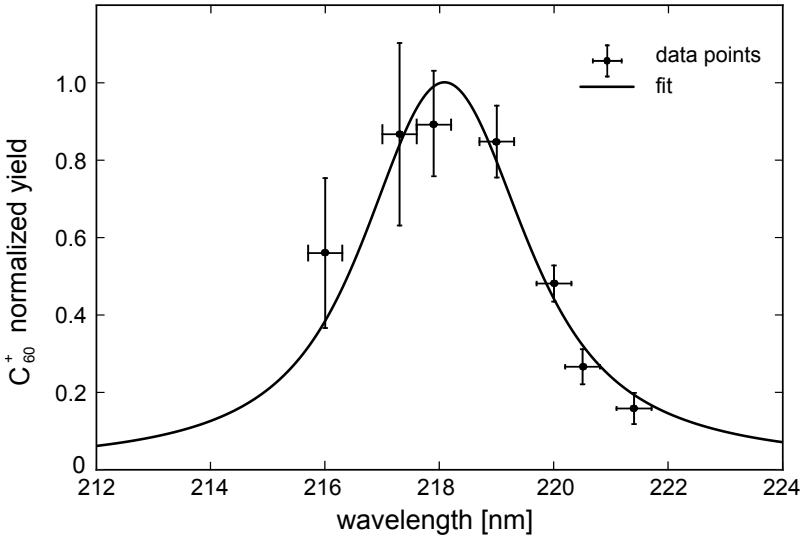

Figure 4.1.4: C_{60}^+ yield recorded as a function of laser wavelength.

4.1.3 Time-dependent pump-probe study

The time-resolved measurement was performed as a one-color pump-probe variable-delay scan. In this scenario the first pulse initiates dynamics of the sample which is then probed (i.e. ionized) by a pulse replica delayed by time τ. The ion yield recorded as a function of τ provides information on relaxation dynamics of the transient state.

4.1.3.1 Experiment

A silicon double-mirror SDU, similar to one depicted in Fig. 2.3.6a, was employed to generate a double-pulse sequence. The wavelength of the laser system was tuned to the maximum of the resonance obtained from the wavelength scan, i.e. 218 nm (see Fig. 4.1.4). Single-shot ion mass spectra were taken at variable delays in the range -60–900 fs. Approximately $\sim$ 3000 shots per delay point were taken in order to have sufficient statistics. The time-dependent on-resonance ion signal is derived by taking the average number of detected C_{60}^+ counts for each delay and normalizing it to the relative pulse energy monitored as the UV stray light peak in the TOF spectrum. The scan was performed two times. The result is presented in Fig. 4.1.5.

4.1.3.2 Extraction of the characteristic relaxation time constant

In general, the recorded ion yield from two-photon ionization of a system with a transient unoccupied state exposed to resonant light will contain contributions from two ionization pathways: (i) direct (coherent) two-photon ionization from the ground state to the continuum and (ii) two-photon ionization via the transient state. The first ionization pathway is obviously nonlinear and proceeds without populating any real excited states. The yield of this process is proportional to the square of the laser intensity I^2 according to Eq. (2.1.2). The second ionization pathway—resonance-enhanced multiphoton ionization (REMPI)—creates a real transient electron population in the excited state. As was discussed in Section 2.3.5, the yield of this process may depend on many parameters, such as laser intensity, number of photons involved in the transitions, resonance width and relaxation dynamics. In a case of a two-photon REMPI process absorption of the first photon promotes an electron to the transient state and subsequent absorption of the second photon by the same electron leads to photoemission. This process typically has linear dependence on the laser intensity and its τ-dependence in the autocorrelation experiment will reflect the dynamics of the excited state evolution.

Already from the present phase-averaged measurement an important information can be extracted: the lifetime of the transient population. This can be done in a fitting procedure as described in the following. The direct ionization pathway contains no memory of the excitation step and thus the ion yield of this channel as a function of τ is proportional to the second-order autocorrelation function of the laser pulse. The yield of the REMPI process depends on both, the population dynamics of the transient state and the temporal profile of the laser field. Therefore, the total ion yield $S_{\mathrm{tot}}(\tau)$ can be decomposed into a sum of three components [116,117]: (i) a coherent component (also called coherent artifact) $S_{\mathrm{ac}}(\tau)$; (ii) an incoherent component $S_{\mathrm{inc}}(\tau)$; (iii) a constant background a_{bg}. The coherent artifact describes the nonlinear process and is proportional to the intensity autocorrelation function $G_2(\tau)$ described in detail in Section 2.3.2:

$$S_{\mathrm{ac}}(\tau) \propto G_2(\tau) = \int_{-\infty}^{+\infty} \mathcal{E}^2(t)\mathcal{E}^2(t-\tau)\,\mathrm{d}t, \tag{4.1.2}$$

where $\mathcal{E}(t)$ is the laser field envelope. The incoherent term $S_{\mathrm{inc}}(\tau)$ is a convolution of $S_{\mathrm{ac}}(\tau)$ with a symmetric decay function reflecting the population dynamics of the transient

state. In case of exponential decay with a rate $\gamma_{\mathrm{dec}} = \tau_{\mathrm{dec}}^{-1}$, $S_{\mathrm{inc}}(\tau)$ takes the form:

$$S_{\mathrm{inc}}(\tau) = \int_{-\infty}^{+\infty} S_{\mathrm{ac}}(t-\tau)\mathrm{e}^{-|t|/\tau_{\mathrm{dec}}}\,\mathrm{d}t. \tag{4.1.3}$$

The background a_{bg} results from the individual action of each pulse and is independent of the delay. The total signal recorded by the detector then reads as:

$$S_{\mathrm{tot}}(\tau) = a_{\mathrm{ac}}S_{\mathrm{ac}}(\tau) + a_{\mathrm{inc}}S_{\mathrm{inc}}(\tau) + a_{\mathrm{bg}}, \tag{4.1.4}$$

where a_{i} are the relative amplitudes of the corresponding terms. In general, the ratio of these amplitudes depends on the involved ionization pathways and spatial overlap of the two pulses. To extract τ_{dec} from the measurement the experimental data is fit by the least squares routine using Eq. (4.1.4). The unknowns a_{ac}, a_{inc} and τ_{dec} are left as free parameters for the fit. The data together with the fit are shown in Fig. 4.1.5. The amplitude ratio given by the best fit is:

$$a_{\mathrm{ac}} : a_{\mathrm{inc}} : a_{\mathrm{bg}} = 0.24 : 1.13 : 1, \tag{4.1.5}$$

which indicates that the nonlinear ionization pathway does not contribute to the signal significantly. This is not surprising, since the direct ionization is dominated by the laser intensity, which was as low as $3.5 \times 10^{10}\,\mathrm{Wcm}^{-2}$ in the present study. These results clearly show that the experimental conditions were correctly chosen in order to simplify the excitation cascade as planned. The ratio between the REMPI component and the background is close to unity as expected for single-photon ionization from an occupied transient state. From the evaluation we derive a population decay constant of $\tau_{\mathrm{dec}} = 400 \pm 100\,\mathrm{fs}$ (95% confidence band). This value is not far from previously reported electron–vibron coupling times on the order of 200–300 fs [30,37]. In the following, we dwell a bit on the theoretical description and understanding of the experimental data presented above. A comprehensive view and the full picture is then given in Section 4.1.5.

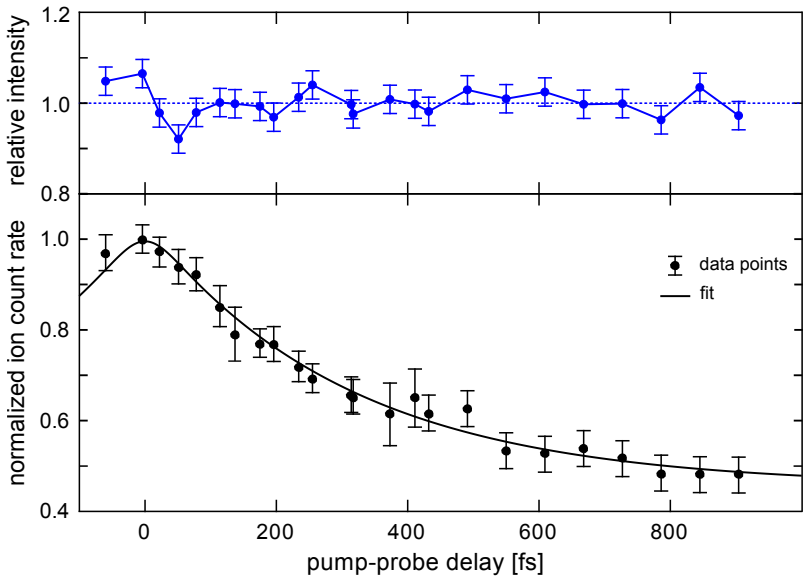

Figure 4.1.5: The C_{60}^{+} ion yield recorded as a function of pump-probe delay (bottom). The black dots are the data and the red curve is the fit according to Eq. (4.1.4). Top: the relative pulse energy estimated as a stray light peak.

4.1.4 Theoretical calculations

Resonant two-photon ionization can be regarded as a sequential two-step process, each involving absorption of one photon—excitation and ionization—with transient dynamics taking place in between the photoabsorption events. The excitation step is especially important as it defines to large extend the following evolution of the system and thus the outcome of photoemission. A mixed theoretical approach is used in the present study to describe the two-photon ionization in order to reduce the computational costs: the transient excitation (population) is propagated in time domain using the density matrix approach, while for the description of single-photon photoemission from the excited state the steady-state perturbation theory is used. The justification of this approach will be given in Section 4.1.5.

4.1.4.1 Dynamics of transient population

An exact theoretical description of ionization processes in complex systems, such as C_{60}, requires to take into account electronic and nuclear degrees of freedom as well as their interaction. Equal numerical treatment of both is not feasible due to high computational costs. One has to rely on certain approximations instead. One of the typical choices when

calculating the electronic structure and dynamics of molecules is the Born-Oppenheimer approximation that neglects coupling of different electronic states through the nuclear motion. This approximation holds for the electronic ground state of many molecules and small nuclear displacements. However, in the excited state manifold electronic and nuclear dynamics often become mixed through nonadiabatic coupling, which leads to the break-down of the Born-Oppenheimer approximation. The fullerene molecular beam in the experiment was produced by evaporation of solid powder at $T_{\mathrm{evap}} = 775\,\mathrm{K}$. At this temperature an energy of several eV is deposed in the vibrational modes of the molecule. This is still insufficient to induce vibronic transitions from the ground state of C_{60}, but considering the high density of states in the vicinity of the band G (Fig. 4.1.1), subsequent electron–vibron coupling comes into play upon photoexcitation.

The calculations presented here are restricted to the harmonic approximation of the bottom of the Born-Oppenheimer surfaces. Frequencies and reduced masses of vibrational modes in C_{60} were computed with OCTOPUS software package [112]. High-energy vibrational modes, which affect electrons most, are weakly populated at 775 K [112], therefore oscillations of nuclei around their equilibrium positions can be considered small. and the electron–vibron coupling can be approximated as linear. Hence, the Herzberg–Teller (HT) expansion [118] of the full Hamiltonian, including electrons and nuclei, yields a reasonable description for both subsystems and their interaction. The first-order HT Hamiltonian amounts to approximating the electron–vibron coupling as linear in the mode amplitudes $\hat{Q}_\nu$. On the KS level, the electron–vibron matrix elements are thus given by:

$$k_{ij}^{\nu} = \langle \phi_i | \frac{\partial v_{\mathrm{KS}}}{\partial Q_\nu} | \phi_j \rangle \Big|_{Q_\nu = 0}. \tag{4.1.6}$$

Here, v_{KS} is the Kohn-Sham potential which depends, in a general case, on the coordinates of all N nuclei of the molecule, i.e. $v_{\mathrm{KS}} = v_{\mathrm{KS}}(\mathbf{r}, \mathbf{R}_1, ..., \mathbf{R}_N)$. For the simulation the matrix elements k_{ij}^{ν} are transformed into the manybody basis set $|\Phi_\alpha\rangle$ (Eq. (4.1.1)) and their representations $K_{\alpha\beta}^{\nu}$ are then used in calculations. The time-dependent Hamiltonian of the system then reads as:

$$\hat{H}(t) = \hat{H}_{\mathrm{el}}(t) + \hat{H}_{\mathrm{vib}} + \hat{H}_{\mathrm{el–vib}}, \tag{4.1.7}$$

with

$$\hat{H}_{\mathrm{el}}(t) = \sum_{\alpha} E_{\alpha} |\Phi_{\alpha}\rangle\langle\Phi_{\alpha}| + \mathcal{E}(t) \sum_{\alpha\beta} M_{\alpha\beta} |\Phi_{\alpha}\rangle\langle\Phi_{\beta}|, \tag{4.1.8a}$$

$$\hat{H}_{\mathrm{vib}} = \frac{1}{2} \sum_{\nu} \left(\frac{\hat{P}_{\nu}^2}{M_{\nu}} + k_{\nu} \hat{Q}_{\nu}^2 \right), \tag{4.1.8b}$$

$$\hat{H}_{\mathrm{el-vib}} = g \sum_{\alpha\beta} \sum_{\nu} K_{\alpha\beta}^{\nu} |\Phi_{\alpha}\rangle\langle\Phi_{\beta}| \hat{Q}_{\nu}. \tag{4.1.8c}$$

Here, $|\Phi_{\alpha}\rangle$ and E_{α} are the eigenstates and eigenenergies in the basis calculated from Eq. (4.1.1), $M_{\alpha\beta}$ are the dipole transition matrix elements calculated by the Casida method, $\mathcal{E}(t)$ is the laser field envelope, $\hat{P}_{\nu}$ is the momentum operator for the nuclei, M_{ν} is the reduced mass of the vibrational mode ν, and k_{ν} is the force constant. The prefactor g in Eq. (4.1.8c) is introduced as an overall scaling factor for the strength of the vibronic coupling. Ideally, $g = 1$ should be fixed. However, due to the perturbative description resulting from the Herzberg–Teller expansion, the electron–vibron interaction might be underestimated. Hence, g is kept as a parameter. The temporal evolution of the density matrix in the basis of the manybody states $|\Phi_{\alpha}\rangle$ is treated by solving the Lindblad maser equation [119].

Population dynamics of ground, "bright" and "dark" states in C_{60} after excitation by a single 100 fs laser pulse with an amplitude corresponding to intensity of 3.5×10^{10} Wcm^{-2} and photon energy of 5.66 eV is shown in Fig. 4.1.6. It is clearly seen from the figure that the population transfer between the ground state and the "bright" excited states is clearly not in the perturbative regime, as two Rabi cycles are apparent during the 100 fs UV pulse interaction. The relaxation dynamics, transferring part of the excitation to the dark states, takes place on two time scales: for short delays one can observe a rapid energy transfer, while for longer times the distribution thermalizes. The depletion dynamics of the laser-excited BS primarily takes place due to the coupling to two lower-energy states at ≈ 5.5 eV (see Fig. 4.1.6b). Closer inspection reveals that these DSs involve the excitation of the $3s$- and the $3p$-SAMOs. The respective weights are given in Fig. 4.1.6a. This relaxation mechanism is the dominant consequence of the electron–vibron coupling. This behavior is expected, as dissipation pathways are generally preferred compared to bath-induced excitations. These thermalization processes are hence less pronounced and occur on a longer time scale.

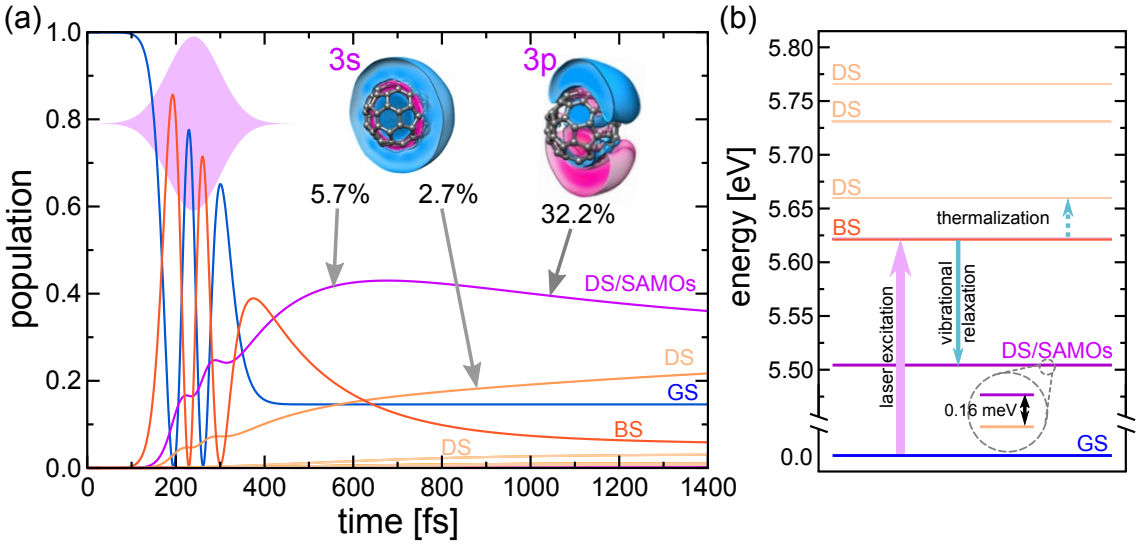

Figure 4.1.6: (a) Calculated population dynamics induced by the pump pulse (sketched in the background). The color coding of ground state (GS), "bright" states (BS) and "dark" states (DS) is identical to Fig. 4.1.1. The insets show the weight of the $3s$- and $3p$-SAMOs in the dominantly populated states. The DS involving the strongest SAMO excitations is highlighted by the purple color. (b) Dominant population mechanisms for the dynamics in (a). Figure from [112].

4.1.4.2 Photoemission from excited states

Inclusion of the photoionization step into the approach described in the previous section requires a much larger density matrix which makes this method computationally expensive. Thus, a different approach is chosen instead. If the dynamics of the photoemission process is much faster than the duration of the laser pulse then the simplest approach is to use the steady-state perturbation theory.

The corresponding description of the pump-probe data takes into account the decaying population of the transient states $\rho_{\alpha\alpha}(t)$ obtained from propagating the density matrix as described in Section 4.1.4.1. Details of the calculation are explained in [112]. The total ionization pump-probe signal $S(\tau)$ is given by:

$$S(\tau) \propto \sum_{\alpha\beta} \int_{-\infty}^{+\infty} \mathrm{d}t \int_{-\infty}^{t} \mathrm{d}t' \mathcal{E}_{\mathrm{probe}}(t-\tau)\mathcal{E}_{\mathrm{probe}}(t'-\tau) P_{\alpha\beta}(E_\alpha + \omega)\rho_{\alpha\alpha}(t'), \qquad (4.1.9)$$

where τ is the pump-probe delay, ω is the photon energy, $\mathcal{E}$ is the probe pulse field envelope and $P_{\alpha\beta}$ is proportional to the energy-resolved ionization probability with respect to the initial state $|\Phi_\alpha\rangle$ and final state $|\Phi_\beta^+\rangle$. Such separate treatment of the excitation

and ionization steps on fundamentally different theoretical levels assumes that the pump pulse (defining $\rho_{\alpha\alpha}$) and the probe pulse (leading to ionization) are completely separated in time, i.e. in the present case it holds for $\tau > 300$ fs.

4.1.5 Discussion

4.1.5.1 Resonant excitation

Interestingly, the measured resonance linewidth with FWHM $\approx$ 4 nm is very narrow compared to the much broader, several tens of nm, band reported by Smith in this wavelength range [111]. The observation can be explained as follows. In the present study molecules are ionized with a short 100-fs laser pulses, while in [111] the author used a UV diode lamp. The 100-fs excitation is shorter than the typical electron–vibron coupling time in C_{60} (see Section 2.2.2 for details). In other words, the sequential absorption of two UV photons required for ionization occurs in a short time window leaving no time for significant energy dissipation. This picture is supported by calculations of the transient population dynamics induced by the short laser pulse (Fig. 4.1.6). As can be seen, the fraction of population transferred to "dark" states while the pulse is active is not large. Therefore, the majority of electrons accessible for ionization will originate from the "bright" states initially populated by photoabsorption. As was discussed in Section 4.1.1, the dipole-allowed excitation G (Fig. 4.1.1) of neutral C_{60} is comprised of a limited number of transitions which form an energetically narrow band. Therefore, the limited number of excitation and relaxation pathways serves as the bottleneck for the ionization process making the resonance width rather narrow. By contrast, if the light–molecule interaction time is long, as it is in the case when a diode lamp is used, energy redistribution takes place while the molecule is still exposed to the photon field. It may lead to the formation of a broad band of excited states with different binding energies accessible for single-photon ionization by "late" photons.

At high photon energies used in the experiment the absorption of the second photon by the excited molecule leads rather to immediate photoionization than to further excitation and energy exchange between different degrees of freedom within the neutral molecule. Moreover, the photoemission cross-sections from different excited states were found to be small [112]. Together with the low laser intensity used in the experiment, it gives strong support for the perturbative treatment of the photoemission step. Another corroboration for this picture is the low contribution of the nonlinear (coherent) ionization

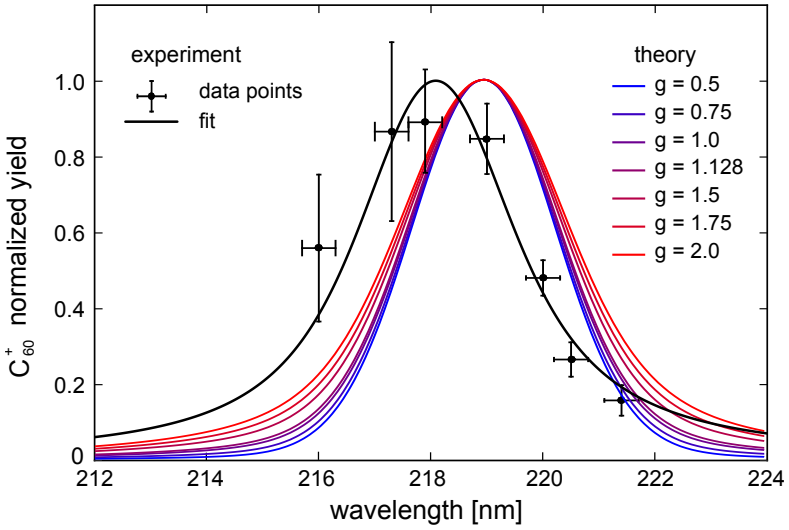

Figure 4.1.7: C_{60}^+ yield recorded as a function of laser wavelength. The colored lines correspond to calculations obtained using transient state populations $\rho_{\alpha\alpha}$ (Section 4.1.4.1) and Eq. (4.1.9) for different electron–vibron coupling strengths g. Figure from [112].

pathway to the pump-probe data.

The theoretical calculation of the C_{60}^+ ion yield as a function of laser wavelength taking into account the transient populations and Eq. (4.1.9) is shown in Fig. 4.1.7. The parameter g denotes a scaling factor for the electron–vibron coupling from Eq. (4.1.6). As expected, the increase of nonadiabatic coupling leads to a broader spectrum. For consistency check calculations of the wavelength-dependent ionization rate were also performed using steady-state perturbation theory for the description of both, excitation and photoemission, thus omitting the population dynamics. Apart from the spectral width of the peak, the result was similar to that obtained using the transient populations taken from the density-matrix approach.

4.1.5.2 Transient state dynamics

The characteristic relaxation time constant extracted from the autocorrelation measurement is $\tau_{\mathrm{dec}} = 400 \pm 100\,\mathrm{fs}$. It is much longer than the characteristic electron–electron coupling time in C_{60} which happens within 100 fs after the initial photoabsorption [37,50,120]. Therefore, the inelastic electron–electron scattering does not play a significant role in energy relaxation if the molecule is excited by short, weak, UV pulses in the photon energy range between 5 and 6 eV. Instead, energy dissipation is mediated by the coupling of electronic motion to nuclear degrees of freedom. As evident from

Fig. 4.1.6, nonadiabatic dynamics leads to effective population transfer from photoexcited "bright" states to dipole-forbidden "dark" states on a timescale of several hundred fs. Simulations of the pump-probe data for different electron–vibron coupling strengths g

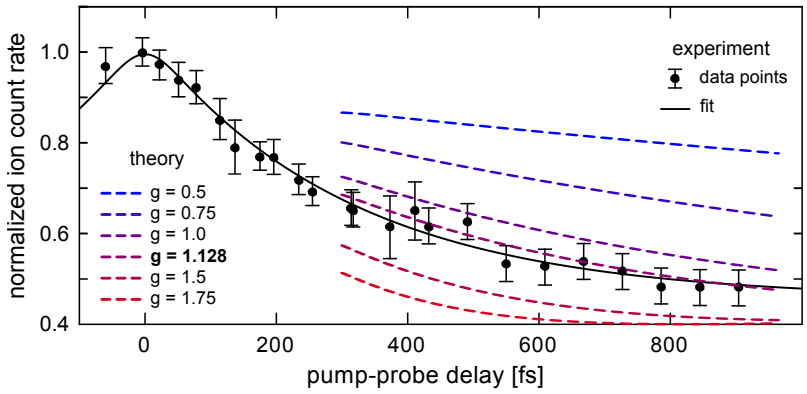

Figure 4.1.8: The autocorrelation C_{60}^{+} data with theoretical calculation using Eq. 4.1.9 for different scaling factors g of the electron–vibron interaction strength. The bold value indicates the best agreement between theory and experiment. Figure from [112].

for delays $\tau > 300$ fs are presented in Fig. 4.1.8. As expected, stronger coupling g leads to faster depopulation of excited electronic states and thus faster decline of the signal.

It was pointed out in Section 4.1.1 that although $3s$- and $3p$-SAMOs lie energetically in the vicinity of the G band, they are unaccessible for direct single-photon excitation from the ground state as the corresponding dipole transition moments are close to zero. However, the present analysis of the excited state dynamics reveals that these orbitals are populated via electron–vibron coupling along with other "dark" states according to the theoretical model (Fig. 4.1.6). Time-resolved experiments that can directly unravel the dynamics of SAMOs are still missing, in particular the lifetime of these diffuse states remains an open question for future studies. Their energy widths point towards very short lifetimes, in the order of several fs [53].

4.2 Commissioning of the ion spatial imaging setup

Design details of the grating split-and-delay unit (SDU) (Section 3.4.1), its optical performance and the importance of the imaging of the ionization volume with high spatial resolution are outlined in Section 2.3.4. Just a reminder of the SDU concept: the grating-like reflectors of the SDU produce several diffraction orders. Each of them will create an ionization channel in space upon focusing on a gas sample. Since the dispersion plane of the SDU is oriented perpendicular to the ion-spectrometer axis, individual channels can be imaged by projecting the ions on a position-sensitive detector (PSD).

The two most important aspects of the spatial imaging—the magnification factor and the velocity focusing—strongly depend on the exact position of the ionization volume with respect to the repeller and the extractor electrodes along the flight axis. The best conditions for each of this aspects are the opposite. Moving the ionization area closer to the repeller gives better velocity focusing but lower magnification. By contrast, placing it closer to the extractor provides higher magnification but results in a blurred image due to worse velocity focusing. Thus, the settings depend on size and shape of the ionization volume, resolution requirements and initial ion velocities. Simulations can provide guidelines for the nominal ion optics settings, but in practice the exact voltages and the focus position of the laser beam must be carefully adjusted to obtain the best image quality and are typically found empirically.

The experiment was carried out at FLASH, the free-electron laser (FEL) facility in Hamburg. The machine was operated with six undulator modules and a total undulator length of 30 m in 42 bunch mode (100 kHz). The electron bunch charge was 0.32 nC and the electron energy 410 MeV resulting in the central photon wavelength of 38 nm. The average photon pulse energy was about 80 µJ which corresponds to about 1.5×10^{13} photons per pulse at this photon energy. The measurements were performed at the PG2 monochromator beamline [121,122]. The monochromator comprised of a plane grating, collimating and focusing mirrors, and an exit slit with variable slit width was utilized to select a spectral region much narrower than a single SASE mode. The grating has a line density of 200 lines/mm and was tuned to the first diffraction order. Resolving power of the monochromator at 32.6 eV is $\sim$7000. The slit width was 70 µm during the experiment which corresponds to 4.6 meV bandwidth at 32.6 eV photon energy. XUV pulses were reflected from the SDU (Section 3.4.1) and focused into Xe gas (IP = 12.1 eV). The ionization volume was located in the extraction area of the electron–ion coincidence

spectrometer (Section 3.5). Xe^+ ions were projected onto the phosphor-based PSD (Section 3.5.4) and the fluorescence signal from the PSD was imaged with a CCD camera (Hamamatsu ORCA-R2, 1344 × 1024 pixels). In the present geometry the camera optics gives a resolution of 83.5 µm/pixel. The camera images were taken in a single-shot mode, i.e. the exposure was synchronized with arrival of FEL pulses. To increase the magni-

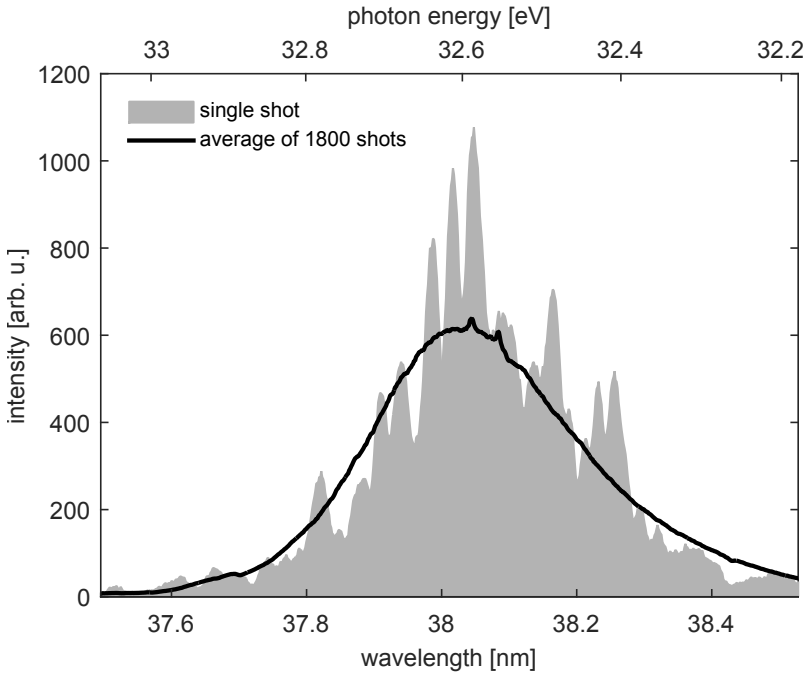

Figure 4.2.1: Typical single-shot and average FEL spectra [123].

fication factor the ion side of the spectrometer was elongated compared to the original design shown in Fig. 3.5.2. For the experiments presented below the detector was placed 670 mm away from the ionization volume. The optimal extraction voltages for spatial imaging in this geometry are given in Table 4.1. The lens on the electron side is operated at high positive voltage to correct for the field distortion in the extraction region due to the aperture in the electron extractor. The spatial image of the ionization volume is displayed in Fig. 4.2.2. It shows Xe^+ ions generated by an FEL beam propagating along z-axis after diffraction from a single grating reflector (from Fig. 3.4.1b) of the SDU. The three brightest traces in the color image correspond to 1^{st}, 0^{th} and -1^{st} diffraction orders. The integral of the image along the FEL propagation (the curve on the right side) reveals orders up to 4^{th}. According to wave-optics simulations (Section 3.4.1.2) the distance between two neighboring orders in the focal plane of the mirror for the present experimental conditions (38 nm wavelength, 250 µm grating period, 300 mm mirror focal length) is $\Delta_{foc} = 46\,\mu m$.

Table 4.1: Extraction voltages used for spatial imaging of ions.

Electrode	Voltage [V]
< ion detector >	
Drift tube (i)	0
Lens (i)	0
Extractor (i)	+5575
< ionization volume >	
Extractor (e)	+6000
Lens (e)	+6000
Drift tube (e)	0
< electron detector >	

The separation of two orders on the detector is $\Delta_{\text{det}} = 835\,\mu\text{m}$, which corresponds to a magnification factor of $M = 18.2$. The Xe gas was injected into the chamber through a valve placed far away from the ionization volume and experienced a number of collisions with chamber walls before reaching the ionization area. Thus, the nascent velocities of Xe^+ ions correspond to thermal velocity of Xe at room temperature, i.e. $\approx 220\,\text{m/s}$ according to Eq. 3.2.5. The position-sensitive ion detection demonstrates that the optical quality of the grating reflector is sufficient to obtain a clear diffraction pattern with 38 nm light. The partial overlap of the peaks can be attributed to the focal size of the FEL beam which makes the neighboring orders partially overlap, or to imaging properties of the electrostatic optics which cannot fully compensate for the velocity spread of Xe^+ ions. The experiment shows that though the setup is not a dedicated ion microscope, the resolution of the ion spectrometer in the spatial imaging mode is sufficient to perform fringe-resolved autocorrelation experiments at wavelengths as low as 38 nm.

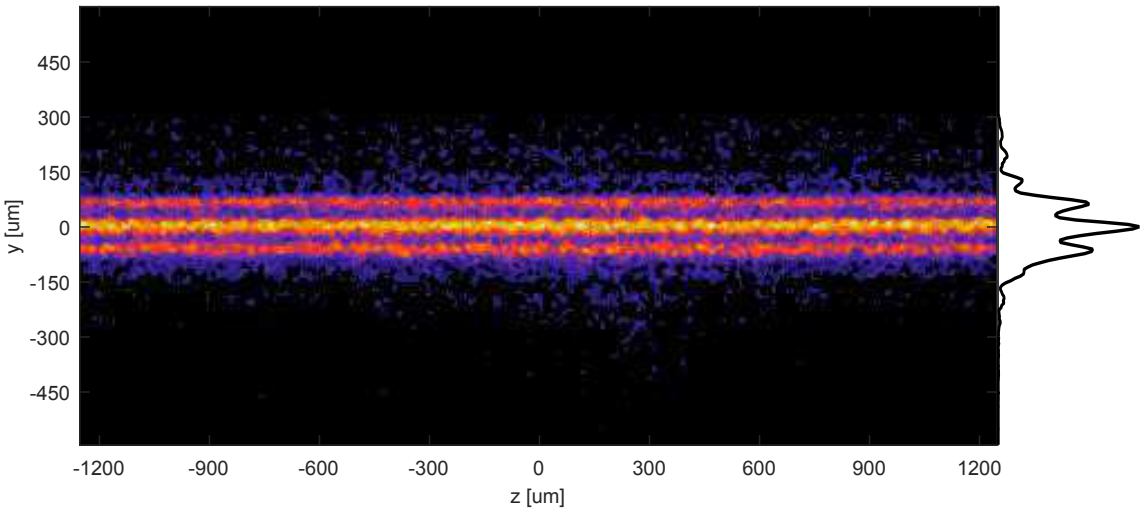

Figure 4.2.2: Spatial image (side projection) of the ionization volume after reflection from a single SDU grating reflector (color image). The FEL beam propagates along z-axis. The three brightest foci correspond to the 1^{st}, 0^{th} and -1^{st} diffraction orders generated by the grating. The integral of the image along the beam propagation direction (right) shows orders up to 4^{th}.

4.3 Field autocorrelation at 38 nm wavelength

All time-resolved autocorrelation experiments with FELs so far used split-and-delay units with a noncollinear overlap of the two partial beams, see e.g. [124]. Upon superposition on a screen, the two pulses produce spatial interference pattern (like in Fig. 2.3.5) with fringe visibility that depends on the temporal delay between them and their temporal and spatial degree of coherence. In a noncollinear geometry the longitudinal coherence is mapped on the transverse spatial distribution due to the mutual wavefront tilt of the partial beams. The fringe contrast as a function of autocorrelation delay provides information about temporal coherence properties of FEL pulses. Experiments give the temporal coherence length of self-amplified spontaneous emission (SASE) FEL pulse in the order of several fs [125–127]. This corresponds to the temporal width of a single SASE mode.

In our experiments we use the grating SDU providing a collinear overlap of the pulse replicas in space. In this case the tunable relative phase delay between the pulse replicas is constant across the full focus volume. The experiment was performed on the PG2 beamline of FLASH. The details of the experiment such as parameters of the FEL and settings of the spectrometer are described in Section 4.2. Xe gas used as a sample has the ionization potential of 12.1 eV which makes ionization with 38 nm (32 eV) light a single-photon process. According to Eq. (2.1.2), the ion yield of this process has a linear

dependence on the laser intensity I. Therefore, spatially resolved collection of Xe^+ ions as a function of autocorrelation delay will correspond to field autocorrelation (FAC) trace if the yield is plotted for a particular diffraction order.

As was mentioned in Section 3.4.1, the two grating reflectors of the SDU have different surface quality. The "ridged" grating (Fig. 3.4.1b) shows good optical quality for 38 nm wavelength as is justified by Fig. 4.2.2. Despite the slight asymmetry in the image, one can clearly distinguish individual diffraction orders. The surface quality of the second SDU reflector, the slotted grating (Fig. 3.4.1a), is worse. The area where the quality is acceptable for applications in the XUV wavelength range is limited and difficult to find with the FEL beam during operation. The focused FEL beam profiles after reflection from both SDU gratings are shown in Fig. 4.3.1. Here, a small tilt angle was introduced between

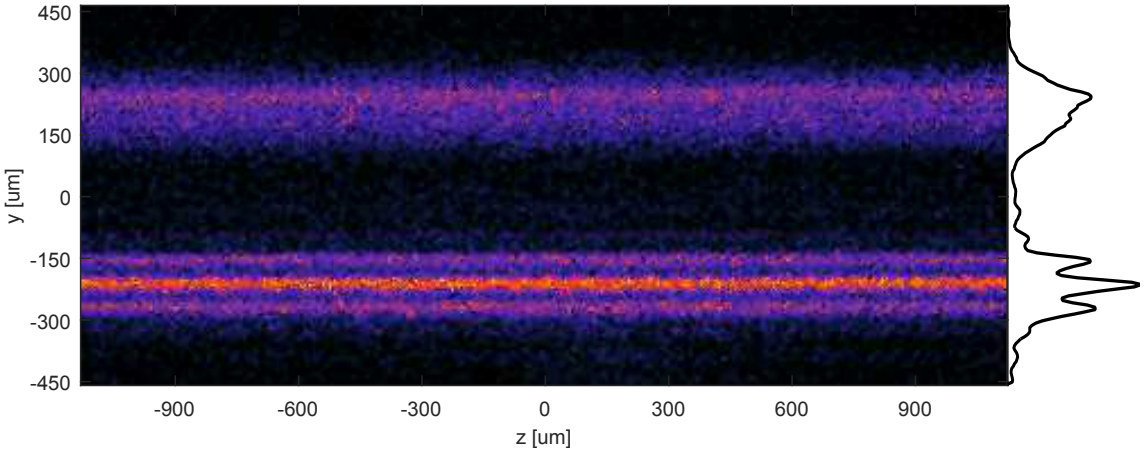

Figure 4.3.1: Color: spatial image (side projection) of the ionization volume after reflection from the two reflectors of the SDU. Upper trace: the beam from the "slotted" grating (Fig. 3.4.1a). Lower trace: the beam from the "ridged" grating (Fig. 3.4.1b). Right: integral of the image along the beam propagation direction (z-axis). The image is accumulated for $\approx$ 5000 FEL shots.

the two SDU reflectors to separate the photon beams in the ionization area. The upper ion trace corresponds to the slotted grating. As can be seen from the figure, the slotted grating produces a strongly distorted beam in contrast to the ridged grating. Though there is still structure visible corresponding to at least four diffraction peaks, they are obscured by a strong uniform background due to spatial phase distortions larger than 2π. Hence, one can expect the mutual spatial coherence of the two beams to be reduced. Fig. 4.3.2 illustrates the FEL focus shape when the beams of two gratings are superimposed. The parallel alignment of the gratings (mutual planarity) and thus the spatial overlap of the beams is ensured by the WLI system (Section 3.4.2).

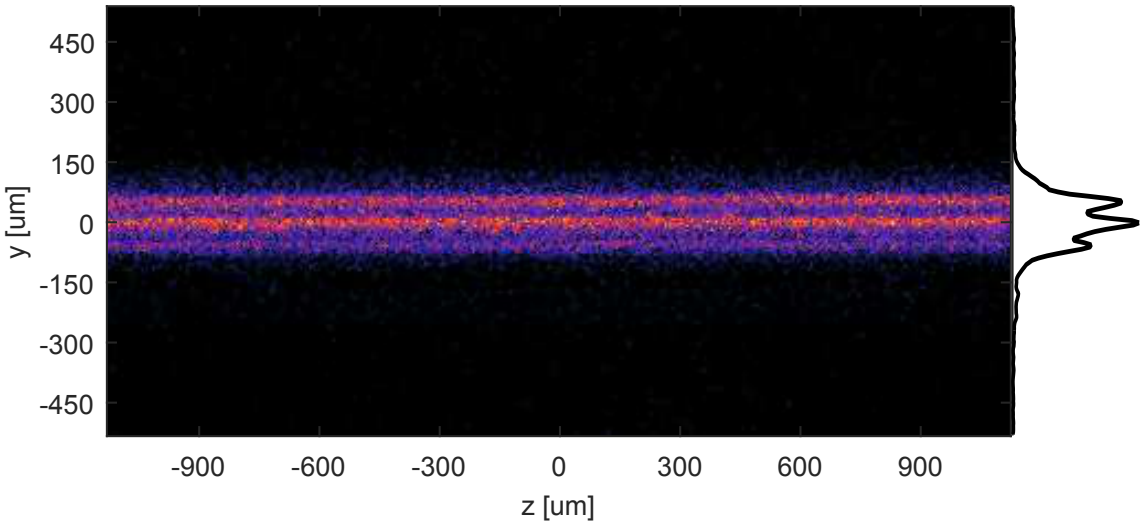

Figure 4.3.2: Color: Spatial image (side projection) of the ionization volume after reflection from the SDU with both gratings aligned parallel. Right: the integral of the image along the beam propagation direction.

In the autocorrelation experiment a delay scan in a range from -250 to 200 attoseconds was performed. The single-shot camera images were taken at 10 Hz repetition rate synchronized to FEL pulses. The MCP of the detector was "gated" as explained in Section 3.5.4 in order to reduce the background signal. A 500 ns wide temporal gate was tuned to the arrival of Xe^+ ions which have a TOF of $\sim 9.5\,\mu s$ when voltages in Table 4.1 are applied. The time zero was defined by monitoring the prompt photon peak from the FEL stray light. As was discussed in Section 3.4.2, due to vibrations in the experimental hall the position of the scanning piezo stage setting the delay exhibits a temporal jitter which is faster than the feedback loop readout. The exact autocorrelation delay τ for each laser shot thus has to be derived using the WLI data as explained in Section 3.4.2.2. For data processing the single-shot images from the position-sensitive detector were sorted according to the delay measured by the WLI. The distribution was binned into 15.84 as (1/8 of the optical cycle at 38 nm) time slots which can be regarded as an effective step size of the present experiment. All the images within one time bin were added up and normalized to the number of shots. The ion yield distribution across the focus was obtained by integrating the normalized images along the dimension corresponding to the beam propagation (the right image in Fig. 4.3.2). The distribution was fitted with several Gaussians describing individual diffraction orders plus a rather broad background structure obtained from fitting the spatial ion distribution generated by the "slotted" reflector

(upper trace in Fig. 4.3.1). Due to the remaining spatial coherence between the pulse replicas, the amplitude ratio between neighboring diffraction orders changes as a function of temporal delay τ on the sub-cycle time scale. The resulting fringe contrast of $\sim 4\,\%$ is clearly visible in Fig. 4.3.3. The figure shows the normalized ratio between the amplitudes of the fitted Gaussian peaks corresponding to zeroth and first diffraction orders as a function of τ. The experiment demonstrated that the setup can be used for fringe-resolved

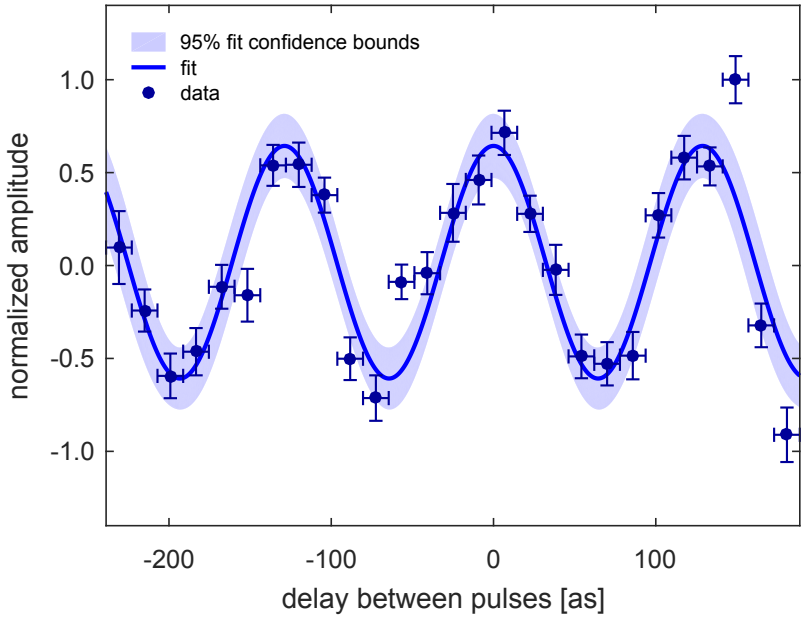

Figure 4.3.3: Relative intensity ratio of the zeroth and first diffraction orders as a function of autocorrelation delay τ. The fit corresponds to $\sin(2\pi c\tau/\lambda_{\mathrm{FEL}})$, where $\lambda_{\mathrm{FEL}} = 38\,\mathrm{nm}$ is the FEL central wavelength [128].

autocorrelation experiments in XUV wavelength range. Currently, we try to enhance the mutual spatial coherence of the beams reflected from the two components of the SDU by improving the surface quality of the optics, in particular of the slotted reflector. This should allow us to perform high-contrast interferometric experiments in non-linear phase sensitive spectroscopy.

5 Conclusions and outlook

The present thesis paves the way towards utilization of advanced nonlinear methodologies at short wavelengths to unravel energy, charge and information transport phenomena in small quantum systems on the attosecond time and nanometer length scale. The heart of the experimental setup is a reflective split-and-delay unit (SDU) for phase-resolved (coherent) one-color pump-probe (autocorrelation) experiments at VUV and XUV frequencies. The SDU splits the wavefront of a single incoming pulse uniformly across the beam profile by two interposed gratings and generates two pulse replicas with a variable time delay. The two gratings generate a number of diffraction orders and in each order the wavefronts of the two partial beams are parallel. In contrast to a conventional half-mirror SDU the above geometry provides collinear propagation of both pulses and thus constant phase difference across the beam profile, which enables to record phase-resolved (coherent) autocorrelation signals. Short wavelengths require high surface quality and motion control of the reflective optics on the sub-wavelength, i.e. nanometer length scale. Manufacturing of the gratings with high quality profiles proved to be nontrivial which is in particular true for the thin slotted grating. Slope errors result in wavefront distortion of the corresponding partial beam and reduce the mutual spatial coherence of the pulses to the order of several percent. However, even this value is sufficient to observe rich interference contrast as a function of time delay at the partially coherent XUV SASE FEL source FLASH using the monochromator beamline. It requires to control the delay between the pair of pulses on the attosecond timescale. For this task a delay diagnostics tool was developed during the thesis. It is based on an in-vacuum white light interferometer (WLI) allowing to monitor the actual relative displacement of the two SDU reflectors for each laser shot at a repetition rate of 10 Hz. In turn, it is possible to derive the corresponding autocorrelation delay with attosecond precision even in highly vibrational conditions.

Phase-resolved autocorrelation experiments with the developed SDU require selection of a single diffraction order. This is achieved by imaging the spatial distribution of

ions generated by the laser beam in a gas sample. Considering the small separation of orders for XUV wavelengths this requires an ion imaging device with sufficient magnification. The electron–ion coincidence spectrometer built during the present work is a versatile setup designed to detect electrons using the velocity map imaging (VMI) technique ions either in velocity- or spatial imaging mode. First experiments demonstrated that the spectrometer provides a magnification factor of 18.2 in the ion spatial imaging mode, which corresponds to resolution of 4.6 µm given by the camera pixel size. This is sufficient to clearly resolve the diffraction pattern generated by the SDU with the FEL beam at a wavelength as low as 38 nm.

A prototypical example studied in the course of the present thesis is the photophysics of C_{60} fullerenes. Energy- and time-resolved two-photon ion spectroscopy of C_{60} with short UV laser pulses combined with *ab initio* theoretical calculations performed by our collaborators from Martin Luther University of Halle-Wittenberg revealed complex dynamics of correlated manybody states. Ionization as a function of excitation energy showed that despite the high density of states in the excited manifold of C_{60}, dipole transitions on a timescale faster than the characteristic intramolecular energy dissipation limit the number of accessible excitation pathways. The theoretical predictions are in agreement with the observation of a narrow resonance. Time-resolved autocorrelation measurements allowed to pinpoint the main mechanisms of energy relaxation after the excitation. The characteristic population decay constant of 400 ± 100 fs observed by recording the C_{60}^+ ion yield as a function of UV pump–UV probe delay is in good agreement with previous reports of electron–vibron coupling times. The analysis of the computed transient electronic population showed that upon excitation the electron–vibron coupling dominates the energy flow in C_{60}. It mediates population transfer within the electronic subsystem and is the major channel for energy dissipation towards nuclear degrees of freedom. The theoretical calculations also predict that superatom molecular orbital (SAMO) states cannot be directly excited through single-photon dipole transitions. However, they can be populated on a longer timescale via nonadiabatic processes. Though, the pulse length used in the experiments is too long to resolve pure electron dynamics in the pump-probe data, evaluation of the resonance linewidth in wavelength-dependent single-pulse experiments suggests that the initial electronic relaxation can be as fast as $\tau_{el} = 10^{+5}_{-3}$ fs. The theoretical analysis indicates complex electron dynamics (Rabi oscillations) even at rather low laser intensity of 3.5×10^{10} Wcm^{-2}.

In future, we will further improve the flatness of the SDU grating reflector as a more compact and robust design is on the way. This will allow to avoid wavefront distortions upon reflection and thus enhance mutual spatial coherence of the partial beams. Mutual average temporal coherence of the two pulse replicas also can be improved by installing more sophisticated vibration-damping equipment on the chamber (i.e. reducing the delay jitter) and improving the fitting algorithm determining the delay from the white light interferometer data. Coherent pump-probe experiments at XUV frequencies open new opportunities for studying light-induced correlations in manybody systems, since the coherent light pulses can excite, probe and even modify the system's response in a controlled fashion. The development of XUV and soft X-ray interferometry is expected to pave the way to resolve details of ultrafast intramolecular electronic motion. For example, ultrafast hole migration is a universal response of complex molecules to sudden ionization or excitation [129]. It is driven by electron correlations within many-electron systems and occurs on a timescale from a few femtoseconds down to the attosecond regime. We also note, that the M-shell resonances of C, O and N lie within the tuning range of modern FELs (e.g. FLASH and FERMI), thus, experimental studies on organic compounds with impact in chemistry, biology and life science would be within reach. Scientific breakthroughs into this direction were achieved at FERMI FEL. For instance, a nonlinear four-wave mixing study has been performed revealing coherent phonon motion in a solid state sample [130]. The FEL-induced transient grating in their experiment combines ultrafast time resolution with energy and wavevector selectivity enabling studies of complex dynamics inaccessible by linear methods.

The spatial imaging properties, in particular the magnification factor, of the spectrometer can be improved without deteriorating its performance in the VMI mode by installing a set of lenses in the drift tube, like, e.g. in [109]. An increase of the magnification factor will allow to perform interferometric pump-probe experiments with shorter wavelengths which require higher spatial resolution. So far, the device was used only for spatial imaging of ions. Detection of electrons and ions in coincidence is possible with two delay-line detectors capable of recording three dimensional information (two coordinates and time-of-flight) for every event which provides detailed information on correlations mediating the molecular response to coherent light fields. In this case the spectrometer can be operated in two modes. One is the pure electron–ion VMI spectrometer. In this case the velocities of photoproducts are recorded which provides information about momentum and kinetic energy release in the ionization process. Alternatively, the

apparatus can be used in a mixed mode when electrons are detected in the VMI regime, while for ions spatially resolved information is recorded. In combination with the developed SDU this allows to trace evolution of excited electron wavepackets depending on the phase of the XUV laser field by observing changes in angular and kinetic energy distributions of photoelectrons. The observation of interference fringes in spatially-resolved electron detection would be extremely interesting. The inherent phase-dependence of the ionization process will allow to observe and study in great detail such aspects as decoherence and information transport in molecular systems of increasing complexity, e.g. in polycyclic aromatic hydrocarbons of different size. This paves way towards coherent control of electron motion since local electronic structure is accessible in the XUV and soft X-ray wavelength range.

The UV pulses with a duration of 100 fs utilized in the present time-resolved experiments are too long to observe pure electron dynamics in C_{60}. Future experimental work making use of shorter UV pulses shall reveal the predicted laser-driven Rabi oscillation and time-resolved transformation of the electronic orbitals, i.e. the coupling between different electronic states. Moreover, in the present work the pump-probe data was obtained using a double-mirror SDU, coarse delay sampling and relied solely on ion detection. Using interferometric pump-probe technique based on the developed SDU in combination with electron–ion coincidence spectroscopy will allow to trace dynamics of individual electronic states on ultimate timescale with sub-optical cycle precision. So far, no direct measurement of the SAMO lifetimes was reported. Combining time-resolved pump-probe spectroscopy and VMI may give important contributions by identifying electrons emitted from SAMOs due to their distinctive angular distribution. C_{60} is also known to exhibit remarkable behavior when the excitation energy lies beyond its ionization potential, i.e. on the giant plasmon resonance. Recent calculations reveal the complex multipole nature of this resonance that is excited in a very broad energy range from 15 to 60 eV [64]. The corresponding dynamics of this excitation involving many electrons occurs on the attosecond timescale and is to be experimentally investigated yet. Advanced nonlinear optics and short pulse spectroscopy at short wavelength, i.e. the developed SDU in combination with the electron-ion coincidence spectrometer may help to unravel details of the plasmon evolution in this nanosphere. Last but not least, nanoplasmonics is another hot topic in ultrafast science and technology with potential applications in material science, catalysis and life science, such as sensing, biomedical diagnostics, labels for biomedical research, cancer treatment, and nanoantennas for light-emitting diodes and solar energy

conversion [131,132].

Appendices

A Scalar diffraction theory

In the scalar diffraction theory light is treated as scalar phenomenon neglecting the vector nature of electromagnetic fields. The electromagnetic wave can be represented as:

$$E(x, y, z, t) = \frac{1}{2}\left(\tilde{u}(x, y, z)\tilde{E}(t) + \text{c.c.}\right)$$

Two criteria must be met for the above formula to be applicable [133]:

- size of apertures and objects $\gg \lambda$
- diffracting fields are not observed too close to the aperture

A.1 Rayleigh–Sommerfeld diffraction formula

It is convenient to consider the propagation of a light wave in three-dimensional space in a slab geometry, i.e. between parallel planes. The plane where the field is known we will call the source plane, and the area of interest we will call the image plane. Let the complex amplitude distribution of a monochromatic field with a wavelength λ in the source plane be $\tilde{u}(x, y; 0)$. We assume that this field will be the only that contributes to the field $\tilde{u}(x, y; z)$ in the image plane located at a distance z from the source plane. The two planes are separated by free space. In this case the complex amplitude of the field in the image plane can be described by the Rayleigh–Sommerfeld diffraction formula

[133,134]:

$$\tilde{u}(x,y;z) = \iint_{-\infty}^{+\infty} \tilde{u}(x',y';0)\frac{z}{2\pi}\frac{\mathrm{e}^{\mathrm{i}kr}}{r^2}\left(\frac{1}{r}-\mathrm{i}k\right)\mathrm{d}x'\,\mathrm{d}y' \tag{A.1.1}$$
$$= \iint_{-\infty}^{+\infty} \tilde{u}(x',y';0)\,h(r,z)\;\mathrm{d}x'\,\mathrm{d}y',$$

where x', y' and x, y are coordinates in the source and image planes, $\tilde{u}(x', y'; 0)$ and $\tilde{u}(x, y; z)$ are the respective complex electric fields, z is the propagation distance, $k = 2\pi/\lambda$ and $r = \sqrt{(x-x')^2 + (y-y')^2 + z^2}$. The factor:

$$h(r,z) \equiv \frac{z}{2\pi}\frac{\mathrm{e}^{\mathrm{i}kr}}{r^2}\left(\frac{1}{r}-\mathrm{i}k\right) \tag{A.1.2}$$

is called the impulse response function of free space. Due to the coordinate differences entering r in $h(r, z)$, Eq. (A.1.1) can be seen as a two-dimensional convolution with a fixed z:

$$\tilde{u}(x,y;z) = \iint_{-\infty}^{+\infty} \tilde{u}(x',y';0)\,h(x-x',y-y';z)\;\mathrm{d}x'\,\mathrm{d}y'$$
$$\equiv \tilde{u}(x,y;0) * h(x,y;z). \tag{A.1.3}$$

For simple sources (e.g. circle, slit, etc.) $\tilde{u}(x, y; 0)$ the expression for $\tilde{u}(x, y; z)$ can be derived analytically and does not require the evaluation of the integral (A.1.1). But in most situations it is not possible and a numerical approach has to be used. The direct numerical evaluation of the integral in real space can be time consuming, but can be done much faster in Fourier domain.

A.2 Angular spectrum of plane waves

A monochromatic scalar wave field can be decomposed into the so-called angular spectrum of plane waves—a superposition of plane wave components with amplitudes that are a function of the direction cosines of the propagation vector. The angular spectrum

$\tilde{U}(f_x, f_y; z)$ of the field $\tilde{u}(x, y; z)$ in a slab geometry (with a fixed propagation distance z) can be expressed as a Fourier transform of $\tilde{u}(x, y; z)$ [69]:

$$\tilde{U}(f_x, f_y; z) = \iint_{-\infty}^{\infty} \tilde{u}(x, y; z) \mathrm{e}^{-\mathrm{i}2\pi(f_x x + f_y y)} \, \mathrm{d}x \, \mathrm{d}y \equiv \mathcal{F}\{\tilde{u}(x, y; z)\}, \tag{A.2.1}$$

where $(f_x, f_y) = \left(k_x/2\pi, k_y/2\pi\right)$ are spatial frequencies and k_x, k_y are projections of the wavevector $\mathbf{k} = k_x\hat{\mathbf{x}} + k_y\hat{\mathbf{y}} + k_z\hat{\mathbf{z}}$ on the corresponding coordinate axes. As it is shown in [135], if $\tilde{U}(x, y; 0)$ is the angular spectrum of the field in the source plane, the angular spectrum at a distance z from the source can be obtained as:

$$\tilde{U}(f_x, f_y; z) = \tilde{U}(f_x, f_y; 0) \mathrm{e}^{\mathrm{i}2\pi f_z z}. \tag{A.2.2}$$

Recalling that $f_z = k_z/2\pi$ and $k_z = \sqrt{k^2 - k_x^2 - k_y^2}$ the above expression can be rewritten as:

$$\tilde{U}(f_x, f_y; z) = \tilde{U}(f_x, f_y; 0) \mathrm{e}^{\mathrm{i}2\pi z\sqrt{\lambda^{-2} - f_x^2 - f_y^2}} = \tilde{U}(f_x, f_y; 0) H(f_x, f_y; z) \tag{A.2.3}$$

with

$$H(f_x, f_y; z) \equiv \mathrm{e}^{\mathrm{i}2\pi z\sqrt{\lambda^{-2} - f_x^2 - f_y^2}} \tag{A.2.4}$$

being the so-called free-space transfer function in spatial-frequency domain. The field perturbation $\tilde{u}(x, y; z)$ in the coordinate space at a distance z from the source is related to its angular spectrum in the frequency space via the inverse Fourier transform:

$$\tilde{u}(x, y; z) = \iint_{-\infty}^{\infty} \tilde{U}(f_x, f_y; z) \mathrm{e}^{\mathrm{i}2\pi(f_x x + f_y y)} \, \mathrm{d}f_x \, \mathrm{d}f_y \equiv \mathcal{F}^{-1}\left\{\tilde{U}(x, y; z)\right\} \tag{A.2.5}$$

If the field amplitude in the source plane $\tilde{u}(x, y; 0)$ is known the calculation of $\tilde{u}(x, y; z)$ with existence of Fast Fourier Transform algorithms becomes trivial using a PC :

$$\tilde{u}(x, y; z) = \mathcal{F}^{-1}\left\{\tilde{U}(f_x, f_y; z)\right\} \tag{A.2.6}$$

$$= \mathcal{F}^{-1}\left\{\tilde{U}(f_x, f_y; 0)\, H(f_x, f_y; z)\right\} \tag{A.2.7}$$

$$= \mathcal{F}^{-1}\left\{\mathcal{F}\{\tilde{u}(x, y; 0)\}\, H(f_x, f_y; z)\right\} \tag{A.2.8}$$

We note in passing that $h(x, y; z)$ from Eq. (A.1.2) and $H(f_x, f_y; z)$ from Eq. (A.2.4) are a Fourier pair.

B Optical-Bloch equations

B.1 Density matrix

An isolated quantum system in a state $|i\rangle$ is completely described by its normalized wave function $|\psi_i\rangle$. Choosing a complete orthonormal basis set $\{|n\rangle\}$ the wavefunction can be expanded as:

$$|\psi_i\rangle = \sum_n c_{ni}|n\rangle, \tag{B.1.1}$$

$$c_{ni} = \langle n|\psi_i\rangle. \tag{B.1.2}$$

In this case the system is said to be in the *pure* state $|\psi_i\rangle$. If the system interacts with the environment, the complete description will require the knowledge of the environmental wavefunction function as well. Unfortunately it is usually unknown and cannot be calculated. In this case the system cannot be described in terms of the isolated pure state wave function anymore. However, what could be known are the relative probabilities p_i to find the system in the corresponding pure states $|\psi_i\rangle$. A nonisolated system described by weighted pure (isolated) states is said to be in a state of an *incoherent mixture* and can be represented by a density operator [83]:

$$\hat{\rho} = \sum_i p_i|\psi_i\rangle\langle\psi_i| \tag{B.1.3}$$

with matrix elements:

$$\rho_{mn} = \langle m|\hat{\rho}|n\rangle = \sum_i p_i c_{mi} c_{ni}^* \tag{B.1.4}$$

If the system has just one isolated pure state $|\psi\rangle$, the density operator and its matrix elements become:

$$\hat{\rho} = |\psi\rangle\langle\psi|, \tag{B.1.5}$$

$$\rho_{mn} = c_m c_n^*. \tag{B.1.6}$$

The diagonal elements $\rho_{nn} = |c_n|^2$ are real and represent the populations of the corresponding states. In a closed system the net population is conserved and thus $\mathrm{Tr}(\hat{\rho}) = 1$. The off-diagonal matrix elements $\rho_{mn} = c_{mi}c_{ni}^*$ are in general complex and describe *coherences* between the states. They are nonzero only if the system is in coherent superposition of the states [70]. The density operator is Hermitian, therefore $\rho_{mn} = \rho_{nm}^*$.

Time evolution of the density matrix can be described by the Liouville-von-Neumann equation [83]:

$$\frac{\mathrm{d}}{\mathrm{d}t}\hat{\rho} = -\mathrm{i}\left[\hat{H}, \hat{\rho}\right], \tag{B.1.7}$$

Here atomic units are used ($\hbar = m_\mathrm{e} = e = k_\mathrm{e} = 1$). The total Hamiltonian of the system consists of the unperturbed and interaction parts:

$$\hat{H} = \hat{H}_0 + \hat{V}(t). \tag{B.1.8}$$

For a system with eigenstates $|n\rangle$ and energies ω_n the diagonal time-independent $\hat{H}_0$ reads as:

$$\hat{H}_0 = \sum_n \omega_n |n\rangle\langle n|. \tag{B.1.9}$$

The dipole operator of the system and its matrix elements are given by:

$$\hat{\mathbf{d}} = \sum_{m\neq n} \mathbf{d}_{mn}|n\rangle\langle m| + \mathrm{H.c.}, \tag{B.1.10}$$

$$\mathbf{d}_{mn} = \langle n|\hat{\mathbf{r}}|m\rangle, \tag{B.1.11}$$

where H.c. denotes the Hermitian conjugate and $\hat{\mathbf{r}}$ is the coordinate operator. In the

electric dipole approximation the interaction operator is:

$$\hat{V}(t) = -\hat{\mathbf{d}}\,\mathbf{E}(t). \tag{B.1.12}$$

For an n-level system Eq. (B.1.7) resolves into n^2 coupled differential equations, with only $n(n+1)/2$ of them being independent recalling that $\rho_{mn} = \rho^*_{nm}$.

The interaction with the environment (bath) can be modeled adding phenomenological damping terms:

$$\frac{\mathrm{d}}{\mathrm{d}t}\rho_{mn} = -\mathrm{i}\left[\hat{H},\hat{\rho}\right]_{mn} - \Gamma_{mn}\rho_{mn}, \tag{B.1.13}$$

where elements of matrix Γ are damping rates of the corresponding components of $\hat{\rho}$. For an exponential decay with characteristic times T_{mn} the rates are defined as $\Gamma_{mn} = T_{mn}^{-1}$.

B.2 Optical-Bloch equations for a three-level system

Let us derive the equations of motion for an idealized three-level electronic system which is the subject to ionization by a laser pulse. Thus, in total we have three eigenstates: $|0\rangle$ (ground), $|1\rangle$ (excited) and $|2\rangle$ (ionized) with energies ω_0, ω_1 and ω_2. Initially the system is in its ground state ($\rho_{00} = 1$ and all other components $\rho_{mn} = 0$). State $|1\rangle$ is an unstable unoccupied excited state with a finite lifetime. State $|2\rangle$ lays in the ionization continuum and its population ρ_{22} will correspond to the ionization yield observed in the experimental realization. For convenience we let the energy of the ground state be $\omega_0 = 0$. The energy differences between the levels are denoted as $\omega_{mn} = \omega_m - \omega_n$.

The dipole operator between the states $|m\rangle$ and $|n\rangle$ and interaction operator are given by:

$$\hat{\mathbf{d}}_{mn} = \mathbf{d}_{mn}\left(|n\rangle\langle m| + |m\rangle\langle n|\right), \tag{B.2.1}$$

$$\hat{V}_{mn} = -\hat{\mathbf{d}}_{mn}\mathbf{E}(t). \tag{B.2.2}$$

For simplicity the vector nature of the laser field and the dipole moments will be neglected (we assume them to be collinear). Then the laser pulse can be written as $E(t) = \mathcal{E}(t)\cos\omega_L t$ and the real dipole transition moments as d_{mn}. We express the electric field

as:

$$E(t) = \frac{1}{2}\left(\tilde{\mathcal{E}}(t)\mathrm{e}^{-\mathrm{i}\omega_L t} + \tilde{\mathcal{E}}^*(t)\mathrm{e}^{\mathrm{i}\omega_L t}\right). \tag{B.2.3}$$

Here we employ the so-called *rotating wave approximation* (RWA). The transformation to the interaction picture is done by a unitary operator $\hat{U} = \mathrm{e}^{\mathrm{i}\hat{H}_0 t} = \sum_n \mathrm{e}^{\mathrm{i}\omega_n t}|n\rangle\langle n|$. Recalling (B.2.3) it can be seen that applying this transformation to $\hat{V}(t)$ will give terms oscillating at frequencies $\omega_L + \omega_n$ and $\omega_L - \omega_n$. In our analysis we assume that the photon energy is near resonance to the atomic transition, i.e. $\omega_L \approx \omega_n$. The slowly varying terms with $\omega_L - \omega_n$ will dominate the observable response as the fast oscillating at $\omega_L + \omega_n$ terms will quickly average to zero at any reasonable timescale. Therefore we will neglect them. After writing the commutator in Eq. (B.1.13) explicitly the equations for the density matrix elements read as:

$$\frac{\mathrm{d}}{\mathrm{d}t}\rho_{mn} = -\mathrm{i}\omega_{mn}\rho_{mn} - \mathrm{i}\sum_k \left(V_{mk}\rho_{kn} - \rho_{mk}V_{kn}\right) - \Gamma_{mn}\rho_{mn}. \tag{B.2.4}$$

Introducing new variables:

$$\tilde{\rho}_{mn} = \rho_{mn}\mathrm{e}^{-\mathrm{i}\omega_L t}, \tag{B.2.5a}$$

$$\tilde{\rho}_{nm} = \rho_{nm}\mathrm{e}^{\mathrm{i}\omega_L t} = \tilde{\rho}^*_{mn}, \tag{B.2.5b}$$

$$\tilde{\rho}_{nn} = \rho_{nn}. \tag{B.2.5c}$$

and substituting them in Eq. (B.2.4) we can write the complete set of density matrix

equations for the three-level system:

$$\begin{aligned}
\frac{\mathrm{d}}{\mathrm{d}t}\rho_{00} &= \frac{\mathrm{i}}{2}d_{01}\left(\tilde{\mathcal{E}}^*\tilde{\rho}_{01}^* - \tilde{\mathcal{E}}\tilde{\rho}_{01}\right) + \Gamma_{11}\rho_{11},\\
\frac{\mathrm{d}}{\mathrm{d}t}\rho_{11} &= \frac{\mathrm{i}}{2}d_{01}\left(\tilde{\mathcal{E}}\tilde{\rho}_{01} - \tilde{\mathcal{E}}^*\tilde{\rho}_{01}^*\right) + \frac{\mathrm{i}}{2}d_{12}\left(\tilde{\mathcal{E}}\tilde{\rho}_{12} - \tilde{\mathcal{E}}^*\tilde{\rho}_{12}^*\right) - \Gamma_{11}\rho_{11},\\
\frac{\mathrm{d}}{\mathrm{d}t}\rho_{22} &= \frac{\mathrm{i}}{2}d_{02}\left(\tilde{\mathcal{E}}\tilde{\rho}_{02} - \tilde{\mathcal{E}}^*\tilde{\rho}_{02}^*\right) + \frac{\mathrm{i}}{2}d_{12}\left(\tilde{\mathcal{E}}\tilde{\rho}_{12} - \tilde{\mathcal{E}}^*\tilde{\rho}_{12}^*\right),\\
\frac{\mathrm{d}}{\mathrm{d}t}\tilde{\rho}_{01} &= -\mathrm{i}\Delta_{01}\tilde{\rho}_{01} + \frac{\mathrm{i}}{2}d_{01}\tilde{\mathcal{E}}^*\left(\rho_{11} - \rho_{00}\right) - \frac{\mathrm{i}}{2}d_{12}\tilde{\mathcal{E}}\tilde{\rho}_{02}^* - \Gamma_{01}\tilde{\rho}_{01},\\
\frac{\mathrm{d}}{\mathrm{d}t}\tilde{\rho}_{12} &= -\mathrm{i}\Delta_{12}\tilde{\rho}_{12} + \frac{\mathrm{i}}{2}d_{12}\tilde{\mathcal{E}}^*\left(\rho_{22} - \rho_{11}\right) + \frac{\mathrm{i}}{2}d_{01}\tilde{\mathcal{E}}\tilde{\rho}_{02}^* - \Gamma_{12}\tilde{\rho}_{12},\\
\frac{\mathrm{d}}{\mathrm{d}t}\tilde{\rho}_{02} &= -\mathrm{i}\Delta_{02}\tilde{\rho}_{02} + \frac{\mathrm{i}}{2}d_{02}\tilde{\mathcal{E}}^*\left(\rho_{22} - \rho_{00}\right) - \frac{\mathrm{i}}{2}\tilde{\mathcal{E}}^*\left(d_{01}\tilde{\rho}_{12}^* - d_{12}\tilde{\rho}_{01}^*\right) - \Gamma_{02}\tilde{\rho}_{02}.
\end{aligned} \tag{B.2.6}$$

where detuning of the laser frequency from the resonance is $\Delta_{mn} = \omega_{mn} - \omega_L$ and a notation $\tilde{\mathcal{E}}(t) \equiv \tilde{\mathcal{E}}$ was used for clarity. Since state $|0\rangle$ is the ground state and $|2\rangle$ is the observable in the experiment, $\Gamma_{00} = \Gamma_{22} = 0$. Also, the transient population $\rho_{11}(t)$ is assumed to decay only to the ground state $|0\rangle$.

Bibliography

[1] M. Shapiro and P. Brumer. "Coherent control of molecular dynamics". *Reports on Progress in Physics* 66.6 (2003), pp. 985–990. DOI: 10.1088/0034-4885/66/6/201.

[2] M. Dantus and V. V. Lozovoy. "Experimental coherent laser control of physicochemical processes". *Chemical Reviews* 104 (2004), pp. 1813–1860. DOI: 10.1021/cr020668r.

[3] K. Ohmori. "Wave-packet and coherent control dynamics". *Annual Review of Physical Chemistry* 60 (2009), pp. 487–511. DOI: 10.1146/annurev.physchem.59.032607.093818.

[4] A. M. Weiner. "Femtosecond optical pulse shaping and processing". *Progress in Quantum Electronics* 19 (1995), pp. 161–237. DOI: 10.1016/0079-6727(94)00013-0.

[5] R. Trebino. "Frequency-Resolved Optical Gating: The Measurement of Ultrashort Laser Pulses". Springer Science+Business Media New York, 2000.

[6] J.-C. Diels and W. Rudolph. "Ultrashort Laser Pulse Phenomena". 2nd ed. Elsevier, 2006.

[7] T. Gebert et al. "Michelson-type all-reflective interferometric autocorrelation in the VUV regime". *New Journal of Physics* 16 (2014), p. 073047. DOI: 10.1088/1367-2630/16/7/073047.

[8] N. S. Sariciftci et al. "Photoinduced electron transfer from a conducting polymer to buckminsterfullerene". *Science* 258 (1992), pp. 1474–1476. DOI: 10.1126/science.258.5087.1474.

[9] G. Yu et al. "Polymer photovoltaic cells: Enhanced efficiencies via a network of internal donor-acceptor heterojunctions". *Science* 270 (1995), pp. 1789–1791. DOI: 10.1126/science.270.5243.1789.

[10] G. D. Scholes and G. Rumbles. "Excitons in nanoscale systems". *Nature Materials* 5 (2006), pp. 683–696. DOI: 10.1038/nmat1710.

[11] S. Klaiman et al. "Extreme correlation effects in the elusive bound spectrum of C_{60}^-". *Journal of Physical Chemistry Letters* 4 (2013), pp. 3319–3324. DOI: 10.1021/jz4018514.

[12] S. Klaiman et al. "All for one and one for all: accommodating an extra electron in C_{60}". *Physical Chemistry Chemical Physics* 16 (2014), pp. 13287–13293. DOI: 10.1039/C4CP01447B.

[13] V. K. Voora and K. D. Jordan. "Nonvalence correlation-bound anion states of spherical fullerenes". *Nano Letters* 14 (2014), pp. 4602–4606. DOI: 10.1021/nl5016574.

[14] H. W. Kroto et al. "C_{60}: Buckminsterfullerene". *Nature* 318 (1985), pp. 162–163. DOI: 10.1038/318162a0.

[15] W. Krätschmer et al. "Solid C_{60}: a new form of carbon". *Nature* 347 (1990), pp. 354–358. DOI: 10.1038/347354a0.

[16] Y. Pavlyukh and J. Berakdar. "Angular electronic band structure of molecules". *Chemical Physics Letters* 468 (2009), pp. 313–318. DOI: 10.1016/j.cplett.2008.12.051.

[17] I. V. Hertel et al. "Ultrafast excitation and ionization and and fragmentation of C_{60}". *Advances in Atomic and Molecular and and Optical Physics* 50 (2005), pp. 219–286. DOI: 10.1016/S1049-250X(05)80010-2.

[18] F. Lepine. "Multiscale dynamics of C_{60} from attosecond to statistical physics". *Journal of Physics B: Atomic and Molecular and Optical Physics* 48 (2015), p. 122002. DOI: 10.1088/0953-4075/48/12/122002.

[19] P. H. Bucksbaum et al. "Role of the ponderomotive potential in above-threshold ionization". *Journal of the Optical Society of America B* 4.5 (1987), pp. 760–764. DOI: 10.1364/JOSAB.4.000760.

[20] F. H. M. Faisal. "Theory of Multiphoton Processes". Springer Science, 1987.

[21] P. Lambropoulos. "Mechanisms for multiple ionization of atoms by strong pulsed lasers". *Physcal Review Letters* 55 (1985), pp. 2141–2144. DOI: 10.1103/PhysRevLett.55.2141.

[22] N. B. Delone and V. P. Krainov. "Multiphoton Processes in Atoms". Springer-Verlag, 1994.

[23] P. Lambropoulos. "Topics on Multiphoton Processes in Atoms". *Advances in Atomic and Molecular Physics* 12 (1976), pp. 87–164. DOI: 10.1016/S0065-2199(08)60043-3.

[24] L. V. Keldysh. "Ionization in the field of a strong electromagnetic wave". *Soviet Physics JETP* 45 (1965), pp. 1307–1314.

[25] M. Lezius et al. "Nonadiabatic multielectron dynamics in strong field molecular ionization". *Physcal Review Letters* 86 (2001), pp. 51–54. DOI: 10.1103/PhysRevLett.86.51.

[26] M. Lezius et al. "Polyatomic molecules in strong laser fields: nonadiabatic multielectron dynamics". *Journal of Chemical Physics* 117 (2002), pp. 1572–1588. DOI: http://dx.doi.org/10.1063/1.1487823.

[27] Y. Huismans et al. "Macro-atom versus many-electron effects in ultrafast ionization of C_{60}". *Physical Review A* 88 (2013), p. 013201. DOI: 10.1103/PhysRevA.88.013201.

[28] M. Wickenhauser et al. "Signatures of tunneling and multiphoton ionization in the electron-momentum distributions of atoms by intense few-cycle laser pulses". *Physcal Review A* 74 (2006), p. 041402. DOI: 10.1103/PhysRevA.74.041402.

[29] M. Kjellberg et al. "Momentum-map-imaging photoelectron spectroscopy of fullerenes with femtosecond laser pulses". *Physical Review A* 81 (2010), p. 023202. DOI: 10.1103/PhysRevA.81.023202.

[30] I. Shchatsinin et al. "Ultrafast energy redistribution in C_{60} fullerenes: A real time study by two-color femtosecond spectroscopy". *Journal of Chemical Physics* 129 (2008), p. 204308. DOI: 10.1063/1.3026734.

[31] M. S. Dresselhaus et al. "Science of Fullerenes and Carbon Nanotubes". Academic Press, 1996.

[32] G. P. Zhang and T. F. George. "Controlling vibrational excitations in C_{60} by laser pulse durations". *Physcal Review Letters* 93 (2004), p. 147401. DOI: 10.1103/PhysRevLett.93.147401.

[33] T. Laarmann et al. "Control of giant breathing motion in C_{60} with temporally shaped laser pulses". *Physcal Review Letters* 98 (2007), p. 058302. DOI: 10.1103/PhysRevLett.98.058302.

[34] R. C. Haddon et al. "Electronic structure and bonding in icosahedral C_{60}". *Chemical Physics Letters* 125.5–6 (1986), pp. 459–464. DOI: 10.1016/0009-2614(86)87079-8.

[35] G. Cappellini et al. "Quasiparticle energies in clusters determined via total-energy differences: application to C_{60} and Na_4". *Physcal Review B* 56.7 (1997), pp. 2633–2636. DOI: 10.1103/PhysRevB.56.3628.

[36] E. E. B. Campbell et al. "Sequential ionization of C_{60} with femtosecond laser pulses". *Journal of Chemical Physics* 114 (2001), pp. 1716–1719. DOI: 10.1063/1.1336573.

[37] K. Hansen et al. "Thermal electron emission from the hot electronic subsystem of vibrationally cold C_{60}". *Journal of Chemical Physics* 119 (2003), pp. 2513–2522. DOI: 10.1063/1.1584671.

[38] E. E. B. Campbell and R. D. Levine. "Delayed ionization and fragmentation en route to thermionic emission: statistics and dynamics". *Annual Review of Physical Chemistry* 51 (2000), pp. 65–98. DOI: 10.1146/annurev.physchem.51.1.65.

[39] E. E. B. Campbell et al. "Delayed ionization of C_{60} and C_{70}". *Physical Review Letters* 67.15 (1991), pp. 1986–1988. DOI: 10.1103/PhysRevLett.67.1986.

[40] E. E. B. Campbell et al. "Thermionic emission from the fullerenes". *Zeitschrift fuerr Physik D: Atoms and Molecules and Clusters* 24 (1992), pp. 81–85. DOI: 10.1007/BF01436607.

[41] H. Kataura et al. "Optical absorption of gas phase C_{60} and C_{70}". *Japanese Journal of Applied Physics* 32 (1993), pp. 1789–1791. DOI: 10.1143/JJAP.32.L1667.

[42] M. Boyle et al. "Excitation of Rydberg series in C_{60}". *Physical Review Letters* 87.27 (2001), p. 273401. DOI: 10.1103/PhysRevLett.87.273401.

[43] M. Boyle et al. "Two-color pump-probe study and internal-energy dependence of Rydberg-state excitation in C_{60}". *Physical Review A* 70 (2004), p. 051201. DOI: 10.1103/PhysRevA.70.051201.

[44] M. Boyle et al. "Excitation dynamics of Rydberg states in C_{60}". *European Physical Journal D* 36 (2005), pp. 339–351. DOI: 10.1140/epjd/e2005-00281-7.

[45] A. N. Markevitch et al. "Sequential nonadiabatic excitation of large molecules and ions driven by strong laser fields". *Physcal Review A* 69 (2004), p. 013401. DOI: 10.1103/PhysRevA.69.013401.

[46] G. P. Zhang et al. "Laser-induced ultrafast dynamics in C_{60}". *Physcal Review B* 68 (2003), p. 165410. DOI: 10.1103/PhysRevB.68.165410.

[47] D. Bauer et al. "C_{60} in intense femtosecond laser pulses: nonlinear dipole response and ionization". *Physical Review A* 64 (2001), p. 063203. DOI: 10.1103/PhysRevA.64.063203.

[48] V. R. Bhardwaj et al. "Internal laser-induced dipole force at work in C_{60} molecule". *Physical Review Letters* 91.4 (2003), p. 203004. DOI: 10.1103/PhysRevLett.91.203004.

[49] A. Jaron-Becker et al. "Saturated ionization of fullerenes in intense laser fields". *Physcal Review Letters* 93 (2006), p. 143006. DOI: 10.1103/PhysRevLett.96.143006.

[50] I. Shchatsinin et al. "C_{60} in intense short pulse laser fields down to 9fs: excitation on time scales below e-e and e-phonon coupling". *Journal of Chemical Physics* 125 (2006), p. 194320. DOI: 10.1063/1.2362817.

[51] M. Feng et al. "Atomlike and hollow-core–bound molecular orbitals of C_{60}". *Science* 320 (2008), pp. 359–362. DOI: 10.1126/science.1155866.

[52] J. O. Johansson et al. "Angular-resolved photoelectron spectroscopy of superatom orbitals of fullerenes". *Physical Review Letters* 108 (2012), p. 173401. DOI: 10.1103/PhysRevLett.108.173401.

[53] B. Mignolet et al. "Probing rapidly-ionizing superatom molecular orbitals in C_{60}: a computational and femtosecond photoelectron spectroscopy study". *Journal of Chemical Physics* 14 (2013), pp. 3332–3340. DOI: 10.1002/cphc.201300585.

[54] E. Bohl et al. "Relative photoionization cross-sections of super-atom molecular orbitals (SAMOs) in C_{60}". *Journal of Physical Chemistry* 119 (2015), pp. 11504–11508. DOI: 10.1021/acs.jpca.5b10339.

[55] J. Zhao and H. Petek. "Non-nuclear electron transport channels in hollow molecules". *Physical Review B* 90 (2014), p. 075412. DOI: 10.1103/PhysRevB.90.075412.

[56] J. Wätzel et al. "Optical vortex driven charge current loop and optomagnetism in fullerenes". *Carbon* 99 (2016), pp. 439–443. DOI: 10.1016/j.carbon.2015.12.028.

[57] J. Zhao et al. "The superatom states of fullerenes and their hybridization into the nearly free electron bands of fullerites". *ASC Nano* 3.4 (2009), pp. 853–864. DOI: 10.1021/nn800834k.

[58] L. Zoppi et al. "Buckybowl superatom states: a unique route for electron transport?" *Physical Chemistry Chemical Physics* 17 (2015), pp. 6114–6121. DOI: 10.1039/c4cp05776g.

[59] D. B. Dougherty et al. "Band formation in a molecular quantum well via 2D superatom orbital interactions". *Physcal Review Letters* 109 (2012), p. 266802. DOI: 10.1103/PhysRevLett.109.266802.

[60] I. V. Hertel et al. "Giant plasmon excitation in free C_{60} and C_{70} molecules studied by photoionization". *Physical Review Letters* 68.6 (1992), pp. 784–787. DOI: 10.1103/PhysRevLett.68.784.

[61] M. Y. Amusia and J.-P. Connerade. "The theory of collective motion probed by light". *Reports on Progress in Physics* 63 (2000), pp. 41–70. DOI: 10.1088/0034-4885/63/1/202.

[62] G. F. Bertsch et al. "Collective plasmon excitations in C_{60} clusters". *Physical Review Letters* 67.19 (1991), pp. 2690–2693. DOI: 10.1103/PhysRevLett.67.2690.

[63] S. W. J. Scully et al. "Photoexcitation of a volume plasmon in C_{60} ions". *Physical Review Letters* 94 (2005), p. 065503. DOI: 10.1103/PhysRevLett.94.065503.

[64] M. Schüler et al. "Disentangling multipole contributions to collective excitations in fullerenes". *Physical Review A* 92 (2016), p. 02104. DOI: 10.1103/PhysRevA.92.021403.

[65] E. Maurat et al. "Surface plasmon resonance in C_{60} revealed by photoelectron imaging spectroscopy". *Journal of Physics B: Atomic and Molecular and Optical Physics* 42 (2009), p. 165105. DOI: 10.1088/0953-4075/42/16/165105.

[66] T. Barillot et al. "Angular asymmetry and attosecond time delay from the giant plasmon resonance in C_{60} photoionization". *Physical Review A* 91 (2015), p. 033413. DOI: 10.1103/PhysRevA.91.033413.

[67] E. P. Wigner. "Lower limit for the energy derivative of the scattering phase shift". *Physcal Review* 98 (1955), pp. 145–147. DOI: 10.1103/PhysRev.98.145.

[68] R. A. Ganeev et al. "Higher-order harmonic generation from fullerene by means of the plasma harmonic method". *Physcal Review Letters* 102 (2009), p. 013903. DOI: 10.1103/PhysRevLett.102.013903.

[69] L. Mandel and E. Wolf. "Optical Coherence and Quantum Optics". Cambridge University Press, 1995.

[70] R. W. Boyd. "Nonlinear Optics". 3rd ed. Academic Press, 2008.

[71] K. Naganuma et al. "General method for ultrashort light pulse chirp measurement". *IEEE Journal of Quantum Electronics* 25.6 (1989), pp. 1225–1233. DOI: 10.1109/3.29252.

[72] J. H. Chung and A. M. Weiner. "Ambiguity of ultrashort pulse shapes retrieved from the intensity autocorrelation and the power spectrum". *IEEE Journal of Selected Topics in Quantum Electronics* 7 (2001), pp. 656–666. DOI: 10.1109/2944.974237.

[73] D. J. Kane and R. Trebino. "Characterization of arbitrary femtosecond pulses using frequency-resolved optical gating". *IEEE Journal of Quantum Electronics* 29 (1993), pp. 571–579. DOI: 10.1109/3.199311.

[74] C. Iaconis and I. A. Walmsley. "Spectral phase interferometry for direct electric-field reconstruction of ultrashort optical pulses". *Optics Letters* 23 (1998), pp. 792–794. DOI: 10.1364/OL.23.000792.

[75] G. Stibenz and G. Steinmeyer. "Interferometric frequency-resolved optical gating". *Optics Express* 13 (2005), pp. 2617–2626. DOI: 10.1364/OPEX.13.002617.

[76] T. Sekikawa et al. "Frequency-resolved optical gating of femtosecond pulses in the extreme ultraviolet". *Physcal Review Letters* 91 (2003), p. 103902. DOI: 10.1103/PhysRevLett.91.103902.

[77] T. Sekikawa et al. "Measurement of the intensity-dependent atomic dipole phase of a high harmonic by frequency-resolved optical gating". *Physcal Review Letters* 88 (2002), p. 193902. DOI: 10.1103/PhysRevLett.88.193902.

[78] G. De Ninno et al. "Single-shot spectro-temporal characterization of XUV pulses from a seeded free-electron laser". *Nature Communications* (2015). DOI: 10.1038/ncomms9075.

[79] H. J. Eichler and A. Hermerschmidt. "Photorefractive Materials and Their Applications 1". Ed. by P. Guenter and J. P. Huignard. 1st ed. Springer Series in Optical Sciences, 2006. Chap. Light-Induced Dynamic Gratings and Photorefraction.

[80] H. Mashiko et al. "All-reflective interferometric autocorrelator for the measurement of ultra-short optical pulses". *Applied Physics B* 76 (2003), pp. 525–530. DOI: 10.1007/s00340-003-1148-0.

[81] E. J. Moler et al. "Design and performance of a soft X-ray inrerferometer for ultra-high resolution Fourier transform spectroscopy". *Journal of Electron Spectroscopy and Related Phenomena* 80 (1996), pp. 309–312. DOI: 10.1016/0368-2048(96)02982-9.

[82] C. Palmer and E. Loewen. "Diffraction Grating Handbook". Newport Corporation, 2005.

[83] R. Loudon. "The Quantum Theory of Light". 3rd ed. Oxford University Press, 2000.

[84] C. Cohen-Tannoudji et al. "Atom-Photon Interactions. Basic Processes and Applications". Wiley-VCH, 2004.

[85] W. Nessler et al. "Energy relaxation and dephasing times of excited electrons in $Bi_2Sr_2CaCu_2O_{8+\delta}$ from interferometric 2-photon time-resolved photoemission". *Journal of Electron Spectroscopy and Related Phenomena* 88–91 (1998), pp. 495–501. DOI: 10.1016/S0368-2048(97)00260-0.

[86] I. Estermann. "Molecular beam technique". *Review of Modern Physics* 54.7 (1946), pp. 4484–4487. DOI: 10.1103/RevModPhys.18.300.

[87] V. Piacente et al. "Vapor pressure of C_{60} buckminsterfullerene". *Journal of Physical Chemistry* 99 (1995), pp. 14052–14057. DOI: 10.1021/j100038a041.

[88] N. F. Ramsey. "Molecular Beams". Oxford University Press, 1956.

[89] A. Popovic et al. "Mass spectrometric investigations of fullerenes. I. Vapour pressure over the C_{60}/C_{70} binary system". *Rapid Communications in Mass Spectrometry* 8 (1994), pp. 985–990. DOI: 10.1002/rcm.1290081216.

[90] R. Pankajavalli et al. "Vapour pressure of C_{60} by a transpiration method using a horizontal thermobalance". *Thermochimica Acta* 316 (1998), pp. 101–108. DOI: 10.1016/S0040-6031(98)00304-9.

[91] J. O. Johansson et al. "Visible and ultraviolet photoelectron spectroscopy of fullerenes using femtosecond laser pulses". *EPJ Web of Conferences* 41 (2013), p. 02015. DOI: 10.1051/epjconf/20134102015.

[92] B. Schmidt et al. *LAB2-A virtual femtosecond laser lab*. URL: http://www.lab2.de.

[93] J. E. Harvey et al. "Transfer function characterization of grazing incidence optical systems". *Applied Optics* 27.8 (1988), pp. 1527–1533. DOI: 10.1364/AO.27.001527.

[94] A. Barty et al. "Predicting the coherent X-ray wavefront focal properties at the Linac Coherent Light Source (LCLS) X-ray free electron laser". *Optics Express* 17.8 (2009), pp. 15508–15519. DOI: 10.1364/OE.17.015508.

[95] L. Chen et al. "Dynamic out-of-plane profilometry for nano-scale fullfield characterization of MEMS using stroboscopic interferometry with novel signal deconvolution algorithm". *Optics and Lasers in Engineering* 47 (2009), pp. 237–251. DOI: 10.1016/j.optlaseng.2008.05.016.

[96] G. S. Kino and S. S. C. Chim. "Mirau correlation microscope". *Applied Optics* 29.26 (1990), pp. 3775–3783. DOI: 10.1364/AO.29.003775.

[97] *Edixeon Federal LEDs datasheet*. Edison.

[98] B. Whitaker. "Imaging in Molecular Dynamics: Technology and Applications". Cambridge University Press, 2003.

[99] C. Bordas et al. "Photoelectron imaging spectrometry: Principle and inversion method". *Review of Scientific Instruments* 67 (1996), pp. 2257–2268. DOI: 10.1063/1.1147044.

[100] L. M. Smith et al. "Abel inversion using transform techniques". *Journal of Quantitative Spectroscopy and Radiative Transfer* 39.5 (1988), pp. 367–373. DOI: 10.1016/0022-4073(88)90101-X.

[101] M. J. J. Vrakking. "An iterative procedure for the inversion of two-dimensional ion/photoelectron imaging experiments". *Review of Scientific Instruments* 72.11 (2001), pp. 4084–4089. DOI: 10.1063/1.1406923.

[102] V. Dribinski et al. "Reconstruction of Abel-transformable images: The Gaussian basis-set expansion Abel transform method". *Review of Scientific Instruments* 73.7 (2002), pp. 2634–2642. DOI: 10.1063/1.1482156.

[103] G. A. Garcia et al. "Two-dimensional charged particle image inversion using a polar basis function expansion". *Review of Scientific Instruments* 75.11 (2004), pp. 4989–4996. DOI: 10.1063/1.1807578.

[104] D. W. Chandler and P. L. Houston. "Two-dimensional imaging of state-selected photodissociation products detected by multiphoton ionization". *Journal of Chemical Physics* 87 (1987), pp. 1445–1447. DOI: 10.1063/1.453276.

[105] A. T. J. B. Eppink and D. H. Parker. "Velocity map imaging of ions and electrons using electrostatic lenses: application in photoelectron and photofragment ion imaging of molecular oxygen". *Review of Scientific Instruments* 68 (1997), pp. 3477–3484. DOI: 10.1063/1.1148310.

[106] M. Schultze et al. "Spatially resolved measurement of ionization yields in the focus of an intense laser pulse". *New Journal of Physics* 13 (2011), p. 033001. DOI: 10.1088/1367-2630/13/3/033001.

[107] A. Vredenborg et al. "A photoelectron-photoion coincidence imaging apparatus for femtosecond time-resolved molecular dynamics with electron time-of-flight resolution of σ = 18 ps and energy resolution ΔE/E = 3.5%". *Review of Scientific Instruments* 79 (2008), p. 063108. DOI: 10.1063/1.2949142.

[108] *SIMION Industry standard charged particle optics simulation software*. Scientific Instrument Services and Inc. (SIS). URL: http://simion.com/.

[109] G. A. Garcia et al. "A refocusing modified velocity map imaging electron/ion spectrometer adapted to synchrotron radiation studies". *Review of Scientific Instruments* 76 (2005), p. 053302. DOI: 10.1063/1.1900646.

[110] J. L. Wiza. "Microchannel plate detectors". *Nuclear Instruments and Methods* 162 (1979), pp. 587–601. DOI: 10.1016/0029-554X(79)90734-1.

[111] A. L. Smith. "Comparison of the ultraviolet absorption cross section of C_{60} buckminsterfullerene in the gas phase and in hexane solution". *Journal of Physics B: Atomic and Molecular Physics* 29 (1996), pp. 4975–4980. DOI: 10.1088/0953-4075/29/21/011.

[112] S. Usenko et al. "Femtosecond dynamics of correlated many-body states in isolated C_{60} fullerenes". *New Journal of Physics* 18 (2016), p. 113055. DOI: 10.1088/1367-2630/18/11/113055.

[113] D. P. Chong. "Recent Advances in Density Functional Systems. Part I." World Scientific, 1995.

[114] M. A. L. Marques et al. "OCTOPUS: a first-principles tool for excited electron–ion dynamics". *Computer Physics Communications* 151.1 (2003), pp. 60–78. DOI: 10.1016/S0010-4655(02)00686-0.

[115] A. Kickermann. "Rotational Coherence Spectroscopy at FLASH: Toward Dynamic Studies in Nanosuperfuids". PhD thesis. University of Hamburg, 2013.

[116] G. J. Dutton et al. "Exciton dynamics at molecule-metal interfaces: C_{60}/Au(111)". *Physcal Review B* 72 (2005), p. 045441. DOI: 10.1103/PhysRevB.72.045441.

[117] E. Knoesel et al. "Ultrafast dynamics of hot electrons and holes in copper: excitation and energy relaxation and and transport effects". *Physical Review B* 57.20 (1998), pp. 12812–12824. DOI: 10.1103/PhysRevB.57.12812.

[118] H. Köppel et al. "The Jahn-Teller Effect: Fundamentals and Implications for Physics and Chemistry". Springer, 2009.

[119] H.-P. Breuer and F. Petruccione. "The Theory of Open Quantum Systems". Oxford University Press, 2003.

[120] E. E. B. Campbell et al. "From above threshold ionization to statistical electron emission: the laser pulse-duration dependence of C_{60} photoelectron spectra". *Physical Review Letters* 102 (2000), pp. 2128–2131. DOI: 10.1103/PhysRevLett.84.2128.

[121] M. Martins et al. "Monochromator beamline for FLASH". *Review of Scientific Instruments* 77 (2006), p. 115108. DOI: 10.1063/1.2364148.

[122] N. Gerasimova et al. "The monochromator beamline at FLASH: performance, capabilities and upgrade plans". *Journal of Modern Optics* 58.16 (2011), pp. 1480–1485. DOI: 10.1080/09500340.2011.588344.

[123] Data by G. Brenner.

[124] F. Sorgenfrei et al. "The extreme ultraviolet split and femtosecond delay unit at the plane grating monochromator beamline PG2 at FLASH". *Review of Scientific Instruments* 81 (2010), p. 043107. DOI: 10.1063/1.3374166.

[125] R. Mitzner et al. "Spatio–temporal coherence of free electron laser pulses in the soft x-ray regime". *Optics Express* 16.24 (2008), pp. 19909–19919. DOI: 10.1364/OE.16.019909.

[126] W. F. Schlotter et al. "Longitudinal coherence measurements of an extreme-ultraviolet free-electron laser". *Optics Letters* 35.3 (2010), pp. 372–374. DOI: 10.1364/OL.35.000372.

[127] A. Singer et al. "Spatial and temporal coherence properties of single free-electron laser pulses". *Optics Express* 20.16 (2012), p. 17480. DOI: 10.1364/OE.20.017480.

[128] S. Usenko et al. *Submitted*.

[129] F. Calegari et al. "Ultrafast electron dynamics in phenylalanine initiated by attosecond pulses". *Science* 346 (2014), pp. 336–339. DOI: 10.1126/science.1254061.

[130] F. Bencivenga et al. "Four-wave mixing experiments with extreme ultraviolet transient gratings". *Nature* 520 (2015), pp. 205–208. DOI: 10.1038/nature14341.

[131] M. I. Stockman. "Nanoplasmonics: past, present, and glimpse into future". *Optics Express* 19 (2011), pp. 483–486. DOI: 10.1364/OE.19.022029.

[132] M. L. Brongersma and V. M. Shalaev. "The case for plasmonics". *Science* 328 (2010), pp. 440–441. DOI: 10.1126/science.1186905.

[133] J. W. Goodman. "Introduction to Fourier Optics". 2nd ed. The McGraw-Hill Companies, 1996.

[134] M. Born and E. Wolf. "Principles of Optics". 7th ed. Cambridge University Press, 2003.

[135] J. E. Harvey. "Fourier treatment of near-field scalar diffraction theory". *American Journal of Physics* 47 (1979), pp. 974–980. DOI: 10.1119/1.11600.

Acknowledgments

There is a large number of people without whom this work would not be possible. Hence, I would like to thank:

- my advisor PD. DR. TIM LAARMANN for giving me the opportunity to make the PhD in his group, for his supervision, support and being open for all my questions.
- PROF. DR. MARKUS DRESCHER for being my second supervisor and making his lab available for experiments which became an important part of this thesis.

Next, I would like to thank my present and former colleagues from the *X-ray Femtochemistry* group for their work support. In particular:

- DR. ANDREAS PRZYSTAWIK for his tremendous help in all the experiments which I performed during my work on this thesis and for teaching me a lot of things related to experimental physics. I also grateful for his translation of my abstract to German and useful comments related to the thesis.
- MARKUS JAKOB for his invaluable help in the experimental work (especially the C_{60} experiment).
- LESLIE LAZZARINO for his help in the development of the WLI setup.
- FLORIAN JACOBS for performing the vibration measurements.
- former colleagues: DR. ANDREAS KICKERMANN who built the spectrometer which was used in early experiments constituting my thesis; DR. JÖRN BÖDEWADT and DR. LASSE SCHRÖDTER for their useful advice in early stages of my PhD studies.

I am grateful to the members of the FLASH Team DR. GÜNTER BRENNER and DR. SVEN TOLEIKIS for their support in the FEL experiment. I thank the rest of the

FS-FL group for lunch breaks and parties we had together, my stay here would not be so enjoyable without it.

I also would like to thank my office mate DR. EVGENY SALDIN for our not very frequent, but very informative physics discussions.

I am grateful to DR. ARMIN AZIMA from the *DynamiX* group for developing the UV fs laser system used in the C_{60} experiments.

This work would be impossible without DESY and Hamburg University workshops which manufactured a large amount of experimental equipment utilized in my work. In particular, I would like to thank the Hasylab workshop for always being fast and responsive in preparing my urgent orders.

Special thanks goes to KAROLIN MERTENS who went to the trouble of proofreading the complete text of the thesis, for all the suggestions she made and all the mistakes she found ☺.

And last but not the least, I thank my family who always supported me throughout all my work and was sympathetic to my lack of time during the last weeks of writing the thesis.